Faculty of Mathematics and Physics of Charles University
in Prague

Measurement of Dijet Production at Low Q^2 at HERA

Doctoral Thesis
2004

Kamil Sedlák

Prohlašuji, že jsem dizertační práci vypracoval samostatně s použitím uvedené literatury. Souhlasím se zapůjčením diplomové práce.

V Rozích, 14.3.2004

Measurement of Dijet Production at Low Q^2 at HERA

Kamil Sedlák

Institute of Physics,
Academy of Sciences of the Czech Republic,
Prague

Supervisor: Dr. Jaroslav Cvach

Abstract

The measurement of triple differential dijet cross sections in $e^{\pm}p$ interactions in the H1 experiment in the region of photon virtualities $2 < Q^2 < 80\,\mathrm{GeV}^2$, inelasticities $0.1 < y < 0.85$, jet transverse energies $E^*_{T\,1} > 7\,\mathrm{GeV}$, $E^*_{T\,2} > 5\,\mathrm{GeV}$, and pseudorapidities $-2.5 < \eta^*_1, \eta^*_2 < 0$ is presented. The analysis was done in the $\gamma^* p$ centre-of-mass frame using an integrated luminosity of $57.6\,\mathrm{pb}^{-1}$. The data are compared with Monte Carlo event generators based on LO QCD cross sections and NLO QCD parton level calculations. The latter fail to describe the region of low Q^2 and low jet transverse energies, in contrast to the LO Monte Carlo generators that include direct and resolved photon interactions. The effects of resolved photons with longitudinal polarisation and initial and final state parton showers are investigated in detail.

The data show clear evidence for effects that go beyond the fixed-order NLO QCD calculations.

Acknowledgements

First of all, I would like to thank to the supervisor of my Thesis, Jaroslav Cvach, for his guidance, continuous support and encouragement and for great working conditions. During the time of our collaboration, he became more than a teacher and colleague for me.

I am also grateful to Jiří Chýla, Marek Taševský, Alice Valkárová and Hannes Jung for many valuable discussions, suggestions and for they constant support, which largely exceeded their duty and even the usual level of collaboration. I especially appreciate the help from Jiří Chýla, who spent a lot of time with me even though he was occupied with other duties.

I would also like to thank to Tomáš Laštovička, Paul Newman, Christian Schwanenberger, Steve Maxfield, Günter Grindhammer, Roman Pöschl, Oliver Nix, Torbjörn Sjöstrand, Jaroslav Zálešák and many others for their help with solving particular problems in my analysis.

This work has been supported in part by the Ministry of Education of the Czech Republic under the projects INGO-LA116/2000 and LN00A006 and by GA AV ČR grant no. IAB1010005.

Contents

Introduction

The analyses of jet production in various high energy processes have become a major field for testing perturbative QCD. In the case of electron-proton collisions, investigated in this Thesis, the jet cross sections are successfully described in most of the HERA kinematic range by next-to-leading (NLO) QCD calculations [H101a, H101c, H102a, H103a, ZEUS02b, ZEUS02c, ZEUS03b, ZEUS03a, H103b, H102b, ZEUS02a, H101b]. However, regions of phase space have previously been identified where NLO predictions do not reproduce the data satisfactorily [H103b, H102b, ZEUS02a, H101b, ZEUS00, ZEUS99].

The present analysis describes a new measurement of the dijet cross sections together with detailed comparisons of the data with available perturbative QCD calculations in order to identify which of them describe the data in which region. In doing that we use NLO QCD calculations (i.e. including terms up to order $\alpha\alpha_s^2$) as well as LO calculations supplemented with parton showers, which take into account leading logarithmic contributions to all orders.

At HERA, a photon coupling[1] to the incoming electron interacts with a parton from the proton. The measurement of dijet production is particularly suitable for the investigation of effects related to photon structure, which has been studied during the last two decades in e^+e^- and ep collisions (for comprehensive surveys of present data on photon structure and related issues see [KZS01, Nis00]). In the *"photoproduction"* regime, i.e. for $Q^2 \ll \Lambda^2_{\mathrm{QCD}}$, the interaction can be described by the sum of two contributions. In the *direct photon* process, the photon interacts as a whole with a parton from the proton, whereas in the *resolved photon* process, it behaves as a source of partons, which subsequently interact with partons from the proton.

The nature of the resolved component is still not well understood, especially the way in which it dies out with increasing photon virtuality. It has been argued [SS96, GRS96, GRS99, KP98, CT00a] that the concept of the resolved photon is very useful phenomenologically for arbitrary Q^2, provided the photon virtuality remains much smaller than some measure of the hardness of the process in which the photon participates. In our case this is satisfied for $Q^2 \ll E_T^2$, where E_T denotes the jet transverse energy. Only in the limit of large Q^2, in our case $Q^2 > E_T^2$, the fixed-order calculations dispensing with the photon

[1] In the low virtuality region investigated in this Thesis ($Q^2 < 80\,\mathrm{GeV}^2$), the contribution of Z, W^+ and W^- bosons can be neglected. Only photons are therefore considered as the intermediate particles.

structure can be used quite successfully.

A special attention is devoted to the contribution of longitudinally polarised photons. We know that due to gauge invariance the longitudinal photon interactions must vanish in the limit $Q^2 \to 0$. However, it has been argued in theoretical studies [CT00b, FS00] that their contribution becomes significant at nonvanishing Q^2. Also in the few instances where the effects of longitudinal photon have been measured in the intermediate Q^2 region, their contribution was found to be quite significant [HER00a, H197a, HER00b]. Some of these contributions can be given a partonic interpretation, and the parton distribution functions (PDFs) can be introduced in the very same way as is often done for transversely polarised resolved photons [SS96, CT01, Chy00a, Chy00b].

Recently a first set of PDFs for the longitudinally polarised photon has been presented by Chýla [Chy00b]. For larger Q^2, in our analysis $Q^2 > 2\,\mathrm{GeV}^2$, the sensitivity of photon PDF to the non-perturbative input is substantially reduced and the theoretical predictions rely mainly on the perturbative QCD calculations.

The present analysis extends some aspects of the previous H1 measurements dealing with the structure of virtual photons, namely the Thesis [Tas99] and the publication [H100]. Using 50 or 10 times larger integrated luminosity, respectively, and investigating significantly larger phase space than in the previous analyses, this work is focused on the detailed comparison of the measurement with the NLO calculations and on the effects of the interactions of the longitudinal photons.

The measurement and QCD analysis described in this Thesis has provided the basis of a recent H1 publication [H104]. Here the analysis is described in more exhaustive way and several issues only briefly mentioned in the publication are addressed and demonstrated in details.

The Thesis is organised as follows. After the introduction to the basic theory of dijet production and various approaches to the description of interactions of virtual photons in Chapter 1, a brief description of the H1 detector is given in Chapter 2. The data sample and selection criteria are defined in Chapter 3. Background subtractions, detector corrections and estimates of various errors are discussed in Chapter 4 and some technical studies on Monte Carlo programs used for the theoretical predictions are performed in Chapter 5. The results are presented and discussed in Chapter 6.

Chapter 1

Theoretical Background

1.1 Perturbative QCD and Renormalisation

The theory of strong interactions, Quantum Chromodynamics (QCD), describes interactions of quarks and gluons. Predictions for scattering processes are usually obtained by Feynman rules based on perturbative expansions derived from the Lagrangian density. Measurable variables (cross-sections) are calculated by summing up a power series in the strong coupling constant, α_s. Higher order contributions to this sum come from Feynman diagrams with internal loops, in which one has to integrate over all possible internal momenta, P. However, these integrals are divergent for $P \to \infty$.

The resulting ultraviolet divergences are regularised in the so-called *regularisation procedure*[1]. As a result, the divergences are absorbed into the definition of the strong coupling constant, so that its value depends on a new dimensional parameter, the so-called i.e. $\alpha_\mathrm{s} = \alpha_\mathrm{s}(\mu_r)$. Also the perturbative coefficients in the power series for any observable, R, depend on μ_r. However, since the renormalisation scale is an arbitrary parameter, the physical quantities cannot depend on its choice, if they are calculated to all orders. Mathematically, this may be expressed by the so-called renormalisation group equation

$$\mu_r^2 \frac{d}{d\mu_r^2} R(\mu_r, \alpha_\mathrm{s}) \equiv \mu_r^2 \frac{\partial R}{\partial \mu_r^2} + \mu_r^2 \frac{\partial \alpha_\mathrm{s}}{\partial \mu_r^2} \frac{\partial R}{\partial \alpha_\mathrm{s}} = 0. \tag{1.1}$$

The dependence of α_s on the renormalisation scale is then given by the β function of QCD, which can be expanded as a power series in α_s

$$\mu_r^2 \frac{d\alpha_\mathrm{s}}{d\mu_r^2} = \alpha_\mathrm{s}\beta(\alpha_\mathrm{s}) = -\beta_0 \frac{{\alpha_\mathrm{s}}^2}{4\pi} - \beta_1 \frac{{\alpha_\mathrm{s}}^3}{16\pi^2} + \dots \tag{1.2}$$

[1] A widely used $\overline{\mathrm{MS}}$ scheme (modified minimal-subtraction scheme [W.A78]) will be employed in this Thesis.

$$\begin{aligned}\beta_0 &= 11 - 2n_f/3 \\ \beta_1 &= 102 - 38n_f/3.\end{aligned}$$

The coefficients β_0 and β_1 are universal for massless quarks, the higher ones, β_2, $\beta_3\ldots$, depend on the renormalisation scheme. The parameter n_f denotes the number of quark flavours active in a given process.

In the one-loop approximation, i.e. neglecting all terms on the right-hand side of Eq. (1.2) except the first one, the coupling constant α_s reads

$$\alpha_s(\mu_r^2) = \frac{\alpha_s(\mu_0^2)}{1 + \beta_0/4\pi \cdot \alpha_s(\mu_0^2)\ln(\mu_r^2/\mu_0^2)}. \tag{1.3}$$

This equation demonstrates two basic features of the QCD, namely that for infinitely large μ_r the coupling constant α_s vanishes (the so-called asymptotic freedom), while for $\mu_r \to \Lambda_{\text{QCD}}$ the coupling diverges, which seems to be responsible for the confinement of partons inside hadrons[2].

As already mentioned, observables R, when computed up to all orders of perturbation theory, cannot depend on the arbitrary renormalisation scale. In reality, however, usually only a few first terms in the power series are calculable, and the resulting sum therefore does depend on the choice of μ_r and the renormalisation scheme. The residual scale dependence should be estimated as part of the theoretical uncertainty of the quantity. The conventional method of doing so is to vary scales between $\mu_r/2$ and $2\mu_r$.

1.2 Factorisation, PDF and Evolution Equations

Interactions of single partons in perturbative QCD can be calculated only at short distances (in *hard* collisions) where $\alpha_s(\mu_r)$ is sufficiently small. In contrast to that, at large distances (i.e. for interactions with low momentum transfers) partons are bound to colourless hadrons, where perturbative theory is no longer applicable. The momentum distribution functions of these partons, usually called *parton distribution functions (PDF)*[3], therefore cannot be calculated within the perturbative QCD. So far, they can be obtained only from measurements. The PDFs are process-independent characteristics of the corresponding hadron.

According to the *factorisation theorem* of QCD [Alt82, CSS88], the cross section of interacting hadrons can be expressed as a convolution of the perturbatively calculable partonic cross section and the non-perturbative parton distribution functions, summed over all contributing partons.

[2]However, the confinement is not yet really understood since it concerns a perturbatively non-calculable region.

[3]The notation adopted in this Thesis is the following: PDF of a hadron h, i.e. the probability of finding a parton i inside the hadron h carrying a fraction x of the hadron's longitudinal momentum, is denoted as $D_{i/h}(x, \mu_f)$.

Also gluon emissions off the valence quarks in a hadron lead to divergences. The contribution of gluons with the transverse momenta[4] approaching zero, i.e. $k_\perp \to 0$, introduces the so-called *collinear* and *infrared* divergences. These can be absorbed into a definition of the *dressed* parton distribution functions according to a given prescription called *factorisation scheme*. The procedure introduces a new scale μ_f, *the factorisation scale*. It can be interpreted as the upper limit on the transverse momentum $k_\perp$ below which parton emissions are included in the redefined PDF of a given hadron. The PDFs are then defined within the given factorisation scheme[5] only.

In analogy to the case of the renormalisation group equation (1.1), there is an expression which guarantees the independence of any observable, when calculated to all orders of α_s, on the choice of μ_f. One of the most common expressions satisfying this equation are the DGLAP evolution equations [GL72, Lip75, AP77, Dok77], a system of coupled differential equations describing the μ_f dependence of the PDFs. In the case of nucleons, they can be written in the form

$$\begin{aligned}
\frac{d\Sigma(x,\mu_f)}{d\ln\mu_f^2} &= P_{qq}\otimes\Sigma + P_{qG}\otimes G \\
\frac{dG(x,\mu_f)}{d\ln\mu_f^2} &= P_{Gq}\otimes\Sigma + P_{GG}\otimes G \\
\frac{dq_{NS}(x,\mu_f)}{d\ln\mu_f^2} &= P_{qq}\otimes q_{NS},
\end{aligned} \tag{1.4}$$

where $P_{ij}(x,\mu_f)$ are splitting functions calculable in powers[6] of α_s

$$P_{ij}(x,\mu_f) = \frac{\alpha_\mathrm{s}(\mu_f)}{2\pi}P_{ij}^{(0)}(x) + \left(\frac{\alpha_\mathrm{s}(\mu_f)}{2\pi}\right)^2 P_{ij}^{(1)}(x) + \cdots \tag{1.5}$$

and $\Sigma(x,\mu_f)$, $G(x,\mu_f)$ and $q_{NS}(x,\mu_f)$ are the singlet, gluon and non-singlet distribution functions, respectively. The singlet and non-singlet functions are defined as combinations of quark, $q_i(x,\mu_f)$, and antiquark, $\overline{q_i}(x,\mu_f)$, densities

$$\begin{aligned}
\Sigma(x,\mu_f) &\equiv \sum_{i=1}^{n_f}\left[q_i(x,\mu_f) + \overline{q_i}(x,\mu_f)\right] \\
q_{NS}(x,\mu_f) &\equiv q_i(x,\mu_f) - \overline{q_i}(x,\mu_f)\,.
\end{aligned} \tag{1.6}$$

The splitting functions $P_{ij}(x,\alpha_\mathrm{s})$ have the intuitive physics interpretation as the probabilities of finding a parton of type i in a parton of type j with a fraction x of the longitudinal momentum of the parent parton.

[4]The transverse momentum $k_\perp$ is taken relative to the motion of the initial parton before the gluon radiation.

[5]Again, the $\overline{\mathrm{MS}}$ scheme will be used as the factorisation scheme in relevant calculations of this Thesis.

[6]Only the first terms $P_{ij}^{(0)}(x)$ are unique, while all higher-order ones depend on the choice of the factorisation scheme.

The DGLAP evolution equations (1.4) are usually solved by a numerical integration in the x space or analytically in the moment space. Once we know (i.e. deduce from the measurement) the parton densities at certain value of μ_f, the evolution equations enable us to extrapolate them to any value of μ'_f. A complication of this procedure comes from the fact that the evolution of a single parton distribution function involves mixing with other parton flavours. Furthermore, it requires the full knowledge of all parton distributions over the range of $x \in \langle x_{\min}, 1\rangle$.

1.3 PDF and Evolution Equations of the Photon

The interactions of virtual photons are far from trivial, contrary to what one could naively expect from the well understood theory of QED, describing the photon as rather simple elementary object without any internal structure. Such simple picture can be used only at very short distances, or in other words, at large photon virtualities. At larger distances photon exhibits hadron-like properties, because it has enough time to fluctuate into quark-antiquark ($q\overline{q}$) pairs before interacting with some other particle. The two apparently different faces of the photon mix together, and their relative importance changes with the photon virtuality, Q^2. In the case of real or quasi-real photons, $Q^2 \ll \Lambda^2_{\mathrm{QCD}}$, it is necessary to introduce parton distribution functions in the spirit of the hadronic physics [CT00a].

The point-like coupling of photons to $q\overline{q}$ pairs, described by QED, generates inhomogeneous terms on the right-hand side of the DGLAP evolution equations of the photon

$$\begin{aligned}
\frac{d\Sigma(x_\gamma,\mu_f)}{d\ln\mu_f^2} &= \delta_\Sigma k_q + P_{qq}\otimes\Sigma + P_{qG}\otimes G \\
\frac{dG(x_\gamma,\mu_f)}{d\ln\mu_f^2} &= k_G + P_{Gq}\otimes\Sigma + P_{GG}\otimes G \\
\frac{d\hat{q}_{NS}(x_\gamma,\mu_f)}{d\ln\mu_f^2} &= \delta_{NS}k_q + P_{qq}\otimes\hat{q}_{NS},
\end{aligned} \tag{1.7}$$

where $\hat{q}_{NS}(x,\mu_f) \equiv \sum_{i=1}^{n_f}(e_i^2 - \langle e^2\rangle)\,[q_i(x,\mu_f)+\overline{q_i}(x,\mu_f)]$, $\delta_{NS} \equiv 6n_f(\langle e^4\rangle - \langle e^2\rangle^2)$, $\delta_\Sigma \equiv 6n_f\langle e^2\rangle$ and k_q, k_G are splitting functions similar to those defined in Eq. (1.5),

$$\begin{aligned}
k_q(x_\gamma,\mu_f) &= \frac{\alpha}{2\pi}\left[k_q^{(0)}(x_\gamma) + \frac{\alpha_s}{2\pi}k_q^{(1)}(x_\gamma) + \left(\frac{\alpha_s}{2\pi}\right)^2 k_q^{(2)}(x_\gamma) + \cdots\right] \\
k_G(x_\gamma,\mu_f) &= \frac{\alpha}{2\pi}\left[\qquad\qquad \frac{\alpha_s}{2\pi}k_G^{(1)}(x_\gamma) + \left(\frac{\alpha_s}{2\pi}\right)^2 k_G^{(2)}(x_\gamma) + \cdots\right].
\end{aligned} \tag{1.8}$$

Here $k_q^{(0)} = x_\gamma^2 + (1-x_\gamma)^2$, while the higher order splitting coefficients depend on the choice of the factorisation scheme.

The general solution of the evolution equations (1.7) can be written as the sum of a particular solution of the full inhomogeneous equations and the general solution of the corresponding homogeneous equations. A subset of the former, resulting from the resummation of series of diagrams shown in Fig. 1.1, are called *point-like*, the latter *hadron-like* solutions[7].

There is an infinite number of these solutions, and the separation of the photon PDF into the point- and hadron-like parts is therefore ambiguous. However, one can choose one of them by introducing an additional parameter μ_f^0 defined as the value of the factorisation scale at which the point-like solutions vanish. The general solution of the evolution equations (1.7) then reads

$$D_{i/\gamma}(x_\gamma, \mu_f) = D^{\mathrm{PL}}_{i/\gamma}(x_\gamma, \mu_f, \mu_f^0) + D^{\mathrm{HAD}}_{i/\gamma}(x_\gamma, \mu_f, \mu_f^0), \tag{1.9}$$

where $D^{\mathrm{PL}}_{i/\gamma}(x_\gamma, \mu_f, \mu_f^0)$ and $D^{\mathrm{HAD}}_{i/\gamma}(x_\gamma, \mu_f, \mu_f^0)$ stand for *the perturbatively calculable* point-like part and *perturbatively uncalculable* hadron-like part of the photon PDF, respectively.

The higher value of μ_f^0 in Eq. (1.9), the less parton emissions is included in the point-like part of the photon PDF and put to the hadron-like part instead. Quantitative aspects of the different μ_f^0 setting can best be illustrated by comparing SaS1D and SaS2D parameterisations [SS96] of the photon PDF, since they provide the two parts of the photon PDF separately for different values of μ_f^0 (for a detailed comparison see [CT00a]).

Equation (1.9) describes real photons with $Q^2 = 0$. It can be generalised also to the virtual photons, in which case the PDF depends in addition on Q^2:

$$D_{i/\gamma}(x_\gamma, \mu_f, Q^2) = D^{\mathrm{PL}}_{i/\gamma}(x_\gamma, \mu_f, \mu_f^0, Q^2) + D^{\mathrm{HAD}}_{i/\gamma}(x_\gamma, \mu_f, \mu_f^0, Q^2) \tag{1.10}$$

The main difference between the point- and hadron-like components concerns their virtuality dependence [Chy01, CT00a, SS96]. Whereas the hadron-like parts fall-off with Q^2 rapidly and essentially independently of μ_f, like $(\mu_f^0)^4/Q^4$, the point-like ones decrease much more slowly, like $\ln(\mu_f^2/Q^2)$.

Graphs contributing to the point-like part of the photon distribution function are shown in Fig. 1.1. In order to study the effects of gluon radiation in the $D^{\mathrm{PL}}_{i/\gamma}(x_\gamma, \mu_f, \mu_f^0, Q^2)$, i.e. the effects of the QCD improvement of the photon PDF, one can use only the QED part of the point-like PDF defined as a pure QED splitting of photon into a $q\overline{q}$ pair. In our kinematic region, i.e. for quark masses $m_q^2 \ll Q^2$, these QED splitting terms have the form

$$\begin{aligned}
D^{\mathrm{QED}}_{q_i/\gamma^*_T}(x_\gamma, \mu_f, \mu_f^0, Q^2) &= \frac{\alpha}{2\pi} 3e_i^2 \left(x_\gamma^2 + (1-x_\gamma)^2\right) \ln \frac{\mu_f^2}{x_\gamma Q^2}, && (1.11)\\
D^{\mathrm{QED}}_{q_i/\gamma^*_L}(x_\gamma, \mu_f, \mu_f^0, Q^2) &= \frac{\alpha}{2\pi} 3e_i^2 4x_\gamma(1-x_\gamma), && (1.12)\\
D^{\mathrm{QED}}_{g/\gamma^*_{T,L}}(x_\gamma, \mu_f, \mu_f^0, Q^2) &= 0, && (1.13)
\end{aligned}$$

[7]The terminology used in this Thesis has been adopted from a recent note [Chy01] that attempts to unify number of sets of notions and definitions associated to photon interactions. The term "hadron-like" is sometimes called "VDM" (Vector Meson Dominance Model), the expression "point-like" is an equivalent for the term "anomalous".

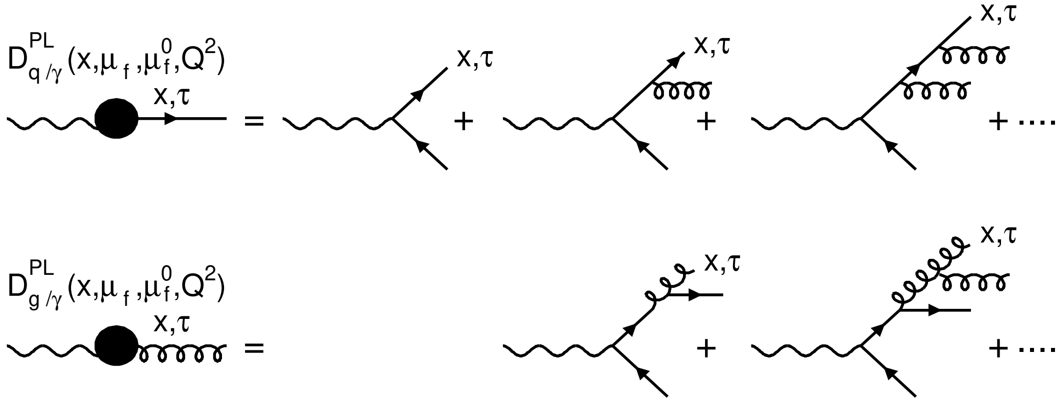

Figure 1.1: Diagrams defining the point-like parts of the quark and gluon distribution functions of the virtual photon. The resummation involves integration over parton virtualities $\tau \leq \mu_f^2$.

where the terms γ_T^* and γ_L^* denote transversely and longitudinally polarised virtual photons discussed in Sections 1.5 and 1.6. The full expressions of Eqs. (1.11) and (1.12) with exact Q^2 dependence that exhibits the correct threshold behaviour for Q^2/m_q^2 can be found in [CT00a].

In the case of photoproduction and massless quarks, the integral over the photon splitting term $\gamma \to q\overline{q}$ in the expression for the cross section diverges and it must be therefore subtracted and included in the PDF of the resolved quasi-real photon[8]. Contrary to that, in the kinematic region of virtual photons investigated in this Thesis, i.e. for $\Lambda_{QCD}^2 \ll Q^2$, the corresponding integral stays finite, since the nonzero photon virtuality shields off the singularity originating from the $\gamma^* \to q\overline{q}$ splitting. The concept of the photon structure can therefore be in principle discarded. In practical perturbative QCD applications, the photon structure can be neglected only for $Q^2 \gtrsim 1\,\mathrm{GeV}^2$. Nevertheless, this concept turns out to be very useful even for virtualities above 1 GeV, because their point-like parts include the resummation of parts of higher-order QCD corrections. These higher-order effects are not included in the existing fixed-order NLO QCD programs. Employing the resolved photon interactions thus provides predictions qualitatively and quantitatively different [Tas99] from the pure NLO direct calculations.

[8]In the following, the letter γ stands for the real or quasi-real photon, whilst γ^* is reserved for the case of virtual photons.

1.4 Kinematics of Electron Proton Scattering

The kinematics of electron-proton deep inelastic scattering is schematically shown in Fig. 1.2 and defined in Eq. (1.14).

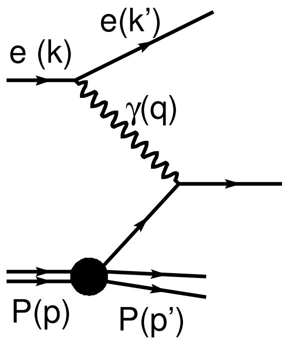

$$\begin{aligned} s_{ep} &= (p+k)^2 \\ Q^2 &= -q^2 = -(k-k')^2 \\ x_B &= \frac{Q^2}{2(p\cdot q)} \\ y &= \frac{p\cdot q}{p\cdot k} \\ W^2 &= (p+q)^2 \end{aligned} \quad (1.14)$$

Figure 1.2: Kinematics of *ep* scattering.

In the naive parton model, the Bjørken scaling variable, x_B, can be interpreted as the momentum fraction of the incoming proton carried by the struck parton. More details on the kinematics of *ep* scattering can be found in the textbook [Chyed].

In addition to the quantities defined in Eq. (1.14) for a general *ep* collision, the dijet events are characterised by variables specifying the two leading jets. The usual choice are their transverse energies, $E^*_{T\,1}$, $E^*_{T\,2}$, pseudorapidities[9], η^*_1, η^*_2, and the azimuthal angles, ϕ_1, ϕ_2. Sometimes, it is convenient to describe dijet events by means of the variable $x_\gamma^{\rm jets}$, defined as

$$x_\gamma^{\rm jets} = \frac{\sum\limits_{j=1,2}(E^*_j - p^*_{z,j})}{\sum\limits_{\rm hadrons}(E^* - p^*_z)}\ , \quad (1.15)$$

where the sum in the numerator runs over the two leading jets, the sum in the denominator includes the full hadronic final state and E^*, p^*_z denote the energy and longitudinal momentum of a hadron (jet) in the centre-of-mass frame. Neglecting the masses of the partons and beam particles, $x_\gamma^{\rm jets}$ represents the fraction of the photon four-momentum carried by the parton involved in the hard scattering. In this approximation, $x_\gamma^{\rm jets}$ can be identified with the variable x_γ used in Section 1.3.

[9]Transverse energies and pseudorapidities in this Thesis are measured with respect to the photon-proton axis. The star symbol "$*$" denotes variables calculated in the γp centre-of-mass frame. See footnote 2 on page 32 for the definition of pseudorapidity.

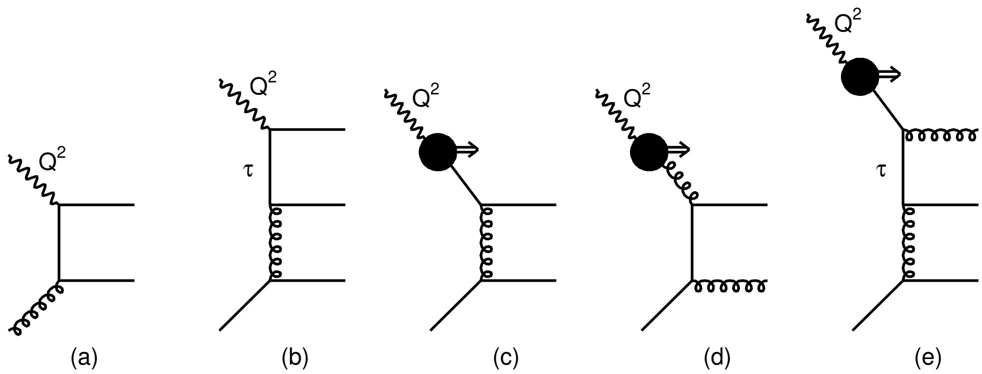

Figure 1.3: Examples of diagrams of dijet production at HERA (incoming electrons and protons not shown): (a), (b) LO and NLO direct photon interactions respectively; (c), (d) LO resolved photon interactions with quark and gluon coming from the photon side; (e) NLO resolved photon diagram. The variable τ denotes the virtuality of the exchanged quark from the photon or parton splitting.

1.5 Cross Section of Dijet Events in the DGLAP Scheme

Present knowledge of the photon structure comes from experiments at ep and e^+e^- colliders, where incoming leptons act as sources of photons. At ep accelerator HERA, effects related to the photon structure can be investigated via the measurement of the cross sections of dijet events, in which a photon emitted by the incoming electron interacts with a parton from the proton producing two partons (i.e. jets) in the final state. The transverse energy, of the jets, E_T, provides a natural choice of the hard scale needed for the perturbative QCD calculations. Correspondingly, the factorisation and renormalisation scales are often identified with E_T of the hardest jet. The same is done in this Thesis.

The cross section of dijet production in our kinematic region is in principle given by the direct photon contribution, illustrated in the diagrams in Figs. 1.3 a, b, and expressed as

$$\sigma^{\mathrm{DIR}} \sim \sum_j D_{j/p} \otimes \sigma_{ej}, \tag{1.16}$$

$$\text{where} \qquad \sigma_{ej} = c_{ej}^{(1)} \alpha_s + c_{ej}^{(2)} \alpha_s^2 + \cdots \,. \tag{1.17}$$

Here σ_{ej} denotes the cross section for a collision between the incoming electron and a parton j from the proton, $c_{ej}^{(1)}, c_{ej}^{(2)}, \cdots$ are coefficients of an expansion of σ_{ej} in powers of α_s and $D_{j/p}$ stands for the PDF of the proton satisfying the DGLAP equations (1.4). The term $c_{ej}^{(1)} \alpha_s$ defines the LO cross section, $c_{ej}^{(1)} \alpha_s + c_{ej}^{(2)} \alpha_s^2$ is the NLO one.

The measurements of dijet cross section in photoproduction and also several recent analyses of the dijet production in the low Q^2 region [H100, ZEUS00, H103c] have convincingly shown that the LO direct photon contribution lies significantly below the data if $Q^2 \ll E_T^2$.

The NLO calculations, exemplified by the diagram in Fig. 1.3 *b*, bring the theoretical prediction closer to the data [H103c], however, the description is still not perfect. Also a recent paper [H102b] dealing with single jet cross sections indicates that the NLO calculations do not completely describe measured single jet production at low Q^2 in part of the phase space. Large values of the so-called k-factors, i.e. the ratio of NLO/LO predictions for the cross sections, and high sensitivity of the predicted jet cross-sections to variations of the factorisation and renormalisation scales [H102b, H103c] strongly suggest the need for higher-order (i.e. $c_{ej}^{(3)}, c_{ej}^{(4)}, \cdots$) terms in Eq. (1.17).

However, as a full calculation beyond NLO is not available, it makes sense to construct some approximate procedure for resummation of the dominant terms at higher orders of direct photon contribution in Eq. (1.17). In the region $\Lambda^2_{\mathrm{QCD}} \ll Q^2 \ll E_T^2$ these terms at m-th order are of the type

$$\alpha\alpha_s^m \ln^{m-1}(\mu_f^2/Q^2) \qquad \text{for} \quad \gamma_T^* \tag{1.18}$$

$$\alpha\alpha_s^m \ln^{m-2}(\mu_f^2/Q^2) \qquad \text{for} \quad \gamma_L^* \tag{1.19}$$

where $m \geq 2$ and γ_T^* and γ_L^* are the transverse and longitudinally polarised virtual photons, respectively. This reflects the fact that in part of the phase space, the upper vertex of the diagram in Fig. 1.3 *b* can be viewed at as a splitting of the photon into a $q\overline{q}$ pair. Taking into account subsequent emissions of partons from this $q\overline{q}$ pair, the terms (1.18) and (1.19) can be resummed into the point-like part of the photon PDF described in Eqs. (1.9) and (1.10). Such resummation has been done for instance for D_{i/γ_T^*} in [SS96] and for D_{i/γ_L^*} in [Chy00b], both of them used later on in this Thesis. Note that for $m = 2$, Eqs. (1.18) and (1.19) correspond to the QED part of the point-like PDFs of the photon, specified in Eqs. (1.11) and (1.12), convoluted with the LO partonic cross section.

Consequently, one can calculate the resolved photon contribution to dijet cross section in ep collisions, corresponding to the graphs shown in Fig. 1.3 c, d, e, as

$$\sigma^{\mathrm{RES}} \sim \sum_{k=T,L} f_k \otimes \sum_{i,j} D_{i/\gamma_k^*} \otimes D_{j/p} \otimes \sigma_{ij}, \tag{1.20}$$

$$\text{where} \qquad \sigma_{ij} = c_{ij}^{(1)}\alpha_s^2 + c_{ij}^{(2)}\alpha_s^3 + \cdots . \tag{1.21}$$

The indexes i, j runs over all partons in the photon and proton respectively, σ_{ij} is the partonic cross section and f_T, f_L denote the fluxes of exchanged transverse and longitudinally polarised virtual photons, respectively[10]:

$$f_T(y,Q^2) = \frac{\alpha}{2\pi}\left[\frac{2(1-y)+y^2}{y}\frac{1}{Q^2} - \frac{2m_e^2 y}{Q^4}\right], \tag{1.23}$$

$$f_L(y,Q^2) = \frac{\alpha}{2\pi}\left[\frac{2(1-y)}{y}\frac{1}{Q^2}\right]. \tag{1.24}$$

The total dijet cross section is then given as a sum of $\sigma^{\rm DIR}$ at a given fixed-order calculation and the corresponding $\sigma^{\rm RES}$, approximating higher-order contributions. Care must be taken when adding the contribution of the LO resolved photon diagram (Fig. 1.3 *c*) to the NLO direct photon term (Fig. 1.3 *b*). To avoid double counting, the photon splitting term, which would be singular for the real photon, must be subtracted from the NLO direct photon contribution[11] before adding the resolved photon contribution.

As a check on the consistency of this approach, in Section 6.1.2 we show that in a large part of our kinematic region, the NLO direct calculations (Fig. 1.3 *b*) are reasonably well approximated by the sum of the LO direct (Fig. 1.3 *a*) and LO resolved photon contributions (Fig. 1.3 *c*), provided the simplest expression, namely that given by the pure QED splitting of the photon into a $q\overline{q}$ pair, specified in Eqs. (1.11) and (1.12), is used for the photon PDF.

1.6 Specific Features of the Longitudinal Photons

For many years, the longitudinally polarised photons have been ignored in the resolved photon interactions. Up to now, there is only one Monte Carlo (MC) generator, PYTHIA, which deals with this kind of interactions. Even in this program, the longitudinal photons are simulated just in an approximate way: the PDF of the longitudinal photon is substituted by a PDF of the transverse photon reweighted by a simple multiplicative expressions [FS00] depending on y, Q^2 and μ_f. Such procedure completly ignores the different x_γ dependence of PDFs for transverse and longitudinal photons. The difference in the x_γ dependencies will be demonstrated later in this section[12].

[10]Note that the expression (1.16) can be approximated by a formula analogous to Eq. (1.20):

$$\sigma^{\rm DIR} \sim \sum_{k=T,L} f_k \otimes \sum_j D_{j/p} \otimes \sigma_{\gamma j} \tag{1.22}$$

Equation (1.22), contrary to Eq. (1.16), is less precise and neglects interference terms of the two polarisation states of the exchanged photon. This is the reason why Eq. (1.16) is the preferred choice in majority of the Monte Carlo generators.

[11]In this Thesis, the term "direct contribution" denotes the direct photon contribution before the subtraction of the splitting term, whilst "direct subtracted contribution" after the subtraction.

[12]In order to overcome the deficit of MC generators suitable for the analysis of longitudinal photons, we have modified the MC generator HERWIG such that it includes correct expressions of the flux and PDF of γ_L^*. More details are presented in Section 1.8.

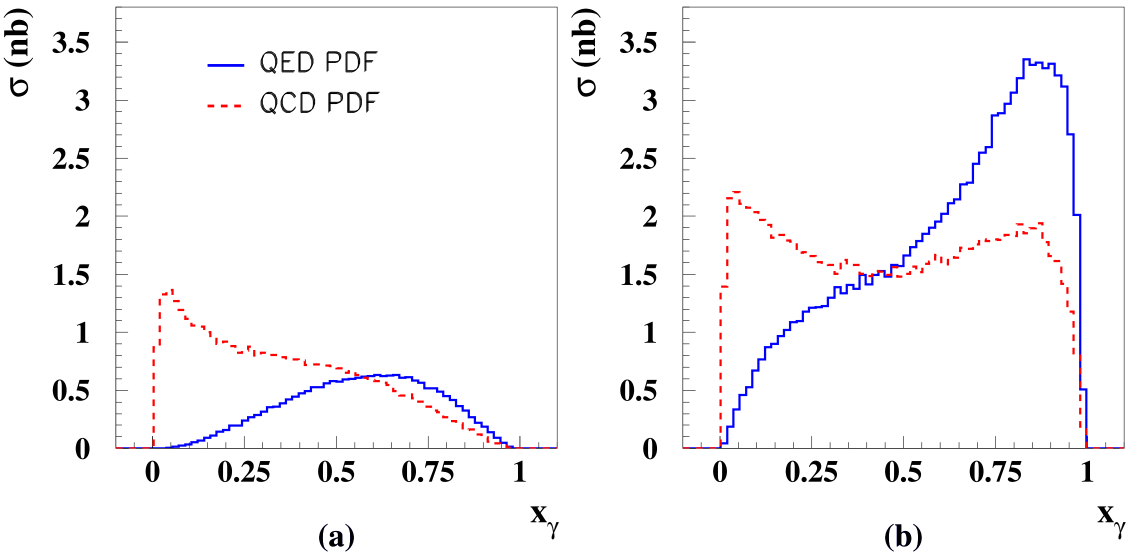

Figure 1.4: HERWIG simulation of dijet cross section of longitudinal (a) and transverse (b) resolved photon interactions for jets with $E_T > 5\,\mathrm{GeV}$ in the region of $1.4 < Q^2 < 2.4\,\mathrm{GeV}^2$. The variable x_γ corresponds to the photon momentum fraction carried by the interacting parton. More details are given in the text.

The reason why longitudinal photons have been so far omitted in the resolved interactions is easy to understand. Due to the gauge invariance and contrary to transverse photons, cross sections of longitudinally polarised photons must vanish for $Q^2 \to 0$. On the other hand, the resolved interactions vanish, with respect to the direct ones, for large values of Q^2 regardless of the photon polarisation. However, as shown e.g. in [CT00b], there is an intermediate region of low Q^2 (i.e. $Q^2 \simeq 1\,\mathrm{GeV}^2$), where the contribution of longitudinal photons appears to be quantitatively important. This is also indicated in Fig. 1.4, which shows a MC prediction of the cross sections of resolved photon dijet production for transverse and longitudinal photons in the region of $1.4 < Q^2 < 2.4\,\mathrm{GeV}^2$. The cross sections were calculated by HERWIG for both QED (Eqs. (1.11) and (1.12)) and QCD-improved (SaS1d [SS96] and J.Chýla [Chy00b]) PDFs of γ_T^* and γ_L^*. One can see that the contribution of longitudinally polarised resolved photons is significant with respect to the transverse one. It is also clearly visible that the x_γ dependence of the cross sections for γ_L^* is quite differet from that of γ_T^*, which is just a consequence of Eqs. (1.11) and (1.12) for the photon PDF. In contrast to the transverse photons, the peak in the x_γ distribution for longitudinal photons is shifted to significantly lower values. We can also see that the QCD corrections due to the generation of gluon emissions in the photon PDF decrease the cross section at large x_γ and increase it at low x_γ.

Another difference between the interactions of γ_T^* and γ_L^* arises from the expressions of the fluxes in Eqs. (1.23) and (1.24). Figure 1.5 shows the dependence of both fluxes on

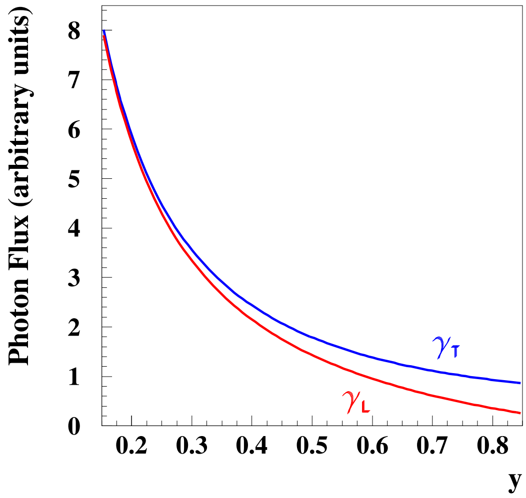

Figure 1.5: Fluxes of transversely and longitudinally polarised virtual photons in the region of $0.15 < y < 0.85$ and $Q^2 = 10\,\mathrm{GeV}^2$.

y. While for $y \to 0$ both transverse and longitudinal fluxes are approximately the same, the longitudinal flux vanishes for $y \to 1$. This fact, together with the different dependence of D_{i/γ_T^*} and D_{i/γ_L^*} on Q^2, μ_f and x_γ in principle allows us to separate effects of γ_T^* and γ_L^* experimentally.

More details about the interactions of longitudinally polarised virtual photons can be found in [FS00, CT00b, CT01].

1.7 Cross Section of Dijet Events in the CCFM Scheme

The DGLAP evolution equations, introduced in Section 1.2, effectively resum leading terms of parton emissions off the proton proportional to $\alpha_s \ln(Q^2)$, which is also reflected in the requirement of the $k_\perp$ ordering[13] of partons in the parton cascade emitted off the proton. However, once the *ep* centre-of-mass energy is large enough, another terms proportional to $\alpha_s \ln(1/x)$ appear to be dominant in part of the phase space of low x.

Different approaches have been developed to cope with the low x physics. The most common one, called BFKL [KLF76, KLF77, BL78], is based on a concept of *unintegrated* PDF of the proton and on the ordering in the longitudinal momentum fractions $x_0 > x_1 > \cdots > x_n$, where x_0 belongs to the parton closest to the proton and x_n enters the hard scattering subprocess, as indicated in Fig. 1.6. In contrast to the standard DGLAP scheme introduced in Section 1.2, the unintegrated PDFs depend in addition to x and μ_f on a new variable, namely the $k_\perp^2$.

[13]The variable $k_\perp$ denotes the transverse momentum of a parton with respect to the incoming proton.

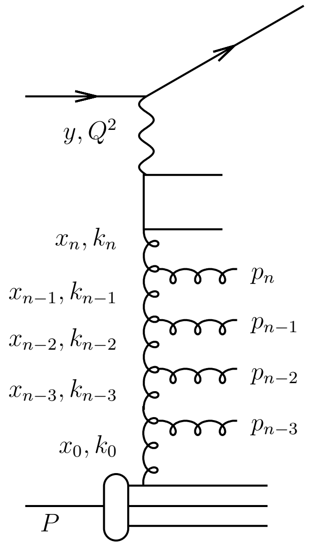

Figure 1.6: Electron proton interaction with multi-gluon emission. The t-channel gluon momenta are given by k_i, while the gluons emitted in the initial state cascade have the momenta p_i.

For several reasons [JS01], the BFKL scheme appears unsuitable for implementation into the Monte Carlo programs that generate complete particle interactions with the full hadronic final state. The problems can be overcome in an alternative CCFM [Cia88, CFM90a, CFM90b, Mar95] evolution scheme, which resums also large logarithmic terms $\alpha_s \ln(1/(1-x))$ in addition to the $\alpha_s \ln(1/x)$ ones. It introduces angular ordering of emissions in order to treat correctly gluon coherence effects. In the limit of asymptotically large energies, it is almost equivalent to BFKL [FS98, Web98, Sal99], but on the other hand it is also approaching the DGLAP evolution for large x and high Q^2.

Similarly to the case of DGLAP scheme, the dijet ep cross section in CCFM scheme can be factorised [CCH91, CE91, GLR83, LRSS91] into a partonic cross section and the universal parton distribution functions [x02]

$$\sigma^{\mathrm{CCFM}} = \sum_j \int \frac{dz}{z}\, d^2k_\perp\, \hat{\sigma}_{ej}(\frac{x}{z}, k_\perp^2)\; A_{j/p}(x, k_\perp^2, \hat{\mu}_f^2), \tag{1.25}$$

where, contrary to DGLAP, the partonic cross sections $\hat{\sigma}_{ej}$ have to be taken off-shell (i.e. $k_\perp$ dependent), and the unintegrated parton distributions, $A_{j/p}(x, k_\perp^2, \hat{\mu}_f^2)$, depend on the transverse momentum $k_\perp$ of parton j emitted off the proton. The sum in Eq. (1.25) goes over all partons j in the proton and $\hat{\mu}_f$ is the factorisation scale related to the maximum angle allowed in the evolution.

The CCFM evolution scheme thus provides a natural framework for the implementation of $k_\perp$-unordered initial state QCD cascades. Partons with the largest $k_\perp$ may come from any emission in the cascade, and not necessarily, contrary to the DGLAP framework, from the hard subprocess. This can lead to events with a similar topology to that of the resolved photon interactions in the DGLAP approximation, in which hard jets are accompanied by softer partons from the photon remnant.

1.8 Monte Carlo Programs

The aim of an experiment is either to test some existing theory or to provide a new information for the development and improvement of our theoretical knowledge. The measurements in the high energy physics are rather complicated and usually do not make possible direct comparisons of the data with some analytically calculable predictions provided by theorists. Instead, the measured data are usually compared with predictions performed by the so-called Monte Carlo (MC) generators, which combine well-founded theories (e.g. the Standard Model) with some approximative procedures (e.g. the technique of perturbative expansions) and phenomenological models (e.g. of the hadronisation processes).

Since contemporary detectors such as H1 are complicated systems, it is even impossible to compare the measured data directly with the output of the MC generators. Programs which simulate the response of the H1 detector have to be applied on events generated by MC programs. This allows us to determine precisely an influence of the limited detector acceptance, granularity, death material or ineffective detector components during the measurement, and to perform appropriate corrections thereof.

In this Thesis, the following MC models are used:

HERWIG [M$^+$92, C$^+$99] is a general purpose MC event generator, applicable to a wide range of hard processes and collisions. The interactions are factorised into separate components: the hard sub-process, perturbative initial and final state showers, non-perturbative hadronisation, resonance decays and the beam-remnant fragmentation. Great emphasis is put on a very sophisticated partonic treatment of the perturbatively calculable QCD showers. On the other hand, the description of the perturbatively uncalculable hadronisation is done by relatively simple "cluster hadronisation model" [Web84], in which colourless clusters, formed during the hard scattering and parton shower stages, decay into the hadrons.

By default, HERWIG can not simulate resolved photon processes with longitudinally polarised photons. This became possible only in the modified version of HERWIG done by Jiří Chýla, who implemented the options of generating the longitudinal photon flux specified in Eq. (1.24) and calculated a set of the QCD-improved D_{i/γ^*_L}.

The remnants of incoming hadron, i.e. those constituent partons which do not participate in the hard subprocess, can optionally undergo a "soft underlying event" interaction modelled on soft minimum bias hadron-hadron collisions. The model used for this purpose is based on the minimum-bias $p\overline{p}$ event generator of the UA5 Collaboration, modified to make use of the HERWIG cluster fragmentation algorithm [M$^+$92, C$^+$99]. The soft underlying event leads to a redistribution of the originally high longitudinal energy into the transverse direction. The probability that a resolved photon event contains the soft underlying activity, has been adjusted in the simulation using the parameter PRSOF such that the energy flow in and around the jets are well described. This will be illustrated in Section 5.4.

RAPGAP [Jun95] has been originally developed for the simulation of diffractive events in *ep* interactions. Nowadays it is extended to several other processes, including jet production. Standard hard scattering partonic cross sections and parton showers are combined with LUND string fragmentation model using the JETSET package [Sjo86, SB87, Sjo94]. RAPGAP can also generate the resolved photon processes, however only for the transverse polarisation of virtual photons. Contrary to HERWIG, it does not include any model of soft underlying interactions. On the other hand, it enables us to simulate initial and final state QED radiation[14], which allows us to correct the measured cross sections for the QED radiation effects (see Section 4.5.1).

PYTHIA [Sjo94] is a powerful event generator developed for a large variety of interactions. It can generate all direct, resolved γ_T^* and resolved γ_L^* processes. Optionally it also provides simulation of QED radiation as well as additional interactions within the single γp scattering event. These so-called *multiple interactions* are modelled using the leading order $2 \to 2$ parton-parton scattering process. This is a different approach to soft underlying events simulated in HERWIG.

Since dijet cross section predicted by PYTHIA in our kinematic region is significantly lower than the data (see Section 6.2), we use it just as an alternative additional model.

PYTHIA [Sjo94], PHOJET [Eng95, ER96], LEPTO [IER97] are another MC generators employed for different purposes in this Thesis: PYTHIA and PHOJET have been used for an estimate of photoproduction background (see Section 4.4), LEPTO for the determination of hadronisation corrections (see Section 5.2). All three programs can generate events with the full hadronic final state.

CASCADE [JS01, Jun02a] is the first-ever-built MC generator with the full simulation of hadronic final state that is not based on the DGLAP evolution equations. It uses unintegrated gluon distribution functions [Jun02b] of the proton satisfying the CCFM evolution equations instead. The hadronisation is done via the LUND string fragmentation model. Even though quarks are considered in the CCFM evolution equations, CASCADE uses only gluons in both the unintegrated proton structure and parton cascade emitted off the proton.

In addition to the MC generators based on the LO cross sections, which allow us to simulate complete *ep* interactions including the hadronic final state, there are also MC programs based on the NLO cross sections. The main advantage of these programs is their smaller theoretical uncertainty and higher predictive power with respect to the LO

[14]Only in the direct photon interactions.

MC generators. Unfortunately, the NLO programs are not yet capable of hadronic final state simulation, and consequently they can not be directly compared to the experimental results. This drawback is usually overcome by an estimate and a subsequent correction of the hadronisation effects, usually done with the help of the LO MC generators. The correction procedure is however not defined unambiguously, as will be discussed in Section 5.2.

The following NLO programs are used in this analysis:

DISENT [CS97] is a NLO program for calculating dijet cross sections at the parton level. It is based on the so-called dipole subtraction method [ERT81] for regularisation of soft and collinear divergences. The factorisation scale, μ_f, was set to $\mu_f = \langle E_T \rangle = 9\,\mathrm{GeV}$, since the program does not allow the user to set $\mu_f = E_T$. However in our kinematic region, the difference between the results obtained with $\mu_f = E_T$ and $\mu_f = \langle E_T \rangle$, tested using JETVIP, is very small. DISENT does not include resolved photon interactions.

JETVIP [Pot99, Pot00] is a NLO parton level program based on the phase-space slicing method. Contrary to DISENT, it generates also the resolved photon interactions, however only for the transversal polarisation. The big disadvantage of this program is the strong dependence of its predictions on the slicing parameter y_s, which is just a technical parameter used internally by the program. We have performed systematic investigations of the stability of JETVIP calculations with respect to variation of y_s, which is presented in Section 5.3. We set $y_s = 0.003$ in all calculations, since JETVIP predictions are most stable around this value.

In all analytical calculations, like JETVIP or DISENT, the massless partons entering the hard process are taken to be exactly collinear with the beam particles. This means that the kinematics of the parton splitting is not treated properly, namely the transverse momentum of the hard partons is underestimated in the NLO calculations. Contrary to that, the MC generators like HERWIG or RAPGAP are designed to take into account the exact kinematics of the parton splitting, which can lead to a numerically significant increase of the dijet cross section when some cut on the minimum transverse energy of the jets is applied.

The actual parameter setting of the MC programs employed in this Thesis is summarised in Table 1.1.

The following notation is used in the next sections in order to distinguish different levels of MC predictions:

- **Parton level** denotes partonic final state after the hard scattering process. It can be predicted by MC generators with or without the initial and final state QCD parton showers.

Parameters	**HERWIG**	**RAPGAP**	**CASCADE**	**DISENT**	**JETVIP**
Version	6.4	2.8	1.2	—	2.1
Proton PDF	CTEQ5L [L+97]	CTEQ5L	J2003 (set 1) [Jun02b]	CTEQ6M	CTEQ6M
Photon PDF	SAS1D [SS96]; [Chy00b] for γ^*_L	SAS1D	—	—	SAS1D
Formula for α_s	one-loop	one-loop	one-loop	two-loop	two-loop
Nr. of active flavours	5	5	4	5	5
PRSOF	10%	—	—	—	—
μ_r	$\sim 1.1 p_T$	$\sqrt{(p_T^2 + m_q^2)}$	$\sqrt{(p_T^2 + m_q^2)}$	$E^*_{T\,1}$	$E^*_{T\,1}$
μ_f	$\sim 1.1 p_T$	$\sqrt{(p_T^2 + m_q^2)}$	given by ang. ordering	9 GeV	$E^*_{T\,1}$
Hadronisation mechanism	Cluster model	LUND string fragmentation	LUND string fragmentation	—	—

Table 1.1: Parameters of the MC programs. The variable p_T denotes the transverse momentum of the parton with mass m_q outgoing from the hard interaction, and $E^*_{T\,1}$ is the energy of the jet with the highest transverse energy. The parameter PRSOF specifies the fraction of resolved photon events with soft underlying activity.

- **Hadron level** is defined by the final state particles, leptons and hadrons, emerging from the interaction. So far, it can be predicted only by the LO MC programs.
- **Detector level** is an information measured by a detector after final state hadrons and leptons pass it through. In order to get the detector level predictions for MC simulations, the output of MC generators is interfaced to the program simulating the response of the H1 detector. This program, called H1SIM, is based on the GEANT package [ea87].

Chapter 2

Experimental Setup

2.1 HERA

The collider HERA (*Hadron Electron Ring Anlage*) are the first ever constructed electron-proton storage rings. It is located at the DESY laboratory in Hamburg, Germany, and hosts four experiments – H1, ZEUS, HERMES and HERA-B.

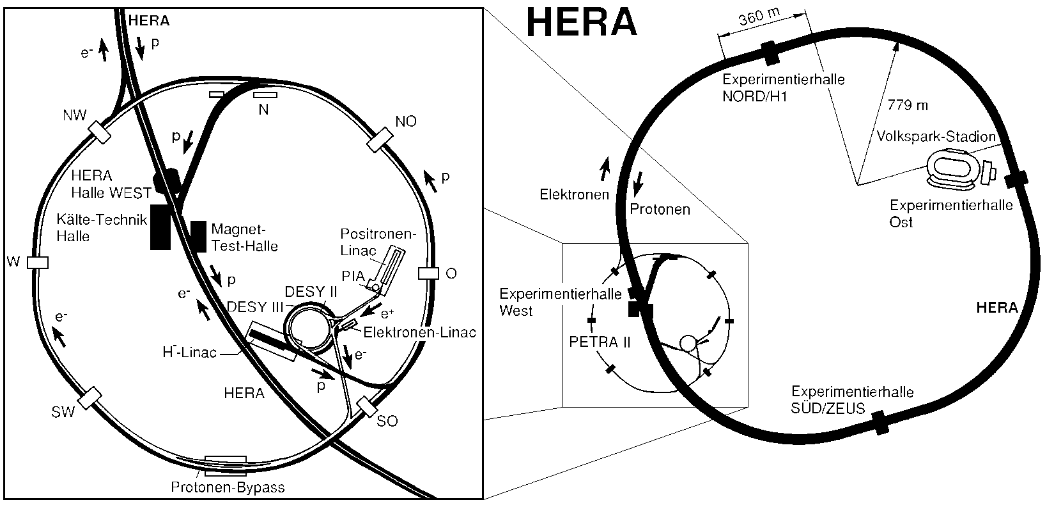

Figure 2.1: Schematic view of the HERA collider

The layout of the HERA facility is depicted in Fig. 2.1. Electrons and protons are accelerated in several pre-accelerators before entering HERA.

HERA itself consists of two storage rings with 6.3 km in circumference, one for the protons of the energy[1] 920 GeV, and the second one for the electrons of 27.55 GeV. Incident particles are kept in bunches with the time distance of 96 ns. The electron bunch length, width and height is about 10 mm, 0.3 mm and 0.04 mm respectively, the proton bunch size reaches 110 mm, 0.3 mm and 0.08 mm.

2.2 The H1 Detector

The H1 detector is designed as a multi-purpose apparatus to study electron-proton collisions in almost hermetic coverage around the beam axis. The limitation comes from the space taken up by the beam pipe itself. Inner space of the H1 detector is described with a coordinate system (x, y, z) in which the nominal interaction point defines the origin, x is the direction to the centre of the HERA ring, y is the upwards direction and z is the direction of the proton beam. The polar, θ, and azimuthal, ϕ, angles are defined correspondingly, so that θ is equal to zero in the proton beam direction and θ equals π in the electron beam direction. The azimuthal angle $\phi = \arctan(y/x)$ is positive for positive values of y.

Since the centre-of-mass system for HERA collisions is boosted along the proton direction, the H1 detector is asymmetric with more instrumentation in the outgoing proton direction, which is referred to as *forward region* in the following.

The layout of the H1 arrangement is displayed on page 25. Around the beam pipe $\boxed{1}$, there are tracking devices $\boxed{2}$ and $\boxed{3}$ made of drift and proportional chambers. SPACAL $\boxed{12}$, a lead scintillating fibre calorimeter, is placed just behind the backward drift chamber. All these detectors are surrounded by the liquid argon calorimeter, which consists of two parts: the electromagnetic section $\boxed{4}$, made of lead absorber plates, and the hadronic section $\boxed{5}$, produced of stainless steel plates.

A superconducting cylindrical coil $\boxed{6}$ with a diameter of 6 m provides the magnetic field of 1.15 T. This field is compensated by another superconducting coil $\boxed{7}$ in order not to influence the HERA beam. The iron return yoke of the magnet is laminated and filled with limited streamer tube detectors, in which a small fraction of hadronic energy leaking out of the liquid argon calorimeter is registered here. Muons are identified and measured by muon chambers $\boxed{9}$ inside and outside the iron yoke. Measurement of muon tracks in the forward region is done in a toroid equipped with drift chambers $\boxed{9}$ and $\boxed{11}$.

The H1 detector is completed with the small angle electron and photon detectors dedicated to the luminosity measurement placed at 33.4 m and 102.9 m, respectively, from the nominal interaction point in the HERA tunnel.

Since the whole H1 apparatus is described in detail in [H197c, H197d], only the major components of H1 relevant for the physics analysis presented in this Thesis will be

[1]In 1998, an upgrade of HERA machine was performed leading to an increase of the proton beam energy from 820 GeV to 920 GeV.

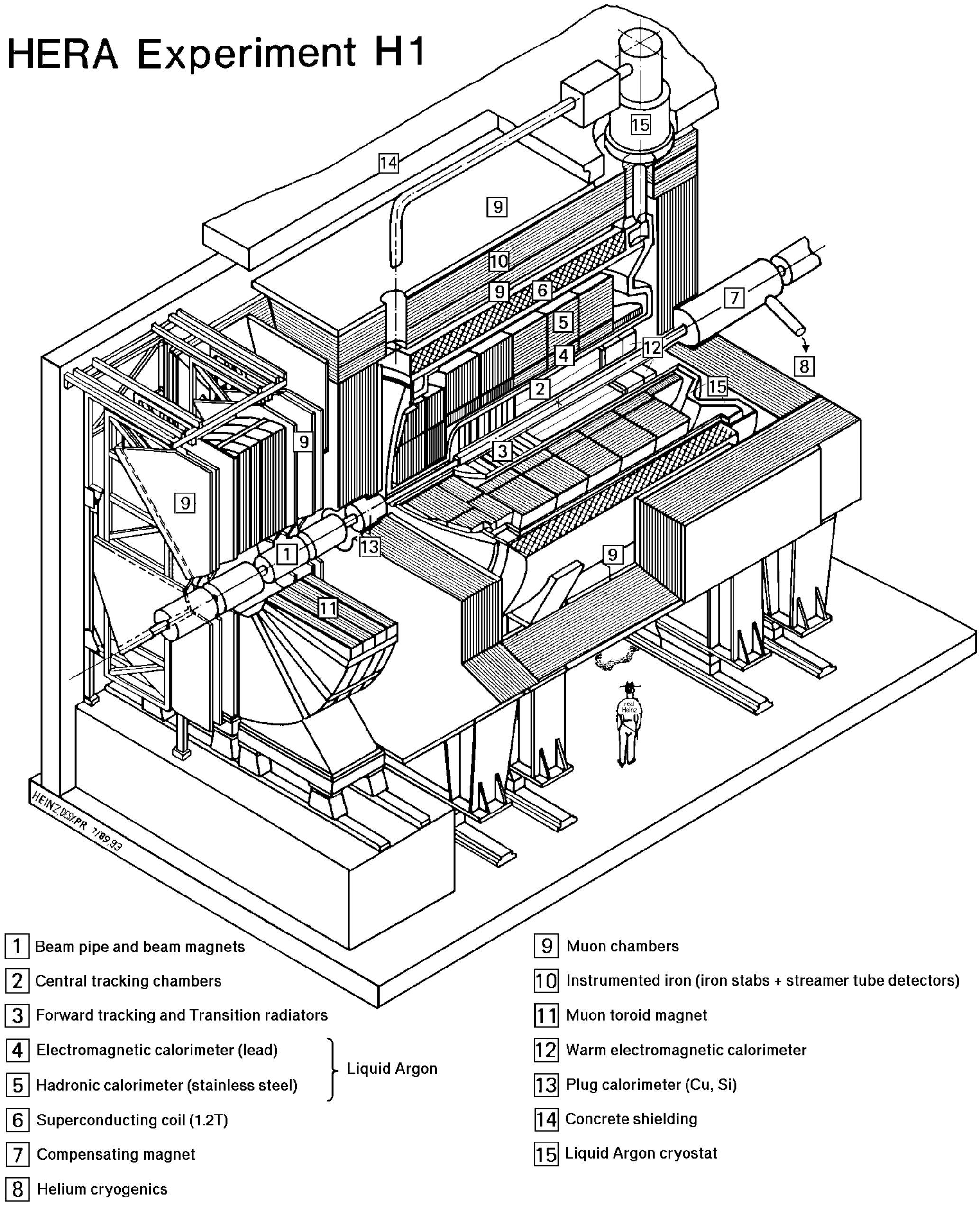
HERA Experiment H1
1 Beam pipe and beam magnets
2 Central tracking chambers
3 Forward tracking and Transition radiators
4 Electromagnetic calorimeter (lead)
5 Hadronic calorimeter (stainless steel)
Liquid Argon
6 Superconducting coil (1.2T)
7 Compensating magnet
8 Helium cryogenics
9 Muon chambers
10 Instrumented iron (iron stabs + streamer tube detectors)
11 Muon toroid magnet
12 Warm electromagnetic calorimeter
13 Plug calorimeter (Cu, Si)
14 Concrete shielding
15 Liquid Argon cryostat

discussed in the following.

2.2.1 Calorimeters

There are four calorimeters in the central part of the H1 detector providing the energy measurement – the Liquid Argon Calorimeter (LAr), the Backward Lead Scintillating Fibre Calorimeter (SPACAL), the Tail Catcher (TC) and the Plug Calorimeter (PLUG).

The liquid argon calorimeter (LAr)

The LAr calorimeter provides the primary measurement of the hadronic energy in H1. Also the scattered electrons with the energy above $\simeq 100$ GeV are detected in this device. The liquid argon technique has been chosen since it makes possible to reach a good stability, simplicity of calibration, fine transverse granularity and homogenity of the signal response. The LAr calorimeter covers polar angles $4^\circ < \theta < 154^\circ$ and is housed in a large cryostat inside the magnet solenoid. Placing the cryostat inside the magnet has the advantages of reducing both the size and weight of the calorimeter and minimising the amount of a dead material in front of the main detector components. The LAr is divided into inner electromagnetic and outer hadronic sections segmented into wheels, which sit on rails inside the cryostat. Each wheel is further azimuthally segmented into eight identical octants. The total thickness of the electromagnetic section varies between 20 and 30 radiation lengths and the depth of hadronic part varies from 4.7 to 8 nuclear interaction lengths.

In total there are 45 000 cells building up the LAr calorimeter. Such a fine granularity is very helpful for shower shape studies and efficient particle identification. The energy resolution of the electromagnetic part, measured in beam tests [Group94], is $\sigma_{em}(E)/E \simeq (11\%/\sqrt{E})+1\%$, where E is the energy of the incident particle in GeV. Similarly the resolution of the hadronic section was determined [Group93] to be $\sigma_{had}(E)/E \simeq (50\%/\sqrt{E}) + 2\%$.

SPACAL

SPACAL, a lead scintillating fibre calorimeter, also consists of the electromagnetic and hadronic sections. The primary goal of the fine-grained electromagnetic section is a high precision measurement of the energy and impact point of the scattered electrons in the angular range $153^\circ \leq \theta \leq 178^\circ$. The hadronic section aims to measure possible electromagnetic shower leakages from the electromagnetic section and to determine hadronic energy flow in the backward region. The depth of approximately one nuclear interaction length of the hadronic section together with one nuclear interaction length of the electromagnetic part improves the e/π separation capabilities. The resolution of the electromagnetic part [H1 96] is $\sigma_{em}(E)/E \simeq (7\%/\sqrt{E}) + 1\%$ and of the hadronic one $\sigma_{had}(E)/E \simeq (30\%/\sqrt{E}) + 2\%$. For triggering purposes, the SPACAL is divided into the inner ($R_{\mathrm{SPAC}} < 30\,\mathrm{cm}$) and outer ($R_{\mathrm{SPAC}} > 30\,\mathrm{cm}$) rings. More information about the SPACAL can be found in [H1 96, H1 97].

The tail catcher (TC)

The TC calorimeter provides a coarse energy measurement of hadronic showers leaking out of the LAr. It covers almost the entire 4π solid angle. The energy resolution of the TC has been measured at the beam tests with pion beams to be $\sigma(E)/E \simeq 100\%/\sqrt{E}$. Due to problems with the simulation of the TC, which does not properly describe the measured data, this detector is not used in our analysis

The plug calorimeter (PLUG)

PLUG covers the extreme forward direction $0.6^\circ < \theta < 3^\circ$ and is designed to minimise the gap in acceptance for energy flow between the beam pipe and the most forward part of the LAr calorimeter. Its primary task is to reduce the losses in transverse momentum measurements due to hadrons emitted close to the beam pipe. The design value of the PLUG resolution is $\sigma(E)/E \simeq 150\%/\sqrt{E}$. For similar reasons as the TC, the PLUG is not employed in this analysis.

2.2.2 Tracking

The tracking system of H1 is shown in Fig. 2.2, and provides simultaneously triggering, track reconstruction and particle identification. The tracking detectors are split into three major components – the central tracker (CTD), the forward tracker (FTD) and the backward drift chamber (BDC). Each of them is optimised for tracking and triggering in its angular region.

The forward and central trackers contain both drift chambers and multi-wire proportional chambers (MWPCs – CIP and COP). The latter ones have worse spatial resolution than the drift chambers due to a limitation of the wire spacing. On the other hand, they are suitable for triggering purposes thanks to a rapid response times to the passage of charged particles. The drift chambers are used for a precision measurement of tracks – the resolution in the drift direction reaches $150\,\mu\mathrm{m}$. The coordinate parallel to the wire can be determined by charge division of the pulses recorded at each end of the wire, to a precision of $\sim 1\%$ of the wire length.

The Central Tracker

The track reconstruction in the central region is based on two large concentric drift chambers, CJC1 and CJC2 shown in Fig. 2.3, covering the polar angle range $15^\circ < \theta < 165^\circ$. The chambers have wires strung parallel to the beam axes, i.e. in the z-direction. Because of the high magnetic field, only tracks with transverse momentum $\geq 0.15\,\mathrm{GeV}$ will pass

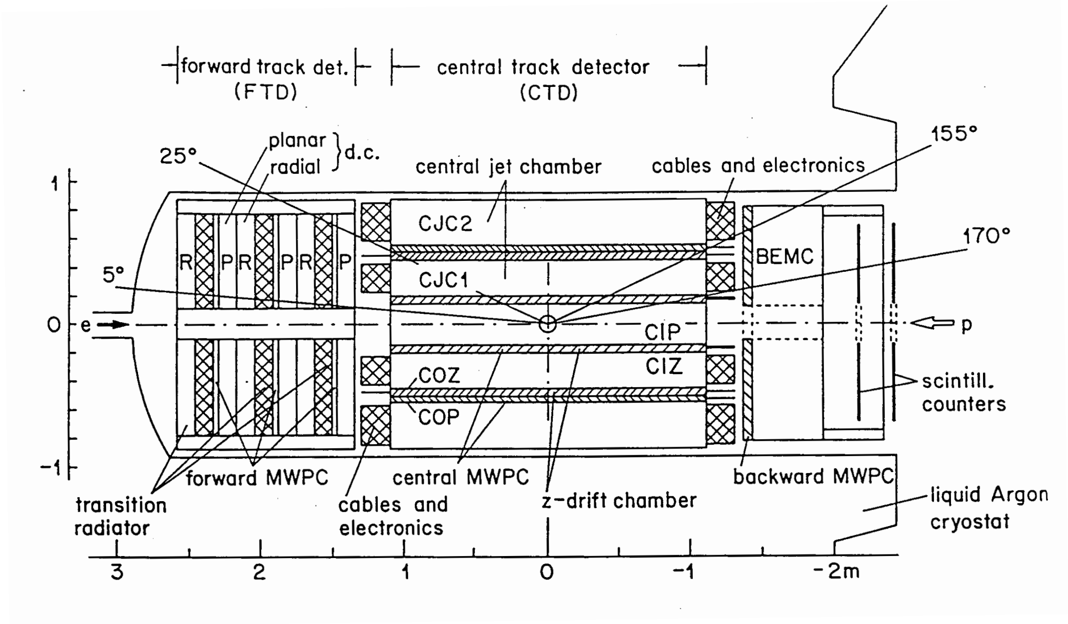

Figure 2.2: The r-z view of the H1 tracking system. Figure was taken from [H197c, H197d].

through both chambers. The momentum and angular resolutions are $\sigma_p/p^2 \leq 0.01\,\mathrm{GeV}^{-1}$ and $\sigma_\theta = 21\,\mathrm{mrad}$. The space resolution is about $170\,\mu$m for x and y coordinates and 22 mm in the z direction.

Two thin drift chambers, the central inner (CIZ) and central outer (COZ) z-chambers complement the measurement of the charged track momenta. The sense wires are perpendicular to the beam axis. These two chambers provide track resolution about $300\,\mu$m in z and $30-60$ mm in x and y direction. Linking these track elements to those obtained from the CJCs gives the final accuracy on both longitudinal and transverse momentum components.

The Forward Tracker

The forward tracking detector (FTD) provides an accurate measurement of charged particles in the forward direction defined by $5^\circ < \theta < 30^\circ$. It consists of three supermodules. Each of them includes three differently oriented planar drift chambers, a multiwire proportional chamber (FWPC), a passive transition radiator and a radial wire drift chamber. The planar drift chambers contain wires parallel to the beam direction and provide homogeneous spatial resolution in the plane perpendicular to the beam direction. They thus allow us to accurately measure polar angles. The FWPC has been designed for fast triggering and the radial chambers provide accurate r and ϕ information.

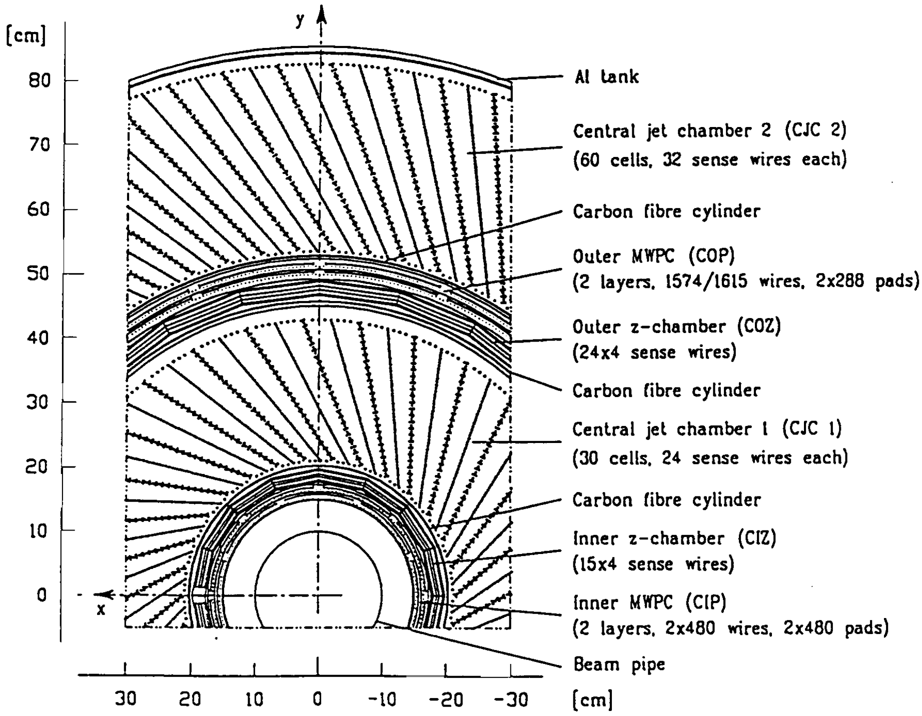

Figure 2.3: Section of the central tracking system. Figure was taken from [H197c, H197d].

The backward drift chamber

The backward drift chamber (BDC) provides track segments for final state electrons entering the backward region. It consists of four double layers of drift chambers divided into eight octants with sense wires strung parallel to the radial direction. The double layers are rotated by $11.5°$ with respect to one another for better spatial resolution, which is $\sigma_r = 0.4\,\text{mm}$ and $\sigma_\phi = 0.8\,\text{mm}$.

2.2.3 Luminosity System

The main task of the luminosity system is a fast on-line relative luminosity measurement and precise off-line absolute luminosity measurement in the interaction region. It also provides electron beam monitoring for the HERA machine group, tagging of photoproduction events and energy measurement of electrons scattered under very small angles and of photons from the initial state radiation.

The luminosity is determined from the rate of theoretically well understood Bethe-Heitler reaction $ep \to ep\gamma$. There is a large source of background to the Bethe-Heitler events due to the bremsstrahlung of the electrons on the residual gas in the beam pipe, $eA \to eA\gamma$. The background events are expected to add 10% contribution to the $ep \to ep\gamma$

cross section. However, they can be rather easily subtracted using data from the so-called *electron pilot bunches*. The pilot bunches do not have any counter-bunches to collide with, therefore the electrons confined in them interact with the residual gas only. The luminosity can then be calculated as

$$L = \frac{R_{tot} - (I_{tot}/I_0)R_0}{\sigma_{vis}}$$

where R_{tot} is the total rate of all events registered in the luminosity detector, R_0 is the rate from the electron pilot bunches, I_{tot} and I_0 are the corresponding electron beam currents and σ_{vis} is the visible part of the $ep \to ep\gamma$ cross-section corrected for the luminosity detector acceptance and trigger efficiency.

The luminosity system is in more detail described in [H197c, H197d]. The precision of the luminosity measurement in the years 1999 and 2000, relevant for our analysis, is 1.5%. This value is also taken as the overall normalisation uncertainty of our final result.

2.2.4 Trigger System

The aim of the trigger system is to reduce the rate of the background events and to keep as many interesting *ep* collisions as is realistically possible to save on a permanent data storage. The background events, which are orders of magnitude more frequent than the rate of *ep* interactions, originate from collisions of the beam particles with the beam-pipe walls or the residual gas, and from the synchrotron radiation and the cosmic rays.

Due to low *ep* cross section, large proton and electron beam currents are needed for statistically significant measurements. The beams have a multi-bunch structure with the bunch-crossing time of 96 ns. Therefore a fast complex trigger system splitted into several levels with the increasing complexity has been constructed. The next trigger level is only started if a given event has been accepted by the preceding one.

Basic triggers[2] consist of *trigger elements*, which are made of electronic signals from dedicated parts of the H1 detector. The trigger may be activated for example by a few tracks reconstructed in the tracking chambers, by the energy deposit in a calorimeter higher than some threshold value, by the successfully reconstructed interaction vertex, etc. By an appropriate set of triggers, various physics processes may be selected for off-line analyses.

[2]There are 128 triggers at H1 named *s0, s1, ... s127.*

Chapter 3

Event Sample Selection

3.1 Run Selection Criteria

The data used in this analysis have been collected by the H1 experiment during the years 1999 and 2000, and correspond to the integrated luminosity of $57.6\,\mathrm{pb}^{-1}$. Incoming protons with the energy of 920 GeV collided with electrons or positrons with the energy of 27.55 GeV. The electrons were used in the beginning of 1999, and make about 17% of the integrated luminosity of the analysis. Since July 1999, positrons have been used instead of electrons. In the low Q^2 region employed in our analysis, the difference between e^-p and e^+p interactions leading to dijet production is negligible. We therefore do not distinguish both types of incident lepton beams and treat both data-taking periods as one data sample[1].

The analysis includes only the data taken with fully operational main detector components: the LAr and SPACAL calorimeters, CJC1, CJC2, CIZ, CIP, COP and BDC trackers, the luminosity system and the time-of-flight counters.

3.2 Event Selection Criteria

The cuts employed in the analysis can be divided into two classes, *the phase-space cuts* and *the technical cuts*. The former define the kinematic region of the measurement and are imposed on both detector and hadron level quantities. The latter are just of a minor importance and are applied at the detector level only. They are introduced due to the limited precision, acceptance and other technical restrictions of the detector components. Rather small fraction of events lost due to the technical cuts is corrected for in the unfolding procedure.

[1] The notion "electron" is used for both e^- and e^+ in this Thesis for ease of reading.

3.2.1 The Phase-Space Cuts

The kinematic region is defined by the cuts on the photon virtuality, Q^2, and inelasticity, y, defined in Section 1.4

$$2 < Q^2 < 80\,\mathrm{GeV}^2, \tag{3.1}$$

$$0.1 < y < 0.85 \tag{3.2}$$

and by the cuts on the hadronic final state containing at least two jets. The jet transverse energies, E_T^*, and pseudorapidities, η^*, are calculated relative to the γp collision axis in the photon-proton centre-of-mass frame[2]. The so-called *leading jets*, i.e. the two jets with the highest transverse energies, are required to fulfil the conditions

$$E^*_{T\,1} > 7\,\mathrm{GeV}, \quad E^*_{T\,2} > 5\,\mathrm{GeV}, \tag{3.3}$$

$$-2.5 < \eta_1^* < 0, \quad -2.5 < \eta_2^* < 0, \tag{3.4}$$

where $E^*_{T\,1}$, $E^*_{T\,2}$ stand for the transverse energies of jets with the highest and second highest E_T^*, respectively, and η_1^*, η_2^* for their pseudorapidities. The asymmetric E_T^* cuts avoid regions of instability in the NLO calculations [KK96, KK97, FR97, CS03] (see Section 5.6).

In order to calculate the quantities used in for cuts (3.1) and (3.4), the electron candidate and jets have to be identified and their energy reconstructed. The corresponding procedures are described in the following two subsections.

The Electron Identification

The scattered electrons are identified via the standard H1 algorithm, *the electron finder* called QESCAT. It is based mainly on the information from the SPACAL and BDC detectors. The algorithm proceeds in the following way:

1. The neighbouring electromagnetic SPACAL cells with the energy deposit above some threshold value are grouped into *clusters*. The energy of the cells within a cluster is summed up.

2. The cluster with the maximum transverse energy is selected as an electron candidate, if its total energy is above 3 GeV.

3. The cluster shape has to fulfil criteria on the electromagnetic shower, namely the cluster radius, R_{cl}, has to be smaller than 3.5 cm, and the energy deposited in the corresponding hadronic part of the SPACAL, $E_{e,\mathrm{had}}$, must not exceed 0.5 GeV or

[2] The pseudorapidity is defined by $\eta^* \equiv -\ln(\tan\theta^*/2)$ where θ^* is the polar angle of the jet axis with respect to the γp axis. Negative values of η^* correspond to the photon fragmentation region (the so-called *backward direction*). The pseudorapidity in the photon-proton centre-of-mass frame is shifted on average by -2.3 units with respect to the pseudorapidity in the laboratory frame.

15% of the energy measured in the electromagnetic section of the SPACAL, $E_{e,\mathrm{elmg}}$. The purpose of these cuts is to reduce fake signals from charged hadrons of the final state that could mimic the scattered electron.

4. The cluster has to lay well inside the active part of the SPACAL, i.e. its distance from the beam line, R_{SPAC}, must be larger than 10 cm and smaller than 67 cm. The energy deposited in the innermost part of the SPACAL, in the so-called SPACAL veto layer, E_{veto}, has to be smaller than 1 GeV.

5. There must be a track reconstructed in the BDC matching the SPACAL cluster within the distance $|R_{\mathrm{SPAC}} - R_{\mathrm{BDC}}| < 1.5\,\mathrm{cm}$.

6. If in the acceptance of the CIP detector, the electron candidate has to be validated by hits in CIP.

7. Some cells close to the beam pipe with unnaturally high rate caused by the synchrotron radiation have to be avoided, therefore an additional fiducial cut is imposed on the electron candidates with distance from the beam axis below 12 cm ($R_{\mathrm{SPAC}} < 12\,\mathrm{cm}$). The azimuthal angles of such candidates, ϕ_e have to fulfil: $\phi_e < 45°$, $180° < \phi_e < 270°$ or $\phi_e > 340°$.

8. At the end, the four-vector representing the positron candidate is constructed from the calibrated cluster energy measured by the SPACAL and from the track information obtained by the BDC.

The variables Q^2 and y are determined using the scattered electron energy and polar angle [BEK91]:

$$Q^2 = 4E_e^0 E_e \cos^2(\theta_e/2),$$

$$y = 1 - (E_e/E_e^0)\sin^2(\theta_e/2),$$

where E_e^0 and E_e denote the energies of the primary and scattered electron, respectively, and θ_e is the polar angle of the scattered electron measured in the laboratory frame.

The Jet Reconstruction

Once the electron has been identified, jets are reconstructed out of the remaining particles of the final state. We use the k_t longitudinally invariant jet algorithm in the inclusive mode [CDSW93, ES93], which proceeds in the following steps:

1. For each particle i as well as for each pair of particles i, j, the distances d_i and $d_{i,j}$ are calculated as

$$d_i = (E^*_{T,i})^2 \qquad \text{and} \qquad d_{i,j} = \min((E^*_{T,i})^2, (E^*_{T,j})^2)\frac{R^2_{i,j}}{R^2_0}\ ,$$

where $R_{i,j}^2 = (\Delta\eta_{i,j}^*)^2 + (\Delta\phi_{i,j})^2$ and $R_0 = 1$ according to the recommendation of [CDSW93, ES93].

2. The smallest value of all d_i and $d_{i,j}$ is labelled as $d_{\min}$.

3. If $d_{\min}$ was selected from the set of d_i, the particle i is marked as "jet", and removed from the list of particles.

4. If $d_{\min}$ was selected from the set of $d_{i,j}$, the particles i and j are merged into a new particle n using the E_T scheme

$$E_{T,n}^* = E_{T,i}^* + E_{T,j}^*, \tag{3.5}$$

$$\eta_n^* = \frac{E_{T,i}^*\eta_i^* + E_{T,j}^*\eta_j^*}{E_{T,i}^* + E_{T,j}^*}, \tag{3.6}$$

$$\phi_n = \frac{E_{T,i}^*\phi_i + E_{T,j}^*\phi_j}{E_{T,i}^* + E_{T,j}^*}. \tag{3.7}$$

5. The procedure is stopped when no particles are left, i.e. all particles are included in jets.

At the hadron level of MC generators, the jet algorithm runs over final state particles. At the detector level, however, the individual particles can not be reconstructed due to the limited resolution of calorimeters, and only some approximation of particles is possible. The so-called *combined objects* [H197b] are used for this purpose. These objects are reconstructed by combining tracking and calorimeter information in a procedure that avoids double counting. The tracks fitted to the primary vertex are extrapolated to the calorimeter. The energy deposits in the electromagnetic (hadronic) calorimeters within 30 cm (50 cm) from the extrapolated track are discounted, until the total energy of the excluded calorimeter clusters exceeds the energy of the track or until all cells within the given radius are removed. This procedure is done for all tracks with energy below 2 GeV, where the tracker information is more precise than the measurement of calorimeters. Low energy isolated clusters in the calorimeters, originating from the detector or electronic noise, are also rejected. The tracks below 2 GeV and any calorimeter deposits that are not associated with a track or rejected as noise are accepted as the combined objects.

The jet algorithm is applied to particles or combined objects boosted into the photon-proton centre-of-mass frame.

3.2.2 The Technical Cuts

The technical cuts are applied at the detector level only. Their purpose is to minimise detector smearing effects, inefficiencies of the measurement and some sources of the background. They should not influence the final results, and if they do, the corresponding

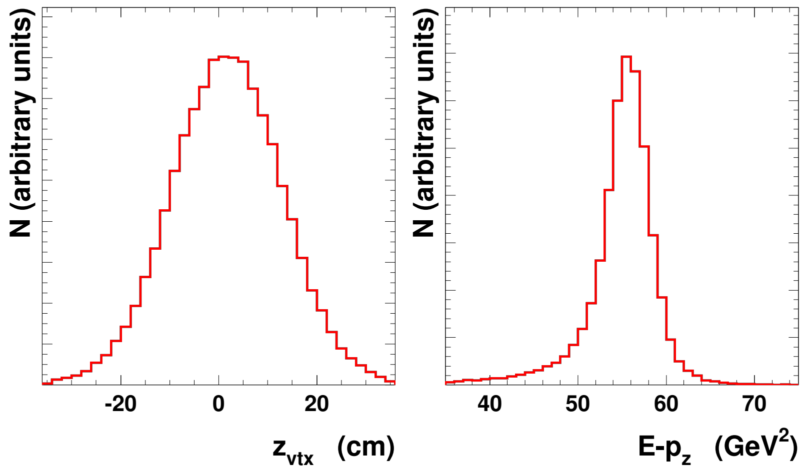

Figure 3.1: Measured z-vertex (left) and $E - p_z$ distribution (right).

uncertainty of the measurement has to be estimated and included in the final systematic error.

Some of the technical cuts, as e.g. the cuts on the electron candidate or on the combined objects, have already been specified in Section 3.2.1, the others are discussed here:

Cut on the z-vertex. In order to avoid interactions of particles outside the beam bunches, and also to remove collisions of beam particles on the residual beam gas, beam walls and collimators, the event vertex must be reconstructed close to the nominal interaction vertex. We therefore impose the condition

$$-35 < z_{\text{vtx}} < 35\,\text{cm}\,, \tag{3.8}$$

where z_{vtx} denotes the z coordinate of the reconstructed event vertex.

$(\mathbf{E} - \mathbf{p_z})$ cut. Due to the momentum conservation law, the sums of the total energy, E, and the z component of the momentum, p_z, over all particles in the event has to be conserved. Consequently, also the difference of $E - p_z$ of initial state particles, which is $920 - 920 + 27.55 - (-27.55)\,\text{GeV} = 55.1\,\text{GeV}$, must be equal to the difference of $E - p_z$ summed over all particles in the final state. Due to the limited precision of the four-momentum measurement of the scattered electron and combined objects, the sum of $E - p_z$ of the final state particles is smeared out around the correct value, as indicated in Fig. 3.1. In the case of photoproduction events, in which scattered electron escapes detection and a charged hadron is misidentified as the electron candidate, the measured $E - p_z$ is shifted to low values. The cut

$$45\,\mathrm{GeV} < \sum E - p_z < 75\,\mathrm{GeV} \tag{3.9}$$

thus provides very effective rejection of the photoproduction background. In addition, this cut suppresses events with the hard QED radiation, in which the incoming electron radiates a highly energetic photon that escapes the detection through the beam pipe.

Trigger selection. Due to the high event rates at HERA and the limitations of computer resources, not all interactions can be saved for the off-line analysis. The interesting events are recorded on the basis of triggers (see Section 2.2.4). The sample of events employed in this Thesis is based on triggers *s9*, *s61* and *s64*:

- **s9:** SPACAL inclusive electron trigger with the energy threshold of 2 GeV. Due to a level 2 validative condition, this trigger is effective in the outer SPACAL ring only (i.e. for $R_{\mathrm{SPAC}} > 30\,\mathrm{cm}$).
- **s61:** SPACAL inclusive electron trigger with the energy threshold of 5.7 GeV in either inner or outer SPACAL ring, z-vertex signature and at least one track with transverse momentum above 800 MeV found by DCrϕ trigger element (see Appendix A).
- **s64:** LAr transverse energy trigger, based on the so-called *LAr trigger towers*, with the energy threshold of 7.2 GeV together with the condition on the energy deposited in the forward modules of the LAr, which has to be larger than 7.5 GeV.

An event was accepted for the analysis if at least one of these three triggers fired. The precise definition of these triggers and the relevant trigger elements is given in Appendix A.

Both phase-space and technical cuts are summarised in Table 3.1.

Phase space cuts	$2.0 < Q^2 < 80\,\mathrm{GeV}^2$
	$0.1 < y_e < 0.85$
	$E^*_{T\,1} > 7\,\mathrm{GeV}, \quad E^*_{T\,2} > 5\,\mathrm{GeV}$
	$-2.5 < \eta^*_1 < 0, \quad -2.5 < \eta^*_2 < 0$
Technical cuts	$45 < E - p_z < 75\,\mathrm{GeV}$
	$\lvert z_{vtx} \rvert < 35\,\mathrm{cm}$
	$R_{\mathrm{cl}} < 3.5\,\mathrm{cm}$
	$E_{e,\mathrm{had}} < 0.5\,\mathrm{GeV}$
	$E_{e,\mathrm{had}}/E_{e,\mathrm{elmg}} < 0.15$
	$E_{\mathrm{veto}} < 1\,\mathrm{GeV}$
	$\lvert R_{\mathrm{SPAC}} - R_{\mathrm{BDC}} \rvert < 1.5\,\mathrm{cm}$
	$10 < R_{\mathrm{SPAC}} < 67\,\mathrm{cm}$
	Fiducial cuts in the SPACAL
	Triggers s9, s61 or s64

Table 3.1: Summary of the phase-space and technical cuts.

Chapter 4

Analysis Procedure

4.1 Electron Calibration

The basic calibration of the SPACAL calorimeter can be done by three independent methods [Mey97, Tza, Dir96]: 1) using the elastically scattered electrons from the *ep* interactions, 2) by cosmic muons, and 3) via the muons from the halo particles accompanying the beams.

Short time fluctuations of the SPACAL calibration are corrected for using the calibrated light signals generated by the system of light-emitting diode (LED) [Jan96].

The final and most precise off-line calibration is determined using the double angle method [BEK91]. The final uncertainty of the electromagnetic energy scale is of the order of 1% [Gla98, Tza], and leads to a systematic error in the determination of the event kinematics and consequently to the deterioration of the Lorenz boost into photon-proton centre-of-mass frame. To check the final SPACAL calibration, the ratio of the scattered electron energy directly measured by the SPACAL over the scattered electron energy measured by the double angle method, E_e/E_{DA}, is shown in Fig. 4.1. The double angle method [BEK91, Gla98] is based on the measurement of two polar angles, the one of the scattered electron and the other one of the scattered quark[1]. Therefore E_{DA} is in the first approximation independent of the energy measurement in the SPACAL and provides a reference scale for the scattered electron energy E_e. Due to statistical fluctuations and the limited precision of a real detector, the ratio is not precisely one but it is smeared out and shifted towards the lower values. The shift in data is, however, well described by the MC simulation, which confirms that the response of the real H1 detector is well reproduced by the simulation program. The dependence of the double ratio $\langle E_e/E_{DA}\rangle_{\mathrm{DATA}}/\langle E_e/E_{DA}\rangle_{\mathrm{MC}}$ on the photon virtuality, shown in Fig. 4.2, further demonstrates the good agreement between the data and MC simulation.

Varying the overall electromagnetic energy scale of the SPACAL by $\pm 1\%$ [Gla98, Tza]

[1]The polar angle of the scattered quark is evaluated as the mean polar angle of the hadronic final state particles.

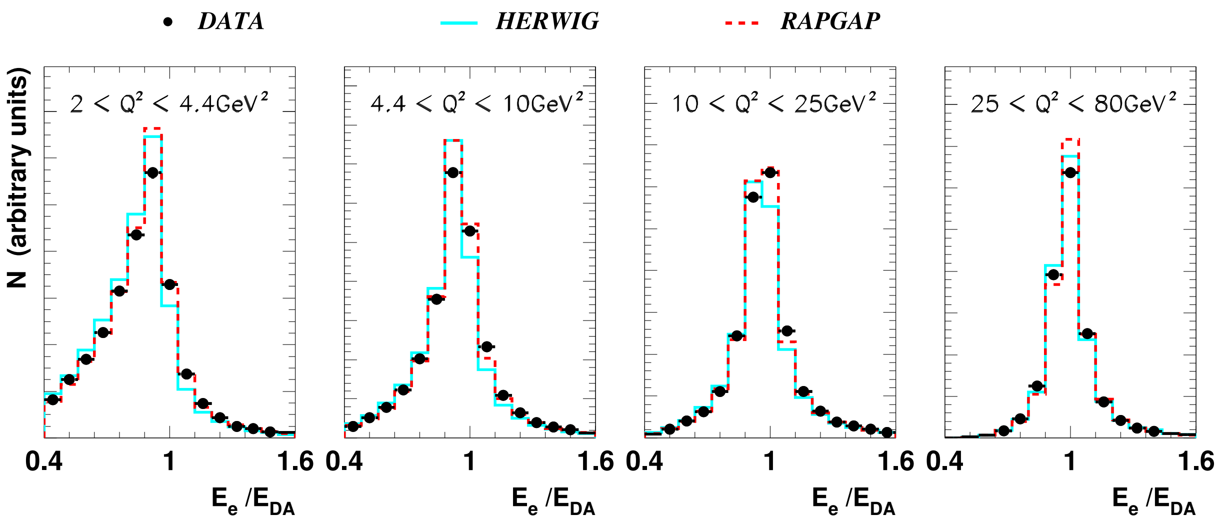

Figure 4.1: The ratio of the scattered electron energy in the SPACAL, E_e, over the energy measured by the double angle method, E_{DA}, for four different regions of Q^2.

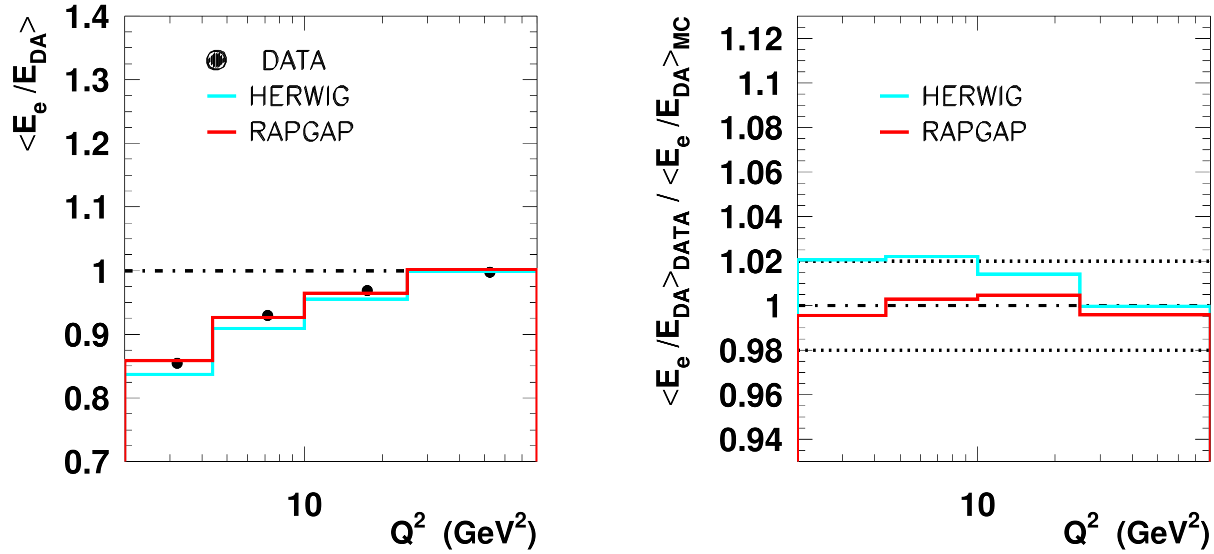

Figure 4.2: Mean values of the E_e/E_{DA} ratia for different Q^2 regions obtained from the distributions shown in Fig. 4.1 *(left)*, and the double ratio $\langle E_e/E_{DA}\rangle_{\mathrm{DATA}}/\langle E_e/E_{DA}\rangle_{\mathrm{MC}}$ *(right)*.

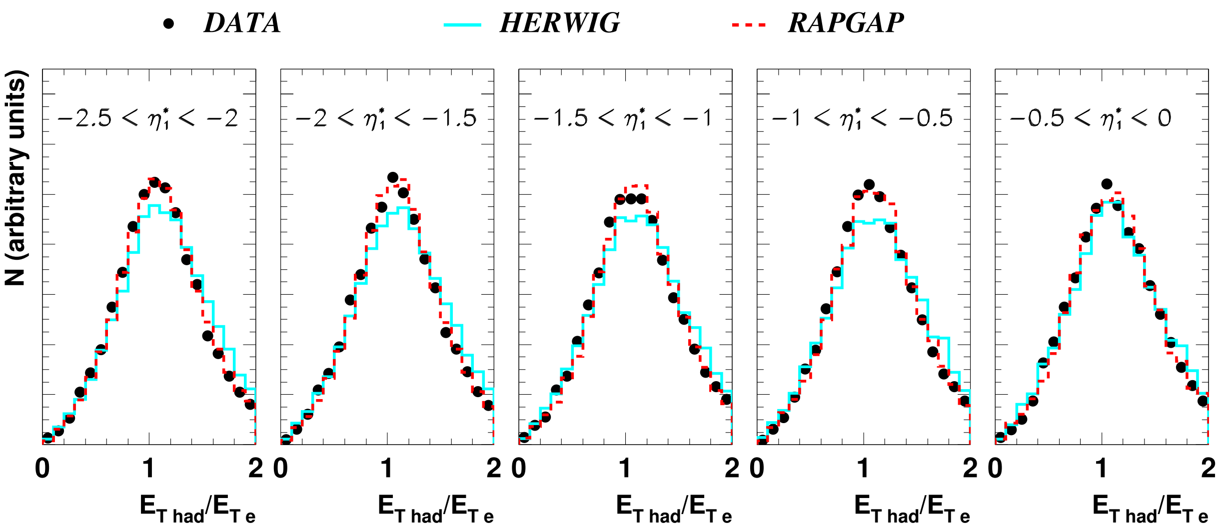

Figure 4.3: The so-called E_T balance, i.e. the ratio of transverse energy of the hadronic final state system, $E_{T\,\mathrm{had}}$, over the transverse energy of the scattered electron, $E_{T\,e}$, for five intervals of the pseudorapidity of the leading jet, η_1^*.

leads to systematic shifts of the final results, presented in Chapter 6, by typically 4%. The size of these shifts, which varies from bin to bin, is taken as the systematic error due to the electromagnetic scale uncertainty.

The polar angle of the scattered electron is measured with a precision of 1 mrad. Variation within this value leads to a 3% (1%) systematic uncertainty of the results in the lowest (highest) Q^2 region.

4.2 Calibration of the Hadronic Final State

Once the electromagnetic calorimetry is well calibrated, we have to check the calibration of the hadronic sector. Due to the momentum conservation, the transverse energy of the scattered electron, $E_{T\,e}$, has to be balanced by the transverse energy of the hadronic final state, $E_{T\,\mathrm{had}}$. This allows us to fix the calibration of the hadronic calorimeters by the electromagnetic energy scale of the SPACAL, which is determined significantly more precisely than the hadronic energy scale. The balance of the hadronic and electromagnetic transverse energies, i.e. $E_{T\,\mathrm{had}}/E_{T\,e}$, presented in Fig. 4.3 in bins of pseudorapidities of the leading jet, η_1^*, is expected to be equal to one. Similarly to the case of E_e/E_{DA}, the statistical fluctuations and the limited precision of the measurement of final state particles smear the distribution of the E_T balance and shift its mean value. However, Fig. 4.3 demonstrates that these detector effects are well reproduced by the MC simulations.

The dependence of the mean values $\langle E_{T\,\mathrm{had}}/E_{T\,e}\rangle$ on the pseudorapidity of the highest E_T jet is presented in the right part of Fig. 4.4. Prediction of RAPGAP agrees very well

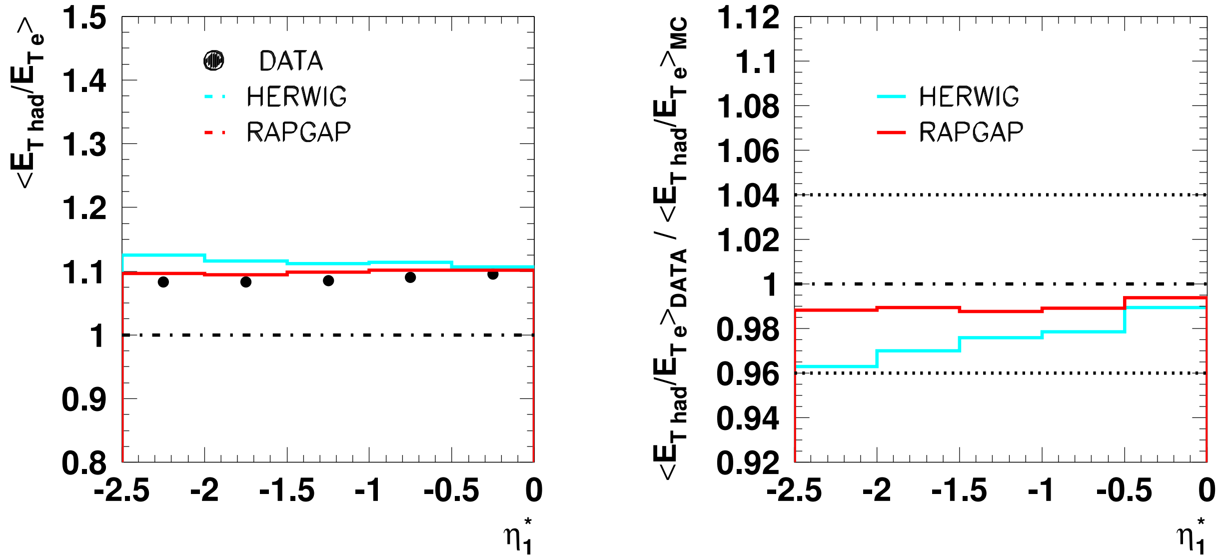

Figure 4.4: *Left plot:* Dependence of the mean values of $E_{T\,\mathrm{had}}/E_{T\,e}$ on the pseudorapidity of the leading jet, η_1^*. The mean values were obtained from the distributions in Fig. 4.3. *Right plot:* The double ratio $\langle E_{T\,\mathrm{had}}/E_{T\,e}\rangle_{\mathrm{DATA}}/\langle E_{T\,\mathrm{had}}/E_{T\,e}\rangle_{\mathrm{MC}}$.

with the data, while HERWIG is systematically slightly above them. In order to estimate the precision of the hadronic energy scale measurement, we construct the double ratio $\langle E_{T\,\mathrm{had}}/E_{T\,e}\rangle_{\mathrm{DATA}}/\langle E_{T\,\mathrm{had}}/E_{T\,e}\rangle_{\mathrm{MC}}$ (see the left part of Fig. 4.4). Its deviation from unity determines the uncertainty on the hadronic final state calibration, which we set on the basis of Fig. 4.4 to the value of 4%. Varying the overall hadronic energy scale of the LAr by $\pm 4\%$ then leads to systematic shift of the results, presented in Chapter 6, by typically 10%.

The energy calibration in the hadronic part of the SPACAL is known with the precision of 7% [Gla98, Poe00], which leads to a 2% systematic uncertainty of the final results.

4.3 Stability of the Event Yield

Once the calorimeter calibration is done, we can check the stability of the event yield, i.e. the dependence of the event rate per some period of integrated luminosity on time. This is shown in the upper part of Fig. 4.5. The event yield is quite stable in time, however, a small systematic drop in the second half of the 1999 running period is clearly visible. We also present the stability of the ratio of selected over generated events for the Monte Carlo simulation (HERWIG) in the lower part of Fig. 4.5. There we observe a similar decrease of rate of events passing the selection criteria as in the event yield of the data, indicating that the drop is probably caused by some change of detector performance, which is correctly taken into account by the simulation program of the H1 detector.

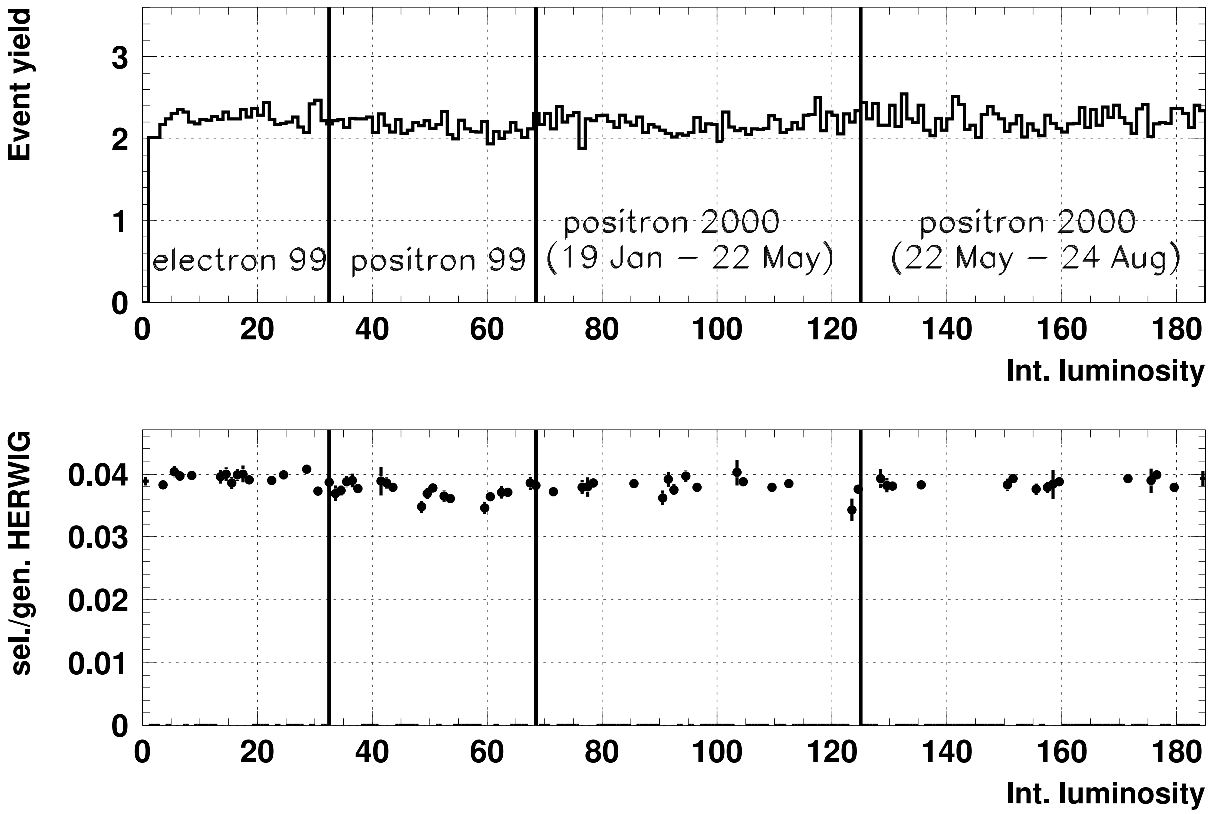

Figure 4.5: *Upper plot:* Stability of the event yield, i.e. the number of selected events per 1 pb^{-1}. One unit on the x-axis corresponds to the integrated luminosity of 300 pb^{-1}. *Lower plot:* Stability of the ratio of selected over generated events in HERWIG. The normalisation of both plots is different.

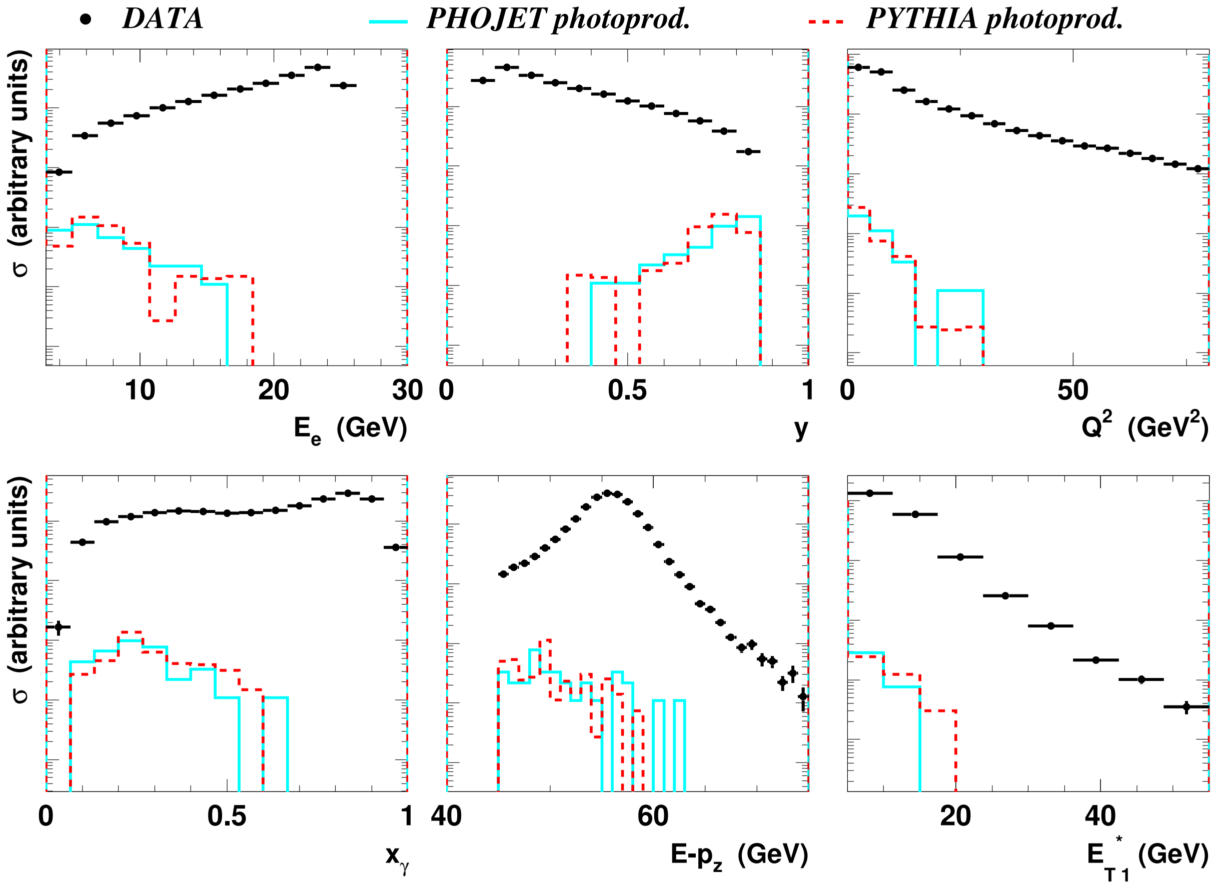

Figure 4.6: Comparison of different measured distributions (points) with the photoproduction background simulated by PHOJET (full line) and PYTHIA (dashed line).

4.4 Photoproduction Background

Photoproduction events, in which the scattered electron usually escapes undetected in the beam pipe, may contribute to our event sample if one of the hadronic final state particles is misidentified as the electron candidate. The corresponding background was estimated using MC programs PYTHIA [Sjo94] and PHOJET [Eng95, ER96]. This background is negligible for most of the phase space, as can be seen in Fig. 4.6. The largest contribution of photoproduction background is observed for the highest y, which corresponds to the region of low electron energies, where the electron identification is most difficult. In accord with the arguments given in Section 3.2.2, the photoproduction background is accumulated at low $E - p_z$.

The contribution of photoproduction events to our final triple differential cross sections is in general negligible, except for a few bins at high y, where it reaches up to 4%. The background, calculated as the average of the PYTHIA and PHOJET predictions, has been subtracted, and half of it is taken as the systematic uncertainty.

4.5 Corrections to the Data

The measurements and theoretical predictions must be compared under the same conditions. The standard praxis adopted by the H1 collaboration and others is to correct the measured data for the effects of limited detector acceptance and resolution (*detector effects*) and for the QED radiative corrections to the leptonic vertex of the interaction (*QED radiative effects*). The theoretical predictions of the *ep* collisions, on the other hand, have to end up with the "stable" final state particles, leptons and hadrons (the so-called *hadron level*). Therefore also in this Thesis, the data are confronted with the theory at the hadron level.

Schematically, the data can be corrected to the hadron level in the following way

$$\mathrm{DATA(hadr,\ nonrad)} = \mathrm{DATA(det,\ rad)}\ \frac{\mathrm{MC(hadr,\ nonrad)}}{\mathrm{MC(det,\ rad)}} \tag{4.1}$$

where terms "DATA" and "MC" stand for the measured or MC simulated distributions respectively, "det" and "hadr" denotes whether the distributions are at the detector or hadron level, and "rad" and "nonrad" whether they include QED radiation or not.

The proper correction procedure according to Eq. (4.1) requires to generate a large number of events with the QED radiation with the simulation of the full detector response. Unfortunately, since there was no suitable[2] LO MC model that simulates QED radiation in resolved photon interactions, the straightforward usage of Eq. (4.1) is not possible in our case. We employ a modified procedure instead:

$$\mathrm{DATA(hadr,\ nonrad)} = \mathrm{DATA(det,\ rad)}\ \frac{\mathrm{MC(hadr,\ nonrad)}}{\mathrm{MC(det,\ nonrad)}}\ \frac{\mathrm{MC(det,\ nonrad)}}{\mathrm{MC(det,\ rad)}} \tag{4.2}$$

where the first fraction stands for the correction of the detector effects and the second one for the QED radiation. In comparison with the approach schematically shown in Eq. (4.1), the two-step procedure introduced in Eq. (4.2) leads to somewhat (but not significantly) larger systematic uncertainty of the results and desires simulated samples of both QED radiative and nonradiative MC events. On the other hand, it enables us to separate radiative corrections from that of the detector effects. The former are smaller and, in the absence of a suitable resolved MC program, they can be roughly estimated using the direct photon interactions within the RAPGAP MC model. The latter are larger and we evaluate them using RAPGAP and HERWIG with both direct and resolved photon contributions.

[2] In principle, we could use MC program PYTHIA, which allows us to simulate QED processes in both direct and resolved photon interactions. However, due to a wrong parameter setting, we were not able to obtain realistic cross sections with PYTHIA at the time when large time-consuming simulations of the detector response have been submitted to computer processing. Only recently, the parameter setting has been corrected and since then PYTHIA predicts cross sections numerically similar to the data or other MC generators (HERWIG and RAPGAP), even though it is still far from being perfect, as will be demonstrated in Section 6.2.

4.5.1 QED Radiative Correction

Two samples of 700 000 RAPGAP direct photon events with and without the QED radiation, respectively, were passed to the full detector simulation. The basic quantities like Q^2, y, x_γ, $E^*_{T\,1}$, $E^*_{T\,2}$, η^*_1 and η^*_2 for both samples are shown in Figs. 4.7 and 4.8. The differences between them are roughly up to 7% (the largest for low y, high x_γ and low jet pseudorapidities).

The QED radiative effects are corrected for by reweighting functions dependent on the above mentioned seven quantities. The reweighting functions are fitted to the relative difference of RAPGAP with and without the QED radiation, as shown in right columns of Figs. 4.7 and 4.8. The final correction factors applied to data on event-by-event basis are given by product of all correction functions (see Appendix B for details of the reweighting).

To see the effect of this procedure, the reweighting has been applied to events generated with the non-radiative RAPGAP, and compared to the radiative RAPGAP sample. As demonstrated by Figs. 4.7 and 4.8, the relative differences between these two samples are then typically of the order of 2%, which is taken as the estimate of remaining systematic uncertainty arising from the QED radiative effects.

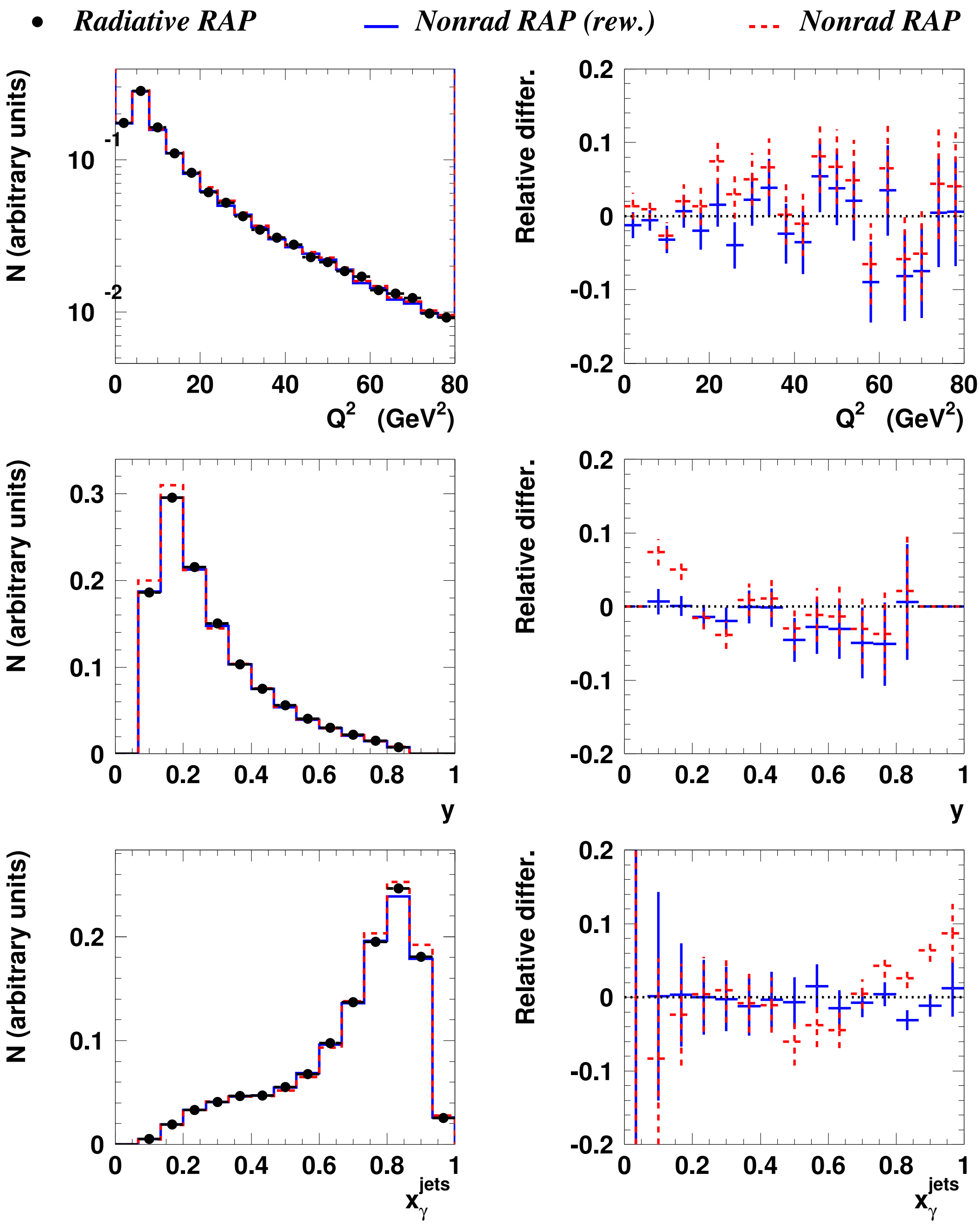

Figure 4.7: The comparison of direct photon events simulated by RAPGAP with the QED radiative correction (points), without it (red line) and without the radiation but corrected for it by the reweighting procedure described in text (blue line).

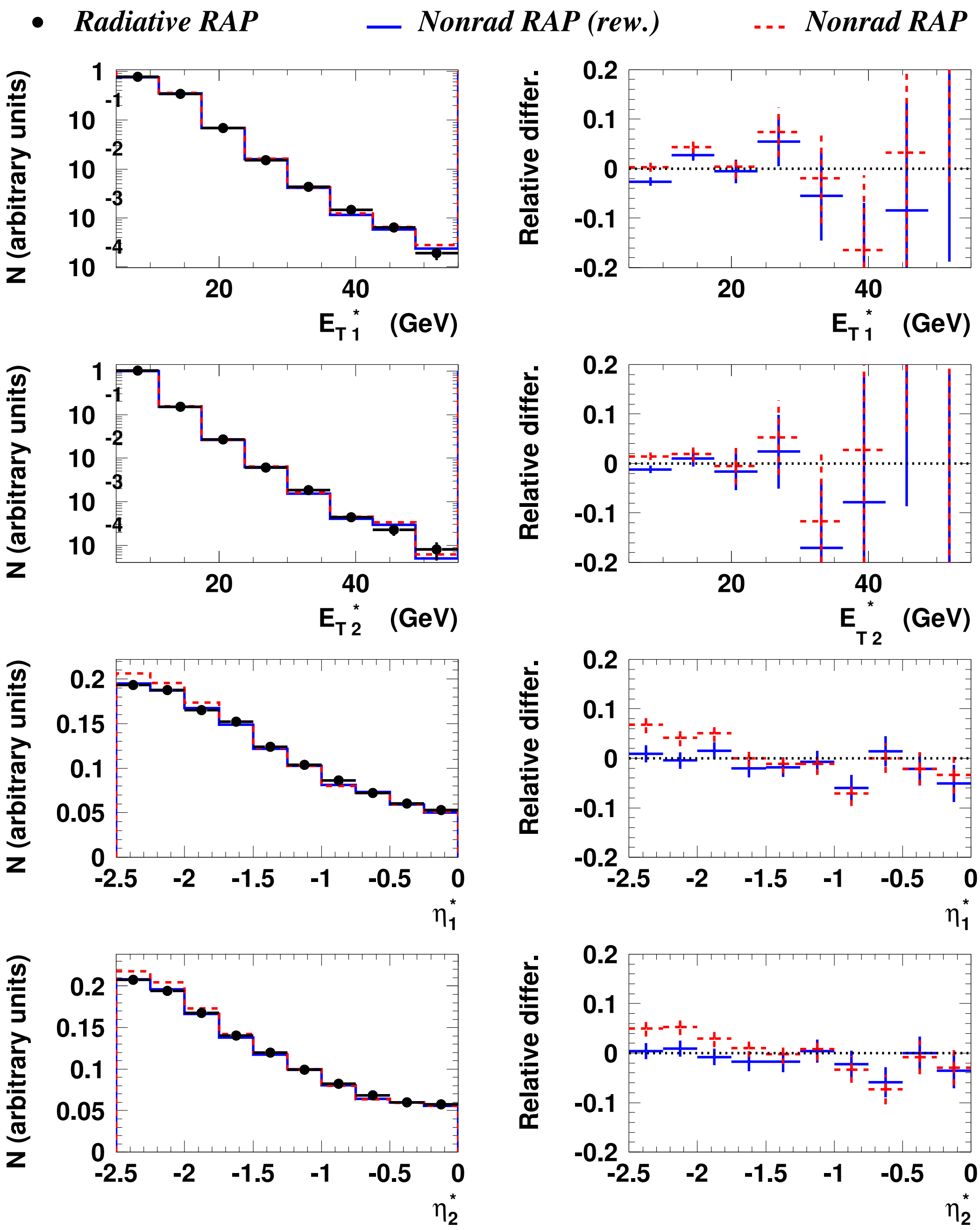

Figure 4.8: See the caption of Fig. 4.7.

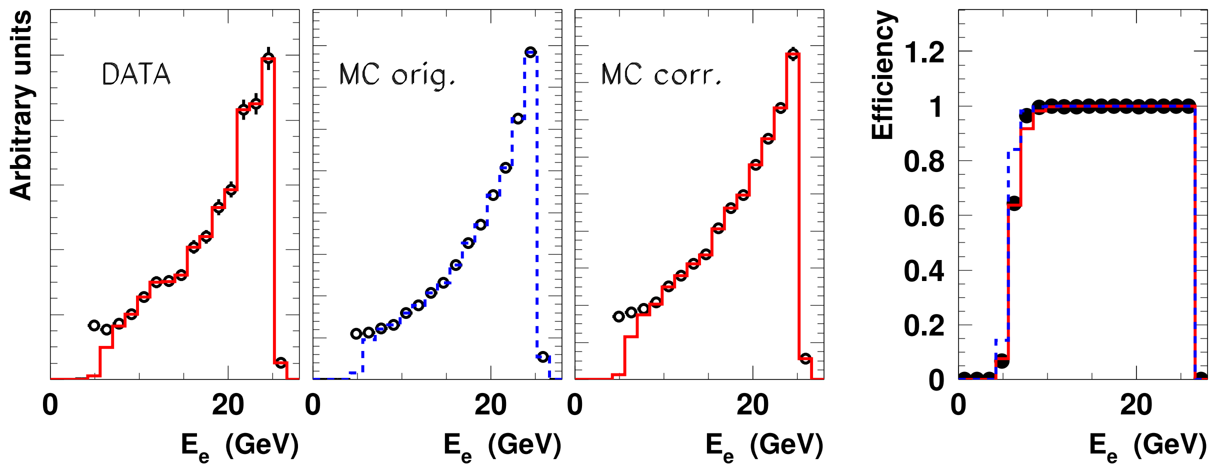

Figure 4.9: Study of the efficiency of the trigger element `SPCLe_IET>2` & `SPCL_R30`. Three plots on the left show number of events taken by a reference trigger (open circles) and by the reference trigger in coincidence with the studied trigger element (lines). The ratio of these two distributions defines the trigger element efficiency, and it is shown in the right plot separately for data (full circles), default MC simulation (dashed line) and corrected MC simulation (full line). See the text for further details.

4.5.2 Trigger Efficiency

Since only the events validated by one of the triggers *s9, s61* or *s64* (see page 36) are considered in the analysis, we have to check the efficiency of these triggers and apply some appropriate corrections if necessary.

Triggers in the H1 experiment are implemented into the simulation program H1SIM. It is therefore possible to correct for the trigger inefficiencies in one go together with the correction for the detector effects, which is the subject of the next section. However before we do so, we have to check that the trigger simulation is done properly and the efficiencies in MC are the same as that in the real data.

For this reason, we have studied efficiencies of all major trigger elements contained in the definitions[3] of *s9, s61* or *s64*. One of them, namely the trigger condition `SPCLe_IET>2` validated by L2 condition `SPCL_R30`, is exemplified in Fig. 4.9.

The efficiency is studied on a subsample of events selected by an independent trigger. If we, for example, investigate the efficiency of the SPACAL trigger elements, a LAr trigger is used to define the unbiased subsample of events.

Then we choose a variable characterising the given trigger element. In our example of `SPCLe_IET>2`, which fires if energy deposited in the SPACAL slicing window exceeds 5.7 GeV (see Appendix A), the electron energy acts as the characteristic variable. There-

[3]See Appendix A for the definitions of triggers and trigger elements.

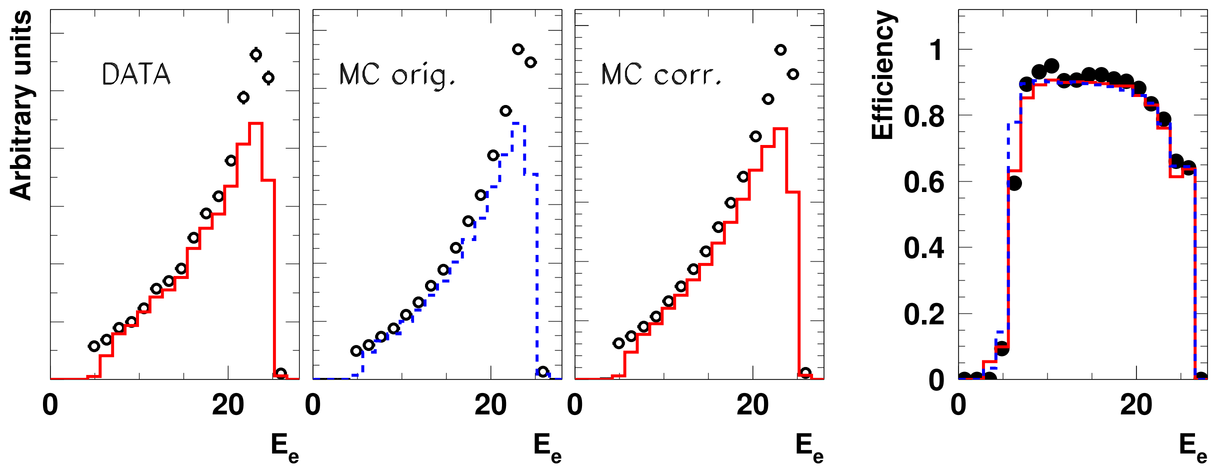

Figure 4.10: Example of the trigger efficiency for *s61*. See the caption of Fig. 4.9 for further details.

fore the efficiency of this trigger element is plotted as a function of the electron energy on the right-hand side of Fig. 4.9. By comparing the efficiency in the data (full circles) and default MC simulation (dashed line), we can see that the threshold behaviour around $E_e = 5.7\,\text{GeV}$ is not reproduced satisfactorily. The threshold in MC is shifted to lower values of E_e with respect to the threshold in the data.

In order to obtain the same trigger efficiency for the MC simulation as for the data, the trigger elements are reset at random in a small fraction of MC events. The fraction of MC events to be reset is determined from the ratio of trigger element efficiencies in the data and MC simulation. After this procedure, the efficiency in the MC simulation and data is the same, as indicated in the right part of Fig. 4.9 by the full line and full circles.

The correction had to be done for the trigger elements `SPCLe_IET>2`, `LAr_IF>1`, `LAr_Etrans>2` and `zVtx_mul<7`. This leads to the consequent improvement in the description of the trigger efficiencies of *s9, s61* and *s64* in MC simulation, as exemplified in Fig. 4.10. Remaining differences in the description of the trigger efficiencies are typically bellow 3%, and this number is therefore taken as the systematic uncertainty of the measured cross sections.

4.5.3 Detector Effects Correction

The correction of the measurement for the detector effects, corresponding to the first fraction in the right-hand side of Eq. (4.2), is done using the Bayesian unfolding technique [D'A95b]. For this purpose, the full detector response of 4+4 million events of HERWIG and RAPGAP samples were simulated and passed to the same reconstruction and analysis chain as for the data.

The main advantage of the Bayesian unfolding compared to the widely used bin-by-bin correction method[4] is a better treatment of migrations between (not only) neighbouring bins of measured distributions, if MC simulations do not perfectly describe the measured quantities.

In an ideal case, Bayesian technique should unfold the data correctly even if the simulated MC sample does not follow the measured distributions, provided the detector response is simulated realistically, and all possible classes of physics events are represented in the simulated event sample. In other words, the MC generator could be based on a toy model with only a limited physics input, and still the Bayesian procedure should perfectly correct for the detector effects and acceptance. In praxis, however, due to a limited statistics of the simulated MC samples and a limited number of variables in which the unfolding is performed, the results of the procedure may not be perfect. Therefore, we demand a good description of the data by the MC simulation at the detector level. This is realised by reweighting of simulated events, as described in Appendix B. At the end of the procedure, we have to check the dependence of the unfolded results on the reweighting (and we shall see that it is small).

The description of the data by reweighted HERWIG and RAPGAP is very good, as can be seen in Figs. 4.11 and 4.12. This is true for all basic distributions. We do not observe any significant difference between the description by HERWIG or RAPGAP, therefore we use both of them in the unfolding procedure.

The Bayesian unfolding, based on the Bayes' theorem, is described in detail elsewhere [D'A95b], therefore we only mention its main principles. The method is based on the so-called *smearing matrix*, which describes the probabilities of migrations from bins of the distributions at the detector level to the bins at the hadron level. The binning at detector level does not have to be the same as the one at the hadron level (contrary to the bin-by-bin method), and indeed, it is recommended to select fine binning at the detector level, while the bin size at the hadron level is more or less dictated by the resolution of the given quantity. The procedure requires an initial distribution, which serves as a "zeroth" guess of the unfolded distribution. The initial distribution can be flat, if we have no prejudice on how the results should look like, or other, if we have some theoretically motivated prediction for the results. The better[5] is the initial distribution, the more precise result of the unfolding can be expected. The non-optimal choice (knowledge) of the initial distribution can be overcome by an iterative procedure, in which the result of the unfolding is used as a new initial distribution, and the whole procedure is repeated again. This is somewhat against the spirit of the Bayes' theorem, since the same data are used several times for the same inference, however, this technique can be considered just

[4]The bin-by-bin correction method is based on a *generalised efficiency*, which may even be larger than unity, evaluated from MC simulation as the ratio of the number of events falling in a certain bin of a variable reconstructed at the hadron level and the number of events in the same bin reconstructed at the detector level. This efficiency, applied as a multiplicative factor on the measured distributions at the detector level, provides an estimate of the "true" number of events at the hadron level.

[5]Meaning "the closer to the unknown true distribution".

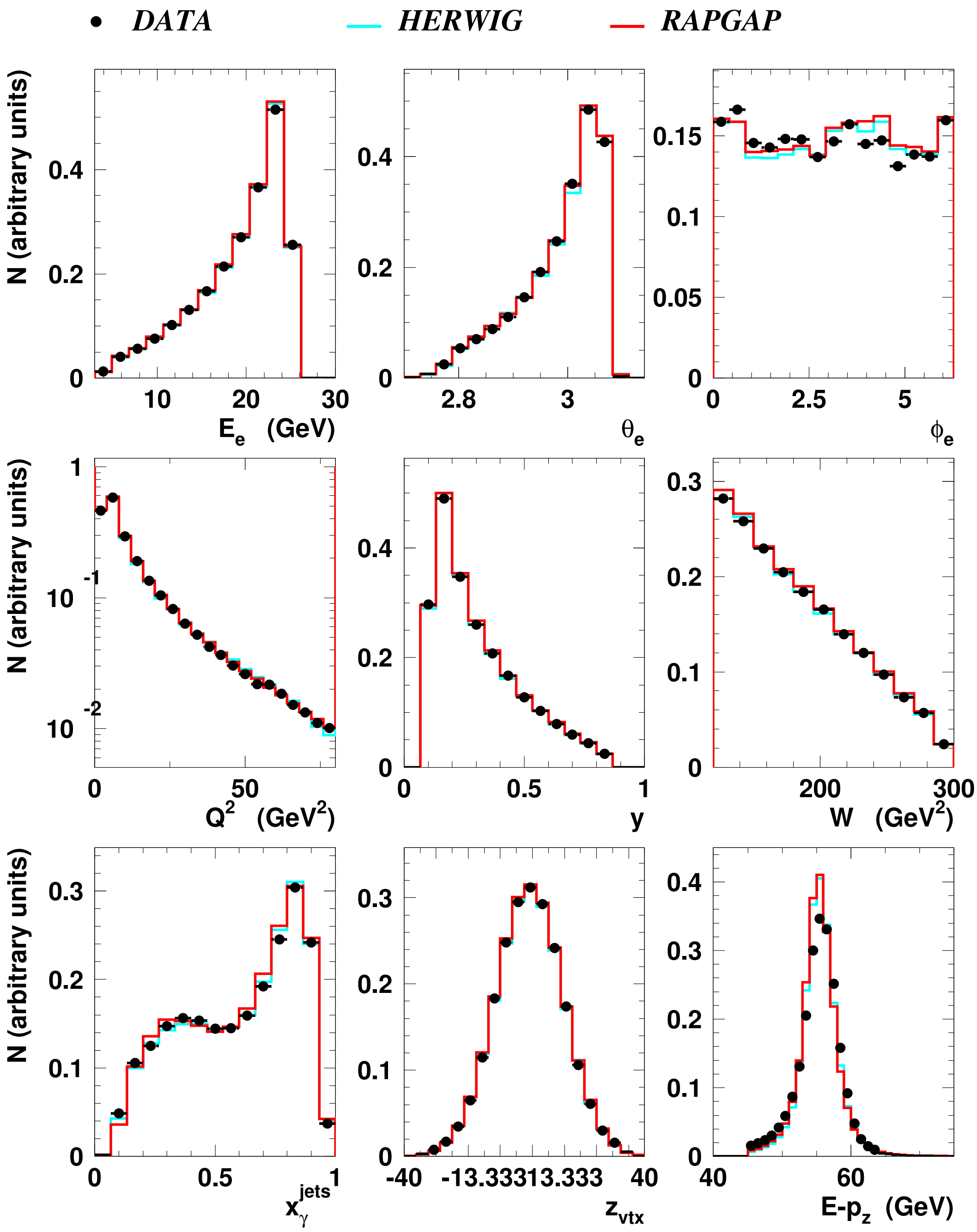

Figure 4.11: Control distributions of the most important observables. The data (points) are corrected for the QED radiation but not for the detector effects, and can thus be directly compared to MC simulations performed with HERWIG and RAPGAP simulated at the detector level.

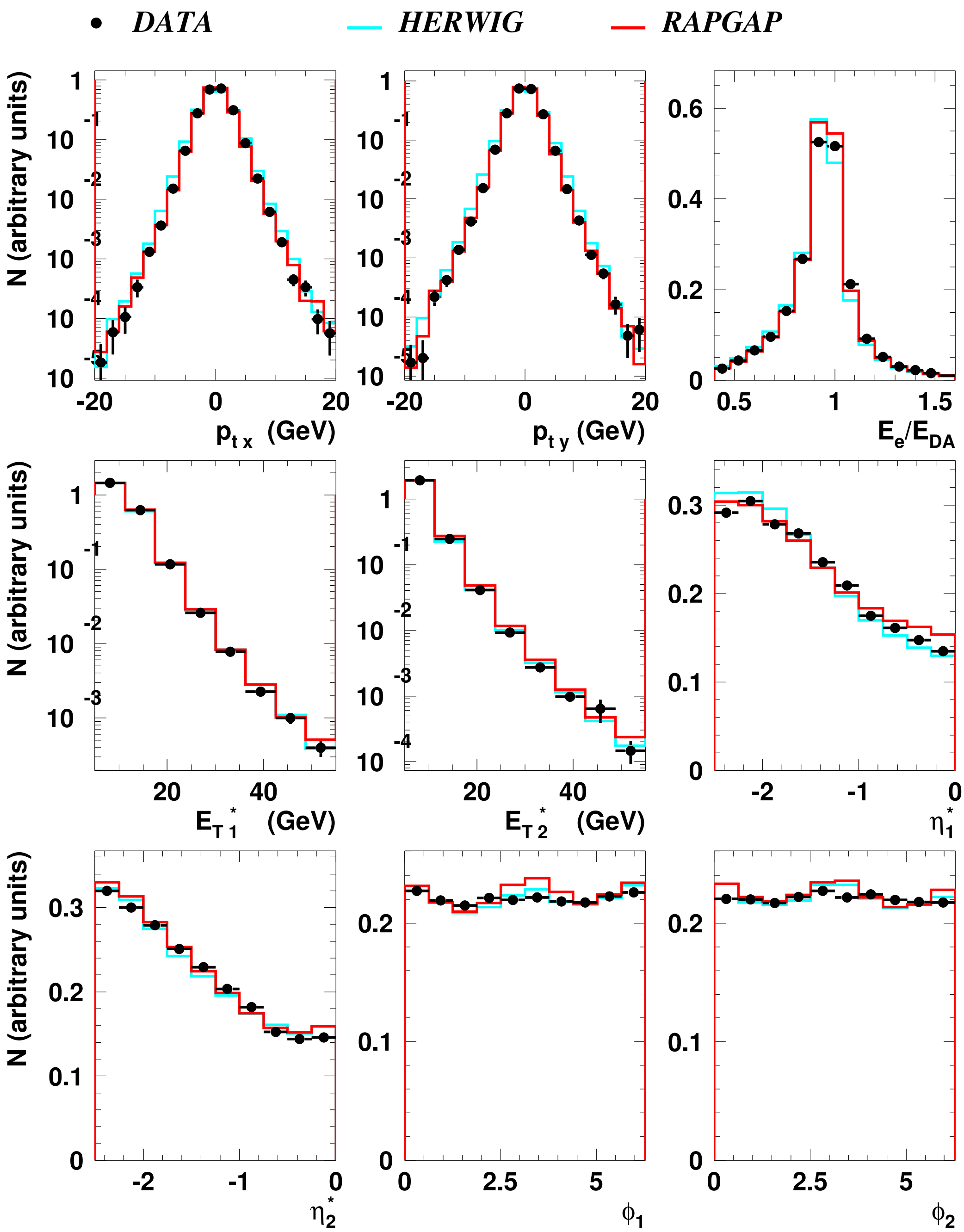

Figure 4.12: See the caption of Fig. 4.11. The variables $p_{t\,x}$ and $p_{t\,y}$ denote sum of transverse energies of all particles in the final state projected to the direction parallel or perpendicular to the direction of the scattered electron, respectively.

as a practical trick to increase the importance of the experimental data with respect to our theoretical prejudice [D'A95a]. On the other hand, the number of iterations should be as small as possible in order to minimise influence of statistical fluctuations in both measurement and MC simulation.

Our final results, the dijet cross sections, will be presented triple differentially, and for this reason also the unfolding is done in three dimensions. As we have theoretical predictions for the results, namely the cross sections from MC programs, we use them as the initial distributions.

The data are unfolded using both HERWIG and RAPGAP event samples independently. Different iterations of the unfolding for the cross section $\mathrm{d}^3\sigma_{2\mathrm{jet}}/\mathrm{d}Q^2\mathrm{d}E_T^*\,\mathrm{d}x_\gamma^{\mathrm{jets}}$ are exemplified in Fig. 4.13. The procedure converges very fast in most bins.

We have chosen the second iteration to be the final one. This decision is motivated by the test of the unfolding, in which several small[6] samples of HERWIG have been unfolded by the full event sample of RAPGAP, and vice versa. For each iteration, we calculated the quantity χ_n^2 defined as:

$$\chi_n^2 = \sum_{\mathrm{i}} \frac{(x_n^{(i)} - x_{\mathrm{true}}^{(i)})^2}{x_n^{(i)} + x_{\mathrm{true}}^{(i)}}, \tag{4.3}$$

where the sum runs over all bins of the unfolded distribution, $x_n^{(i)}$ is the value observed in the i-th bin after the n-th iteration of the unfolding procedure, and $x_{\mathrm{true}}^{(i)}$ stands for the "true" value (i.e. generated by HERWIG at the hadron level) in the i-th bin. The smaller is the quantity χ_n^2, the closer is the unfolded distribution to the true one. We therefore identify the iteration with the lowest χ_n^2 as the optimal one. We performed this procedure repetitively for all triple differential cross sections specified in Chapter 6, and identified the best iteration to be the first, second or the third one in majority of the trials. We take the second iterations as our central results. This is also in a good accord with the request of the smallest possible number of iterations mentioned earlier in this section. Half of the difference between the first and third iterations is taken as the systematic uncertainty due to the unfolding instability. Its size is typically less than 2% and at most 5%.

The main criterion for the reliability of the unfolding is the size of correlation between the neighbouring bins of the unfolded distribution, the so-called *off-diagonal elements of the covariant matrix* (see [D'A95b] for more details). The binning of the final cross section has been chosen such that the off-diagonal elements are always below 60%.

In all distributions studied, the final cross sections are taken as averages of the cross sections obtained when correcting for the detector effects using HERWIG and RAPGAP, since the description from the two models of the uncorrected distributions are of the similar quality. Half of the difference between the results unfolded with RAPGAP and HERWIG is taken as the systematic error due to the model dependence of the detector corrections. This leads to an error of 5–10% on average, reaching 20% in the most extreme case.

[6] Here the term "small" means "approximately of the same statistics as that in the measured data".

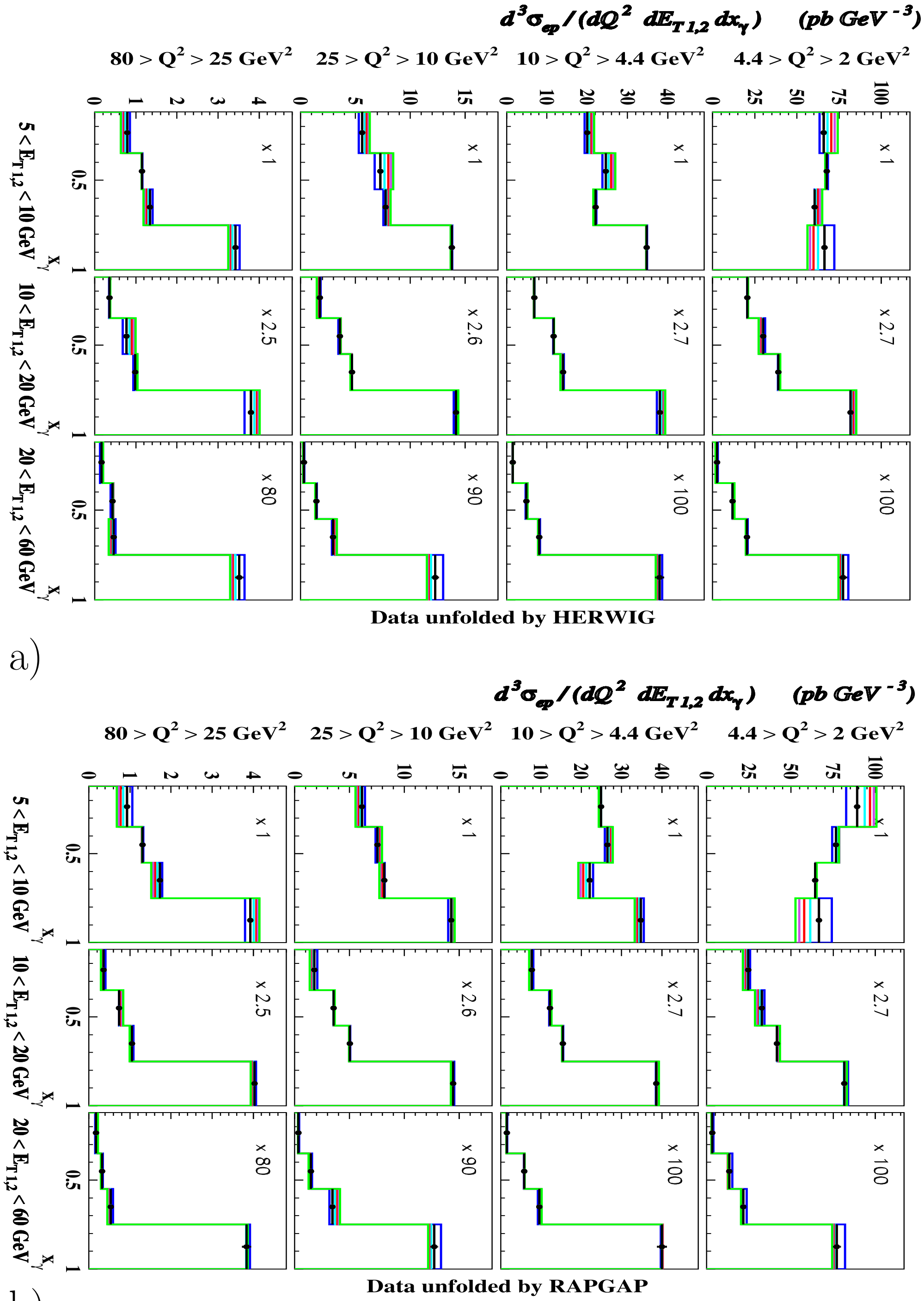

Figure 4.13: Different iterations of the unfolding procedure for $\mathrm{d}^3\sigma_{2\mathrm{jet}}/\mathrm{d}Q^2\mathrm{d}E_T^*\,\mathrm{d}x_\gamma^{\mathrm{jets}}$ using HERWIG *(a)* and RAPGAP *(b)*.

Chapter 5

Generator Studies

5.1 Comparison of the DISENT and JETVIP Predictions

As will be shown in Section 6.1.1, we observe non-negligible differences between the differential dijet cross section calculated using the NLO programs DISENT and JETVIP (only the direct photon contribution). We have checked that the discrepancy is not caused by the different setting of the input parameters or kinematic cuts, as the leading order $\mathcal{O}(\alpha\alpha_s)$ contributions agree perfectly.

The recent paper [DHKW99] compares predictions of dijet cross section calculated by four different NLO programs: DISENT, JETVIP, DISASTER++ and MEPJET. The differences between the cross sections predicted by the four NLO programs are found to be very small (within 3%) except for MEPJET, which deviates systematically from the other programs by typically 5-8%. The comparisons were done for different kinematic regions, some of them being very similar to that selected in this Thesis. However, only the total dijet cross sections have been investigated.

We have therefore also calculated the total dijet cross section in our kinematic region and found the agreement between DISENT and JETVIP on the level of 2%. Even the dijet cross sections plotted double differentially in the "electron variables" Q^2 and y (see Fig. 5.1) using JETVIP agrees quite well with that obtained with DISENT. However, as soon as we start to present the cross section differentially in the jet variables like η^*, E_T^* or x_γ^{jets}, the systematic deviations between both programs increase up to 40% (!) in part of the phase space, as shown in Section 6.1.1 (e.g. in Fig. 6.1).

5.2 Hadronisation Corrections

LO MC event generators, like HERWIG, RAPGAP, LEPTO and others, supplement predictions of partonic cross section with phenomenological hadronisation models. They

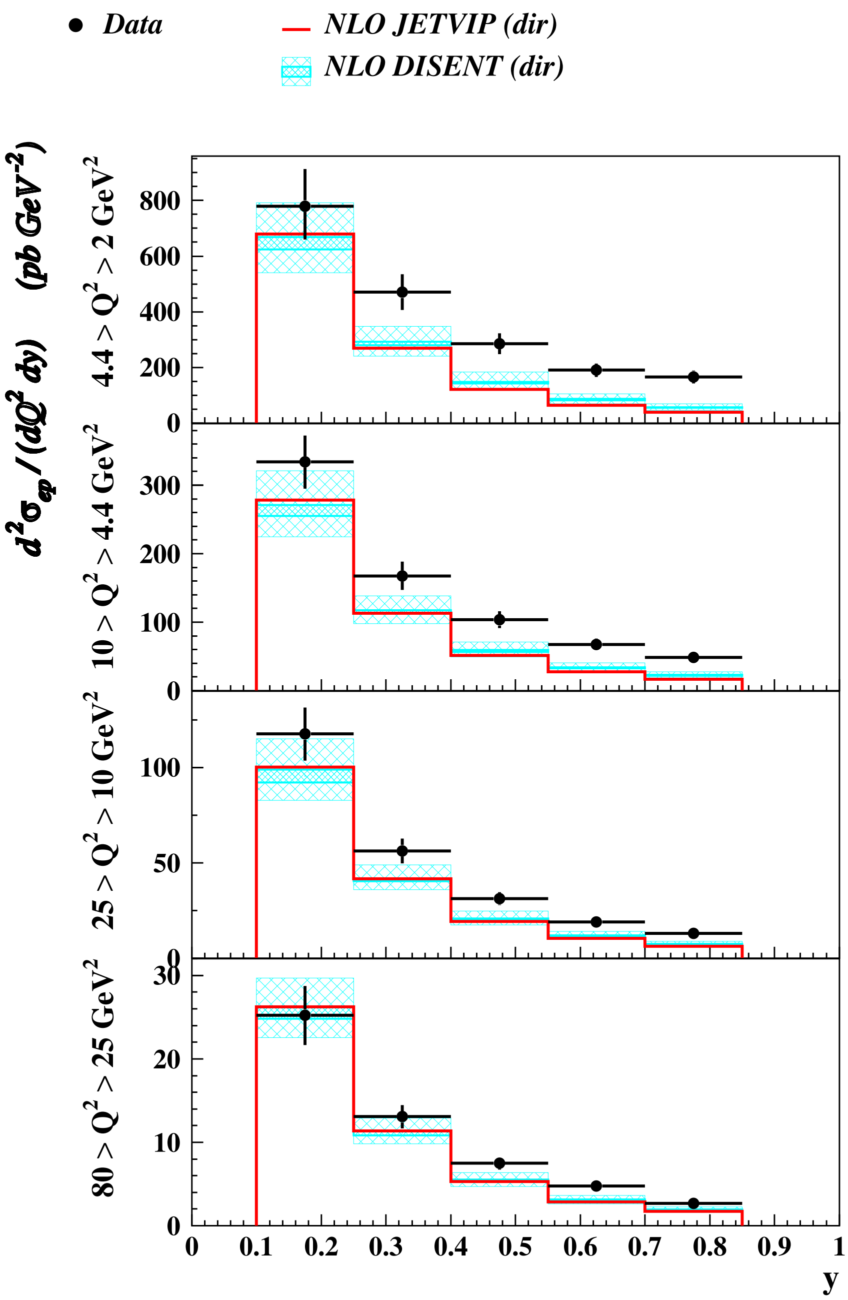

Figure 5.1: Double differential dijet cross section $\mathrm{d}^2\sigma_{\mathrm{ep}}/\mathrm{d}Q^2\mathrm{d}y$. The NLO QCD prediction calculated using DISENT (hatched area) is compared with the one calculated with JETVIP (full line). Both NLO predictions are corrected for hadronisation effects. The data points are shown in order to indicate the relative importance of the size of the difference between both programs. See the caption of Fig. 6.1 for further details.

thus predict cross sections at the hadron level, which can be directly compared with the measured data.

NLO calculations, like DISENT or JETVIP, so far do not include the simulation of the hadronisation, and predict only the parton level cross sections. Before they are compared with the experimental data, the size of the perturbatively uncalculable hadronisation corrections has to be estimated. There is, however, no unique way to separate perturbative and non-perturbative contributions in theoretical calculations, and the hadronisation corrections can be defined in different ways leading to different results.

In agreement with the usual praxis adopted in the H1 collaboration, we define the hadronisation corrections as

$$\mathcal{C}_{\mathrm{hadr.\,corr.}} = \frac{\mathrm{MC(parton\ level)}}{\mathrm{MC(hadron\ level)}} \,, \tag{5.1}$$

where the term "MC(parton level)" stands for the cross section predicted with a LO MC event generator at the parton level **after simulation of the initial and final state QCD parton showers**, while the term "MC(hadron level)" denotes the cross section predicted with the same MC generator at the hadron level. In addition to the simulation of hadronisation, the hadron level distributions include also the soft underlying interactions (see the description of HERWIG in Section 1.8), if the generator enables to do so. The same phase-space cuts are applied at both parton and hadron levels.

It is therefore obvious that the size of the hadronisation corrections depends not only on the hadronisation model but also on the values of the cut-off parameters for the parton showering in a given MC generator.

We estimate the size of the hadronisation corrections using two different MC models, HERWIG and LEPTO, and exemplify them in Fig. 5.2. The average values of the corrections obtained with the two models are applied to the NLO calculations as bin-by-bin correction factors and half the difference between the corrections obtained with HERWIG and LEPTO is taken as a hadronisation uncertainty in the NLO predictions. The hadronisation effects usually do not change the NLO predictions by more than 5%, with the exception of the cross section differential in x_γ^{jets}, for which the corrections are significantly larger in a few bins (see Fig. 5.2 *a*).

It should be stressed that the definition of hadronisation corrections in Eq. (5.1) does not correct for the initial and final state QCD parton showers, as they are included in both numerator and denominator of the expression (5.1). The parton level predictions in LO MC event generators appearing in the numerator of Eq. 5.1 include usually several (~ 10) partons from the QCD showering process, while the NLO parton level calculations, to which the corrections are applied, include only two or three partons in the final state. The parton levels in LO and NLO programs are therefore not equivalent. As will be demonstrated in Section 6.2, the QCD parton showers in LO MC generators increase the parton level cross section by 30%, which is much higher number than the hadronisation corrections defined in Eq. (5.1). The size of hadronisation corrections should therefore be

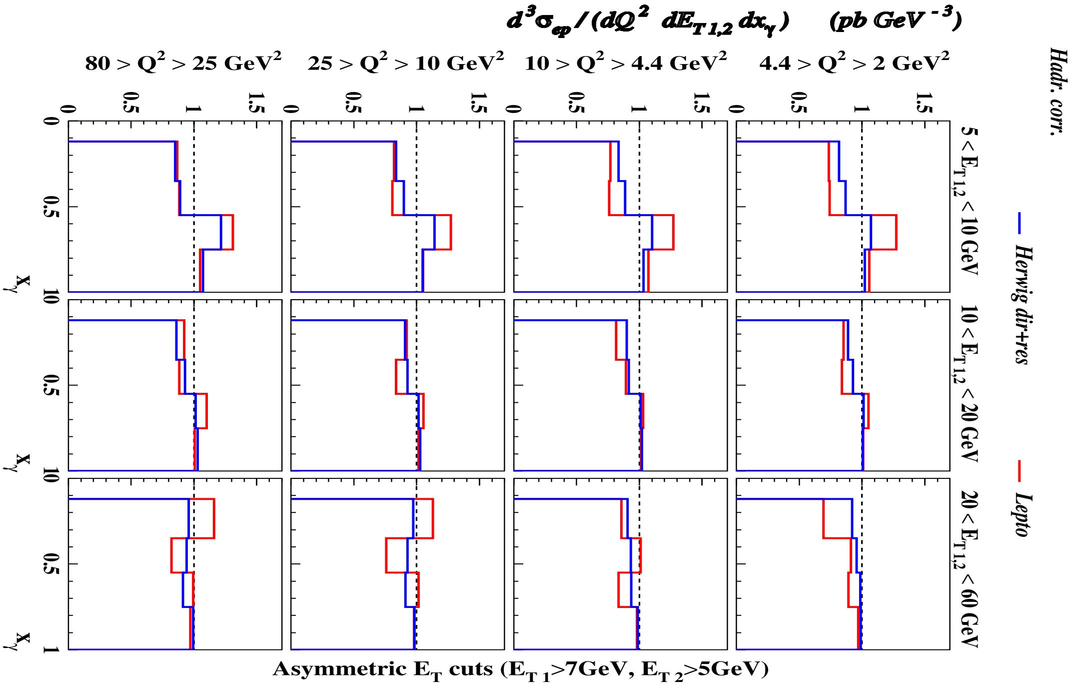

a)

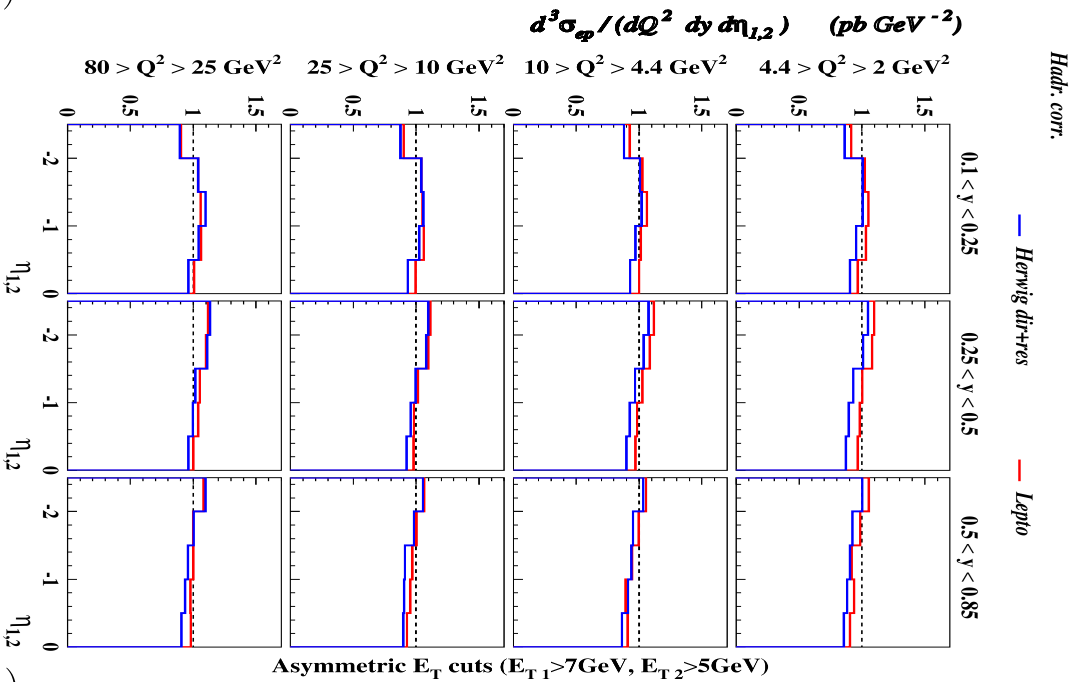

b)

Figure 5.2: Hadronisation corrections for the triple differential dijet cross section $\mathrm{d}^3\sigma_{2\mathrm{jet}}/\mathrm{d}Q^2\mathrm{d}E_T^*\,\mathrm{d}x_\gamma^{\mathrm{jets}}$ *(a)* and $\mathrm{d}^3\sigma_{2\mathrm{jet}}/\mathrm{d}Q^2\mathrm{d}y\mathrm{d}\eta^*$ *(b)*.

taken with caution. In the absence of a better unambiguous definition of hadronisation corrections we stay with the one adopted by the H1 collaboration.

5.3 Dependence of the JETVIP Predictions on $\mathbf{y_s}$ Parameter

The NLO program JETVIP uses the phase-space slicing method to cancel the collinear and infrared singularities between the real and virtual emissions. The method introduces a technical "slicing" parameter, y_s, which separates regions of phase space of the numerical calculation and approximative analytical cancellation of the cross section. However, the final prediction of JETVIP should be independent of y_s.

Numerically correct results can be obtained only for sufficiently small values of the y_s parameter. The author of JETVIP recommends to choose y_s in the interval $10^{-4} \leq y_s \leq 10^{-2}$ [Pot99] or $10^{-4} \leq y_s \leq 10^{-3}$ [Pot00]. He claims [Pot00] that *"it is very hard to calculate the cross section for values of $y_s < 10^{-5}$ since the compensation between large positive and negative contributions lead to large statistical errors, which is a well-known problem of the phase-space slicing method".* Nevertheless, except the problem with the statistics, no other argument has been given why the slicing method should not be applicable for $y_s < 10^{-5}$.

Due to an enormous increase of the computing power in the last few years, nowadays we were able to generate huge samples of 200 and 350 million events for resolved and direct photon interactions, respectively. Generating several different runs of the JETVIP predictions for the total dijet cross section in our kinematic region shows that the statistical fluctuations in the calculations do not cause any problems even for $y_s = 10^{-5}$. This is illustrated in Fig. 5.3, where different runs of JETVIP predict stable cross sections once the number of generated events exceeds 50 million.

Several authors of jet analyses (e.g. in [DHKW99]) claim that JETVIP calculations depend significantly on the value of y_s. We have therefore investigated the y_s dependence of the dijet cross section in our kinematic region, which is exemplified in Fig. 5.4. The NLO direct photon contribution in our kinematic region is independent of y_s to within 5% over the range of recommended interval $10^{-4} \leq y_s \leq 10^{-2}$, except for the highest E_T^* and Q^2 bin, where the cross section varies by 15%. The situation changes in the case of the NLO resolved photon contribution, for which the dependence on y_s is significantly larger. The sum of NLO direct and NLO resolved photon JETVIP predictions varies by 30% in some bins for the recommended range of y_s. We set $y_s = 0.003$ in all JETVIP calculations, since the predictions are most stable around this value.

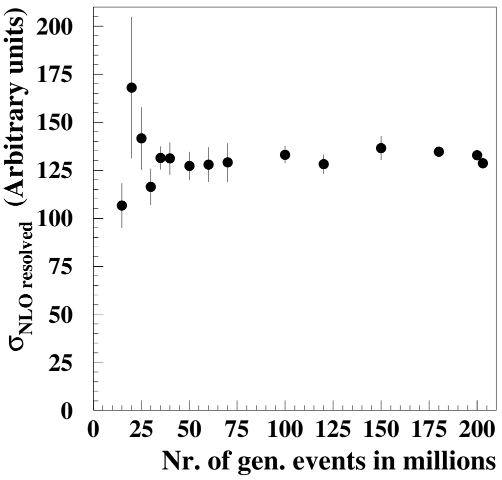

Figure 5.3: Dependence of the total dijet cross section, calculated in our kinematic region with NLO JETVIP, on the number of generated events. The parameter y_s is set to 10^{-5}. The error bands correspond to statistical uncertainties estimated by JETVIP.

5.4 Energy Flow around Jets

The proper description of the energy flow inside and outside jets is important for the correct procedure of the unfolding of the detector effects as well as for comparisons of the measurement with theoretical predictions. The energy flow is therefore presented in Fig. 5.5. The figure is produced in the following way: the transverse energies of combined objects, which are measured by the detector and roughly correspond to hadrons (see Section 3.2.1), are summed in the histogram according to $\Delta\phi$, which is the difference of their azimuthal angle and the azimuthal angle of the jet. Only the combined objects that are close to the jet in rapidity, $|\eta^*_{\text{jet}} - \eta^*_{\text{object}}| < 1$, are included. The procedure is done for the two hardest jets satisfying the selection criteria specified in Chapter 3.

The energy flow of hadrons deposited outside jets is often called *jet pedestal*. Figure 5.5 a demonstrates that the relative importance of the jet pedestals rises with decreasing E_T^* of the jets. On the other hand, the dependence of the energy flow outside jets on Q^2 is only weak, if any. Figure 5.5 b indicates that the jet pedestals depend significantly on the pseudorapidity of the jets, η^*. While for small η^*, i.e. in the so-called *backward jet region*, the energy flow outside jets is relatively small, it increases for large η^*, i.e. in the *forward jet region*. This reflects the fact that the resolved photon processes, which produce jets predominantly in the forward region, provide less energy for the hard subprocess and therefore more energy for a possible additional soft interactions than the

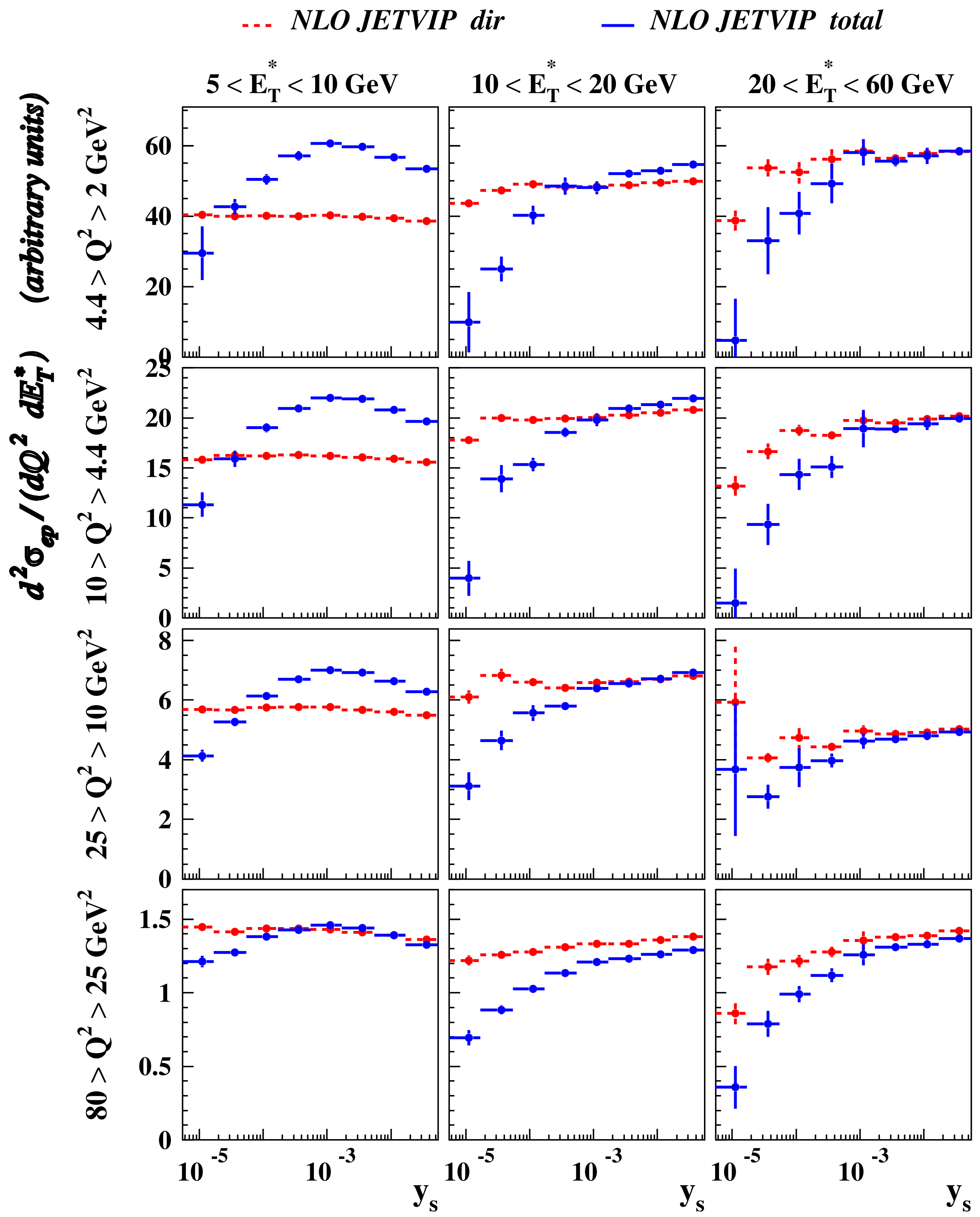

Figure 5.4: Dependence of the JETVIP cross sections, calculated at NLO in different Q^2 and E_T^* regions, on the y_s parameter.

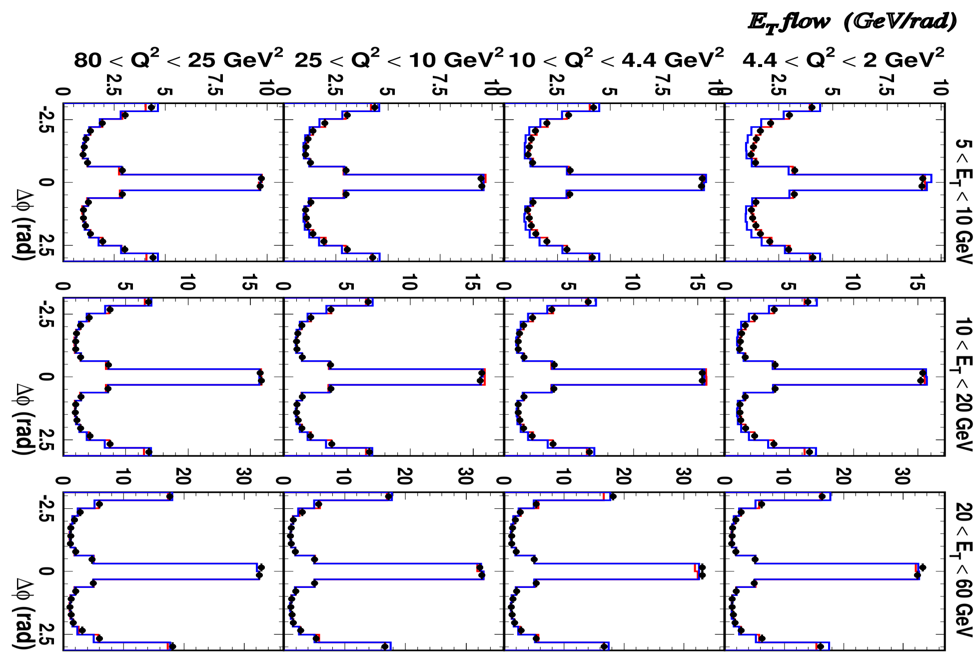

a)

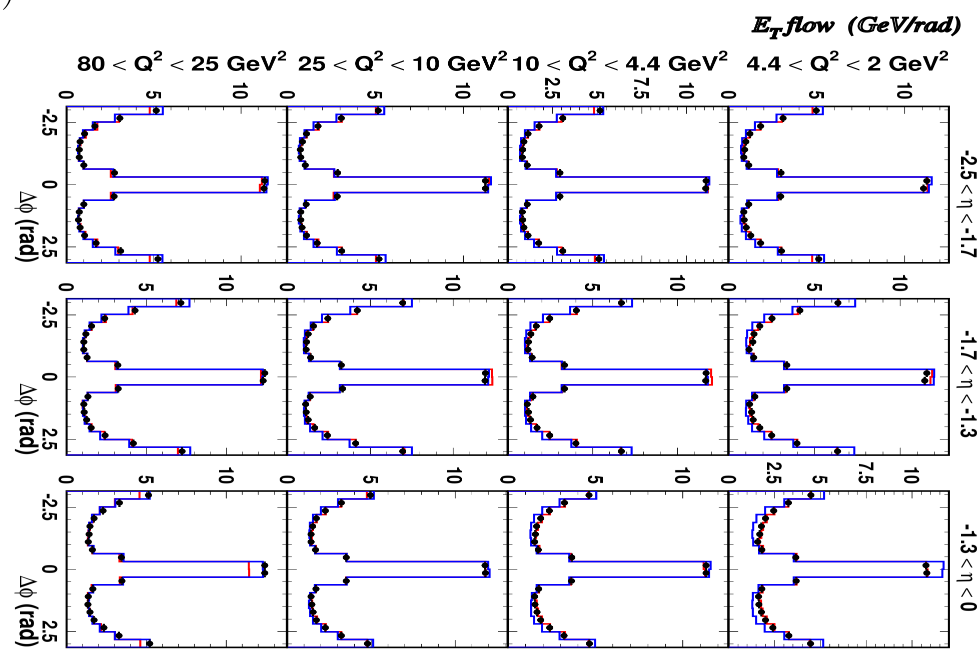

b)

Figure 5.5: The energy flow around the jet axis in different regions of Q^2 and E_T^* *(a)* and in different regions of Q^2 and η^* *(b)*.

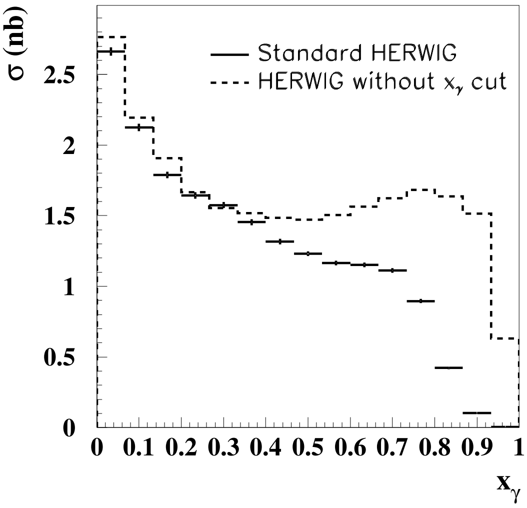

Figure 5.6: Comparison of the resolved photon dijet cross section computed by the standard HERWIG with the "x_γ cut" (full line) and the modified HERWIG in which high x_γ values in the photon PDF are not cut out (dashed line). The calculations are performed in the kinematic region $1 < Q^2 < 100\,\mathrm{GeV}^2$, $0.05 < y < 0.95$ and $p_T^{\min} = 3\,\mathrm{GeV}$, where $p_T^{\min}$ denotes the minimum transverse momentum of the outgoing parton. No cut on jet pseudorapidities has been applied.

direct processes producing jets predominantly at low η^*.

5.5 Cut on High $\mathbf{x}_\gamma$ in HERWIG

MC program HERWIG employs on-shell matrix elements but takes into account finite masses of the quarks, which introduces rather tricky treatment of some mass-related effects. One of them is a cut on the photon PDF in the high x_γ region in the resolved photon processes. Events with $x_\gamma^{\mathrm{gen}} > (1 - f(m_q)/\mu)$ (where x_γ^{gen} denotes x_γ generated at the parton level, μ is the hard scale and $f(m_q)$ is a function of quark and gluon masses[1]) are cut away as if they were not present in the appropriate photon PDF. This cut is not done in other MC generators, neither in the NLO programs like JETVIP. Moreover, it is inconsistent with the usual way of the extraction of photon PDFs from experimental data, which is based on analytical formulae without the x_γ^{gen} cut. Consequently, there is quite a big difference in the x_γ^{jets} spectrum in resolved photon processes for $x_\gamma^{\mathrm{jets}} \gtrsim 0.75$ between the HERWIG and other MC generators. Figure 5.6 illustrates the influence of the x_γ cut in HERWIG. However, the standard HERWIG with the x_γ cut is used throughout the Thesis.

[1] $f(m_q) \sim 0.8 - 0.85\,\mathrm{GeV}$. The precise definition is: $f = (m_q + 0.48)\,\mathrm{GeV}$ for quarks, and $f = (m_G + 0.10)\,\mathrm{GeV}$ for gluons, where HERWIG default parton masses are $m_q = 0.32\,\mathrm{GeV}$ and $m_G = 0.75\,\mathrm{GeV}$.

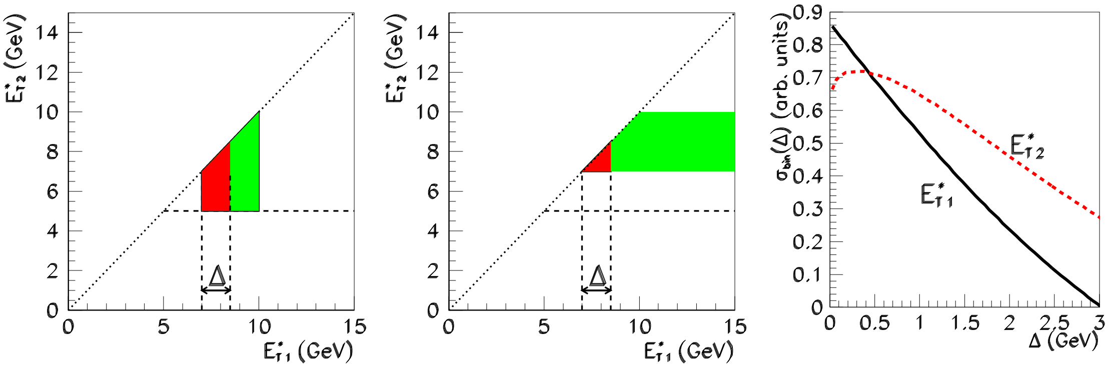

Figure 5.7: The left and middle plots show the phase space defined in Eq. (5.2) and (5.3), respectively. Also shown is the Δ cut, which decreases the phase space of the bin according to Eq. (5.4). The right figure shows the dijet cross section in the bin of Eq. (5.2) (full line) and (5.3) (dashed line) as function of Δ.

5.6 Asymmetric Cuts in the NLO Calculations

Due to experimental as well as theoretical reasons, some lower cut on the transverse energy of jets has to be applied in the analysis. In the NLO calculations of dijet cross section, this cut can, however, get into conflict with the infrared safety in parts of the phase space [KK96, KK97, FR97, CS03]. The problems in numerical calculations come from the region $E^*_{T\,1} \approx E^*_{T\,2}$, where the negative virtual corrections do not properly cancel with the positive real emissions. This leads to an unphysical behaviour of the NLO predictions, which is typically manifested by the increase of the cross section when reducing certain parts of the phase space. The situation is often solved by imposing an asymmetric cut on E^*_T of the jets. The same strategy has been adopted in this Thesis (see Section 3.2.1), even though it has been recently argued that the symmetric E^*_T cut scenario is equally suitable (or problematic) as the asymmetric one [CS03].

The total dijet cross section in our phase space is thus clearly infrared safe. However when plotting the cross section differentially, the situation is more complicated. Let us for example closely inspect the cross section $\mathrm{d}^3\sigma_{2\mathrm{jet}}/\mathrm{d}Q^2\mathrm{d}E^*_T\,\mathrm{d}x_\gamma^{\mathrm{jets}}$, which is one of our final results presented in Chapter 6. In this "inclusive dijet" cross section each event contributes to the distribution twice – separately for the first and for the second jets.

Let us select just one bin of the distribution, e.g. the one with[2] $7 < E^*_T < 10\,\mathrm{GeV}$ and arbitrary Q^2 and x_γ^{jets}. The selected bin is graphically presented in the left and middle charts of Fig. 5.7 and mathematically expressed as

$$7 \leq E^*_{T\,1} \leq 10\,\mathrm{GeV}, \qquad E^*_{T\,1} \geq E^*_{T\,2}\,, \qquad E^*_{T\,2} \geq 5\,\mathrm{GeV} \tag{5.2}$$

[2]The variable E^*_T denotes the transverse energies of the jets with the highest and second highest E_T measured in the photon-proton centre-of-mass frame.

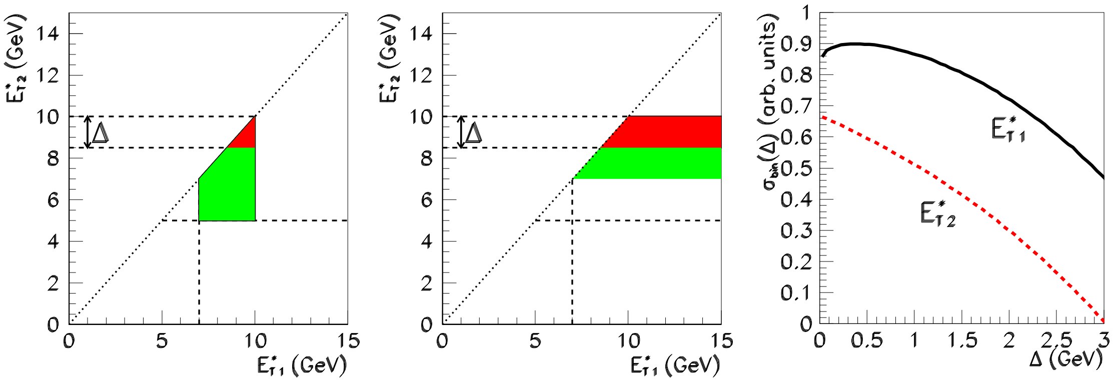

Figure 5.8: Analogous to Fig. 5.7 but for Δ cut defined in Eq. (5.5).

$$7 \leq E^*_{T\,2} \leq 10\,\mathrm{GeV}, \qquad E^*_{T\,1} \geq E^*_{T\,2}\ . \tag{5.3}$$

For both bins we can introduce an additional cut Δ, which chops off part of these bins, and investigate the dependence of the cross section on the parameter *Delta* in the limit $\Delta \to 0$. This dependence for Δ chosen in the following way

$$7 + \Delta \leq E^*_{T\,1} \leq 10\,\mathrm{GeV} \tag{5.4}$$

is shown in the right-hand part of Fig. 5.7. The dijet cross section in the bin defined by Eq. 5.3 behaves unphysically for small Δ, since it increases with decreasing phase space. This observation is in accord with unphysical behaviour of dijet cross section with symmetric E_T cut scenaria previously reported in several publications. One could therefore conclude that it is not safe to plot the distribution $d\sigma/dE^*_{T\,2}$.

However, one can introduce a Δ cut in an alternative way

$$7 \leq E^*_{T\,2} \leq 10 - \Delta\ \mathrm{GeV}\ , \tag{5.5}$$

graphically presented in Fig. 5.8, which is certainly as legitimate as the cut in Eq. 5.4. The corresponding cross sections, shown in the right part of Fig. 5.8, lead to opposite conclusion than the Δ cut in Eq. 5.4. Now $d\sigma/dE^*_{T\,2}$ is monotonously decreasing function of Δ, while $d\sigma/dE^*_{T\,1}$ behaves unphysically.

To conclude, there is no way how to introduce the cuts on transverse energies of the jets that would entirely avoid the problems of numerical NLO calculations described in this section. For any variable or binning there is always a simple way how to cut the chosen kinematic region in a way that leads to the unphysical behaviour of the cross section. More details about this issue can be found in [CS03].

The problematic kinematic region $E^*_{T\,1} \approx E^*_{T\,2} \approx 7\,\mathrm{GeV}$ in Fig. 5.7 is partially compensated by a complementary region $E^*_{T\,1} \approx E^*_{T\,2} \approx 10\,\mathrm{GeV}$ (and vice versa in Fig. 5.8). Also by merging the kinematic regions defined in Eq. 5.4 and 5.5 into one bin, which is done for the final dijet cross sections presented in Chapter 6, the unphysical dependence of the cross section on the Δ cuts is substantially decreased. In the absence of a better possibility, we stay with the predictions of present NLO programs based on numerical calculations using Monte Carlo technique.

Chapter 6

Results

In this chapter we present the main results of the measurement, namely the triple differential dijet cross sections, $\mathrm{d}^3\sigma_{2\mathrm{jet}}/\mathrm{d}Q^2\mathrm{d}E_T^*\,\mathrm{d}x_\gamma^{\mathrm{jets}}$, $\mathrm{d}^3\sigma_{2\mathrm{jet}}/\mathrm{d}Q^2\mathrm{d}y\mathrm{d}\eta^*$, $\mathrm{d}^3\sigma_{2\mathrm{jet}}/\mathrm{d}Q^2\mathrm{d}\eta^*\,\mathrm{d}E_T^*$ and triple differential event cross section $\mathrm{d}^3\sigma_{\mathrm{ep}}/\mathrm{d}Q^2\mathrm{d}x_\gamma^{\mathrm{jets}}\mathrm{d}y$, measured in the region of photon virtualities $2 < Q^2 < 80\,\mathrm{GeV}^2$, inelasticities $0.1 < y < 0.85$, transverse energy of the jets $E^*_{T\,1} > 7\,\mathrm{GeV}$, $E^*_{T\,2} > 5\,\mathrm{GeV}$ and pseudorapidities $-2.5 < \eta_1^*, \eta_2^* < 0$. By the term "dijet cross sections" we mean that both hardest and second hardest jets contribute to the distributions, i.e. each event is considered twice. Contrary to that, each event contributes only once to the distributions in the case of the "event cross section".

The results are presented below in form of figures, the numerical values of the cross sections are summarised in the tables of Appendix C.

6.1 Comparison with NLO Parton Level Calculations

6.1.1 NLO Direct Photon Contribution

In this section, the measured cross sections are compared with the NLO direct photon[1] calculations, which do not include the concept of resolved virtual photon, performed with DISENT and JETVIP.

The triple differential dijet cross section is presented as a function of x_γ^{jets} in different bins of Q^2 and E_T^* in Fig. 6.1. The variable E_T^* is used to denote the transverse energy of jets with the highest and second highest transverse energy measured in the photon-proton centre-of-mass frame, so that each event contributes twice to the distributions. The measured data are presented by points, the inner error bars show the statistical error, the outer error bars stand for the quadratic sum of systematic and statistical errors. The uncertainties of DISENT prediction coming from variation of the factorisation and renormalisation scales in the interval $E_T/2$ to $2E_T$ as well as from hadronisation corrections

[1]For brevity reasons, we will use term "direct calculations" and "direct contribution" instead of "direct photon calculations" and "direct photon contribution", respectively.

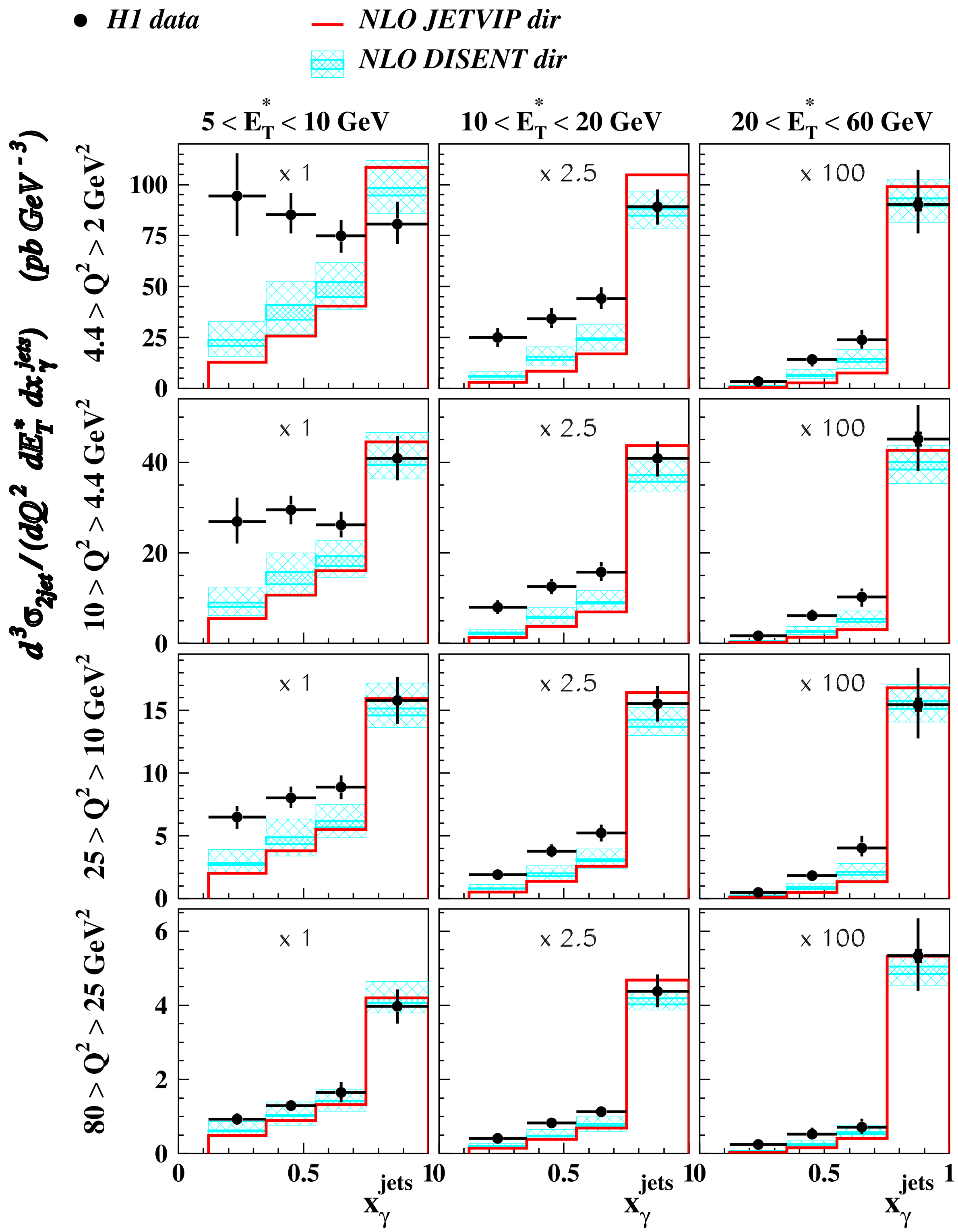

Figure 6.1: Triple differential dijet cross section $\mathrm{d}^3\sigma_{2\mathrm{jet}}/\mathrm{d}Q^2\mathrm{d}E_T^*\,\mathrm{d}x_\gamma^{\mathrm{jets}}$. The inner error bars on the data points show the statistical error, the outer error bars stand for the quadratic sum of systematic and statistical errors. Also shown are NLO calculations of DISENT (hatched area) and JETVIP (full line), both of them corrected for hadronisation effects. The inner hatched area denotes the uncertainty of the hadronisation corrections, the outer hatched area stands for the quadratic sum of the error from hadronisation and the scale uncertainty (shown only for DISENT). The scale factors applied to the cross sections are indicated.

are indicated. The uncertainties (not shown) of the direct contribution obtained with JETVIP are approximately the same as for DISENT.

Figure 6.1 demonstrates that the NLO direct calculations are able to describe the data in the region of high $x_\gamma^{\rm jets}$. For $x_\gamma^{\rm jets} < 0.75$, i.e. the region dominated by the resolved photon contribution, the description is never perfect, indicating the need for orders beyond the NLO. The description of the data for $x_\gamma^{\rm jets} < 0.75$ gets worse as Q^2 and E_T^* decrease and the resolved photon contribution in the data becomes dominant. The discrepancy is particularly pronounced in the lowest Q^2 and lowest E_T^* bin, where the data at low $x_\gamma^{\rm jets}$ lie significantly above the theoretical predictions, even taking into account the sizable scale uncertainty.

The relative decrease of the cross section at low $x_\gamma^{\rm jets}$ for high E_T^* is of kinematic origin. Due to the smaller energy available for the hard process[2], the production of high E_T^* jets is suppressed at small $x_\gamma^{\rm jets}$.

Note that for $x_\gamma^{\rm jets} < 0.75$ the JETVIP results are systematically lower than those of DISENT, whereas for $x_\gamma^{\rm jets} > 0.75$ it is the other way round. The discrepancy between DISENT and JETVIP is clearly observable only for multi-differential distributions which include a jet variable. It gets substantially smaller for the distributions in electron variables only, like y and Q^2, as can be seen from the inclusive dijet cross section $\mathrm{d}^2\sigma_{\rm ep}/\mathrm{d}Q^2\mathrm{d}y$ in Section 5.1 (see Fig. 5.1).

In Fig. 6.2 the event cross section is shown as a function of y in different bins of Q^2 and $x_\gamma^{\rm jets}$. As in the case of Fig. 6.1, we observe good agreement between the data and theoretical predictions in the region of $x_\gamma^{\rm jets} > 0.75$. The cross sections in low $x_\gamma^{\rm jets}$ region are not described properly, the disagreement rising with decreasing Q^2. Especially the high y, low $x_\gamma^{\rm jets}$ and low Q^2 region, where we expect the resolved photon processes to dominate, is poorly described – the data are more than four times higher than the NLO calculations. The difference can not be accommodated within the theoretical and experimental errors.

Instead of the variable $x_\gamma^{\rm jets}$, which has a clear and intuitive physics interpretation as the four-momentum fraction of the photon carried by a parton but is not directly measurable, the data were also analysed in terms of jet pseudorapidities. Figure 6.3 presents the dijet cross section as a function of η^* in different bins of Q^2 and y, where η^* denotes the pseudorapidities of the jets with the highest and second highest transverse energy. The excess of the data over the direct contribution at low $x_\gamma^{\rm jets}$ and low Q^2 observed in Figs. 6.1 and 6.2 is reflected in a similar excess at high y and low Q^2 in Fig. 6.3. The discrepancy is especially pronounced at large η^* (i.e. in the forward jet region).

Figure 6.4 shows the triple differential dijet cross section as a function of E_T^* in different bins of Q^2 and η^*. The predictions of the NLO direct calculations agree nicely with the data at large Q^2 or at large E_T^* for arbitrary η^*. On the other hand, the theory prediction clearly fails to describe the data in the forward jet region at low Q^2 and low E_T^*. The low

[2]The centre-of-mass energy of the hard process is related to the total ep centre-of-mass energy as $\hat{s} = yx_\gamma x_p s_{ep}$.

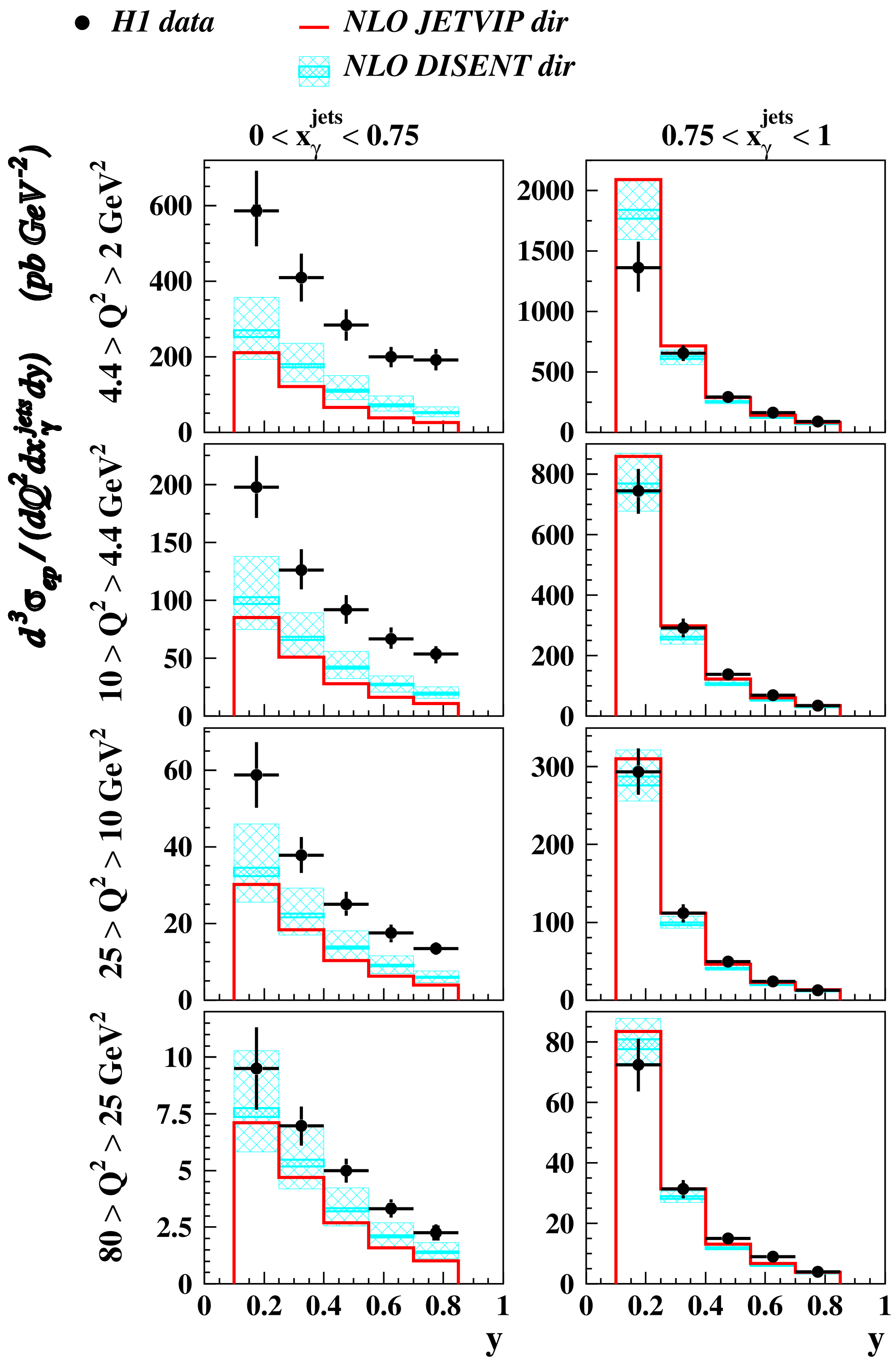

Figure 6.2: Triple differential event cross section $\mathrm{d}^3\sigma_{\mathrm{ep}}/\mathrm{d}Q^2\mathrm{d}x_\gamma^{\mathrm{jets}}\mathrm{d}y$. See the caption of Fig. 6.1 for further details.

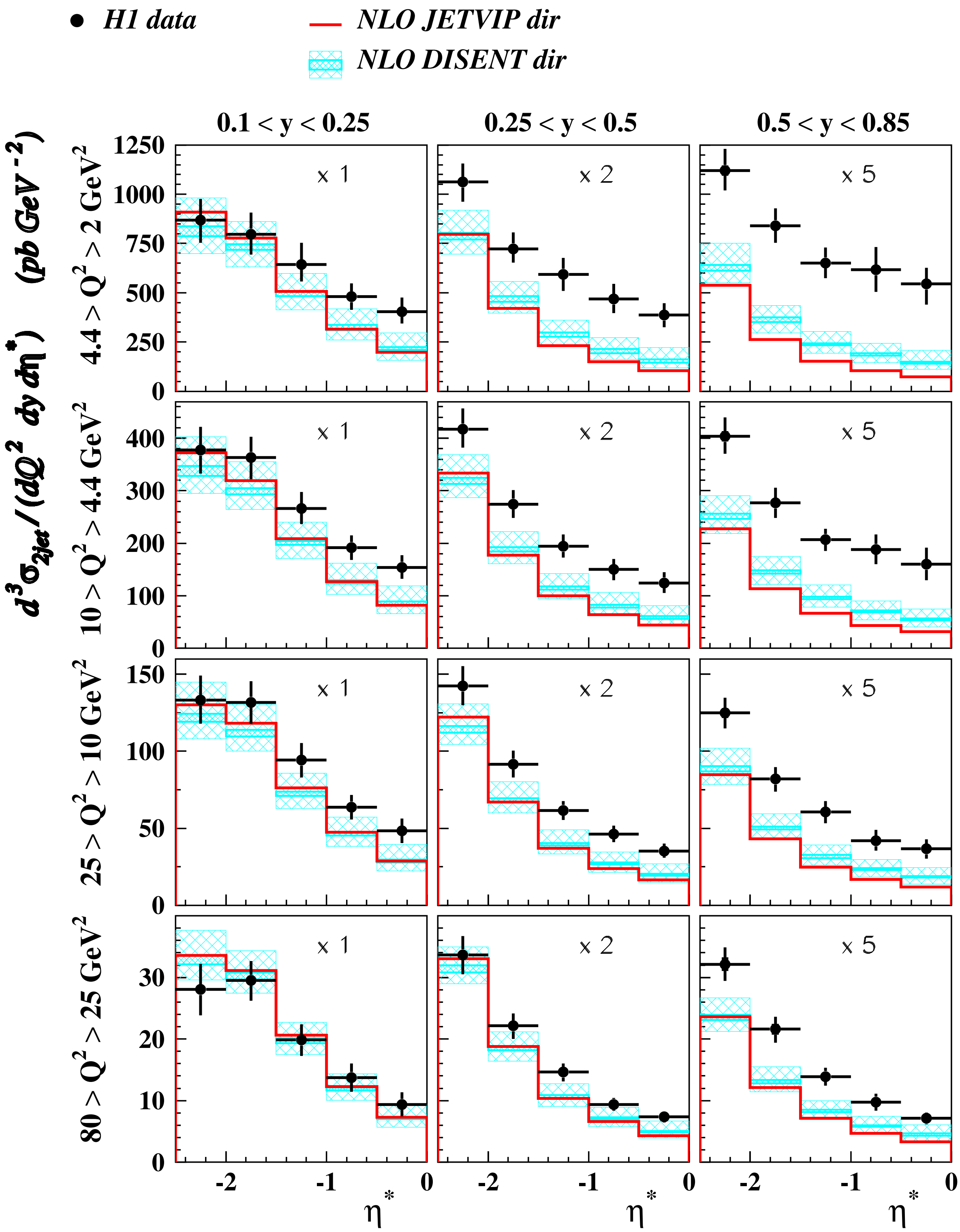

Figure 6.3: Triple differential dijet cross section $\mathrm{d}^3\sigma_{2\mathrm{jet}}/\mathrm{d}Q^2\mathrm{d}y\mathrm{d}\eta^*$. Negative values of η^* correspond to the photon fragmentation region (the so-called backward direction). See the caption of Fig. 6.1 for further details.

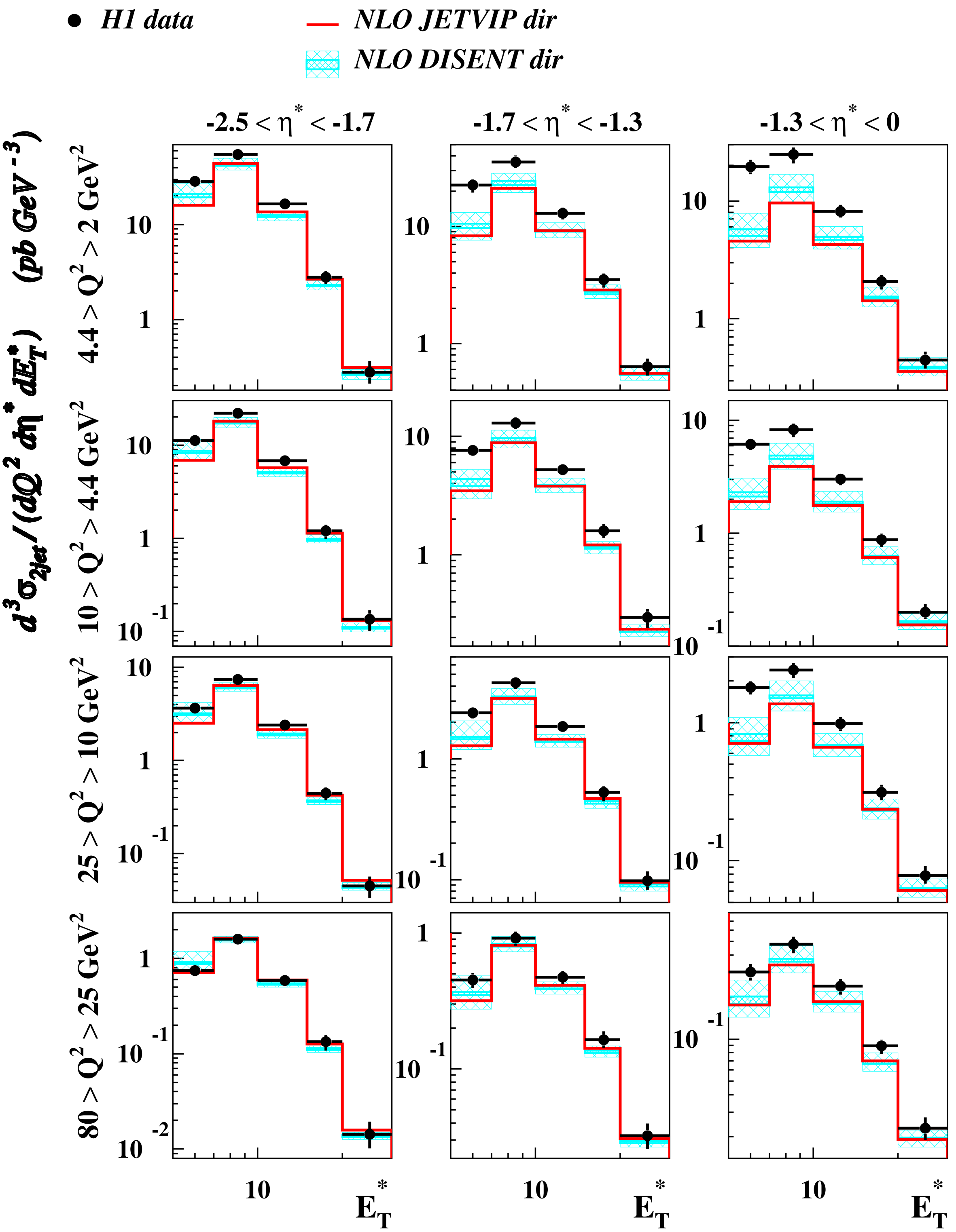

Figure 6.4: Triple differential dijet cross section $\mathrm{d}^3\sigma_{2\mathrm{jet}}/\mathrm{d}Q^2\mathrm{d}\eta^*\,\mathrm{d}E_T^*$. See the caption of Fig. 6.1 for further details.

E_T^* region gets better described as η^* is reduced or Q^2 is increased. A similar discrepancy between the data and NLO prediction has recently been reported for inclusive single jet cross sections in a similar kinematic range [H102b].

The above comparisons convincingly demonstrate that in the region of low Q^2, high y, forward η^* and low E_T^* the data lie significantly above direct NLO QCD calculations. This excess cannot be accommodated within the standard theoretical uncertainties coming from scale variation and hadronisation corrections, neither within the statistical and systematic error of the measurement.

6.1.2 Approximation of the NLO Calculations by the LO Ones

Motivated by the discussion at the end of Section 1.5, we now make a connection between the NLO direct and LO direct plus LO resolved photon contributions. Figure 6.5 presents a comparison of the LO parton level predictions obtained in HERWIG by summing the LO direct and LO resolved photon contributions with the NLO parton level predictions calculated by DISENT[3]. In this figure all initial and final state QCD parton showers as well as hadronisation and soft underlying events were switched off and only the pure QED photon PDF, $D_{i/\gamma}^{\mathrm{QED}}$, see Eqs. (1.11) and (1.13), have been used. As one can see in Fig. 6.5, the sum of LO direct and LO resolved photon contributions of both transverse and longitudinal polarisation is very close to the NLO direct prediction of DISENT in most of the bins[4]. A significant discrepancy between the two approaches at low E_T^*, high Q^2 and $x_\gamma^{\mathrm{jets}} < 0.75$ is not surprising, since there the main theoretical condition for the validity of the resolved photon concept, namely $E_T^2 \gg Q^2$, is not fulfilled, and $D_{i/\gamma}^{\mathrm{QED}}$ in the LO resolved contribution are explicitly set to zero for $E_T^2 < Q^2$. The difference in the high x_γ^{jets} bins at low E_T is probably due to the asymmetric cuts on E_T of the jets, which may decrease the LO direct calculation in the lowest E_T^* bin, since in this case the transverse energy of the two outgoing partons are necessarily equal and larger than the upper cut on E_T, i.e. $E_{T\,1}^* = E_{T\,2}^* > 7\,\mathrm{GeV}$. Contrary to that, in the case of NLO there can be also events with $5 < E_{T\,2}^* < 7\,\mathrm{GeV}$ contributing to that bin.

The recent measurement of inclusive single jet cross sections [H102b] indicated that the region where the NLO calculations fail to describe the data, i.e. the region of forward jets, low E_T^* and low Q^2, corresponds to the region where the ratio of NLO/LO predictions is largest. The same is true for the dijet cross sections, which can be seen in Fig. 6.5 by comparing the LO direct and NLO predictions. The k-factors are smallest at largest Q^2 and largest E_T^* of the jets, i.e. $k = 1.3$, while for smallest Q^2 and smallest E_T^* the k-factor reaches the value $k = 4.2$.

[3]We have checked that the LO direct predictions computed by DISENT (not shown) is basically equivalent to that performed with HERWIG or JETVIP. The same is true for the LO resolved components of HERWIG and JETVIP.

[4]Both HERWIG and DISENT predictions in Fig. 6.5 are shown without the hadronisation corrections.

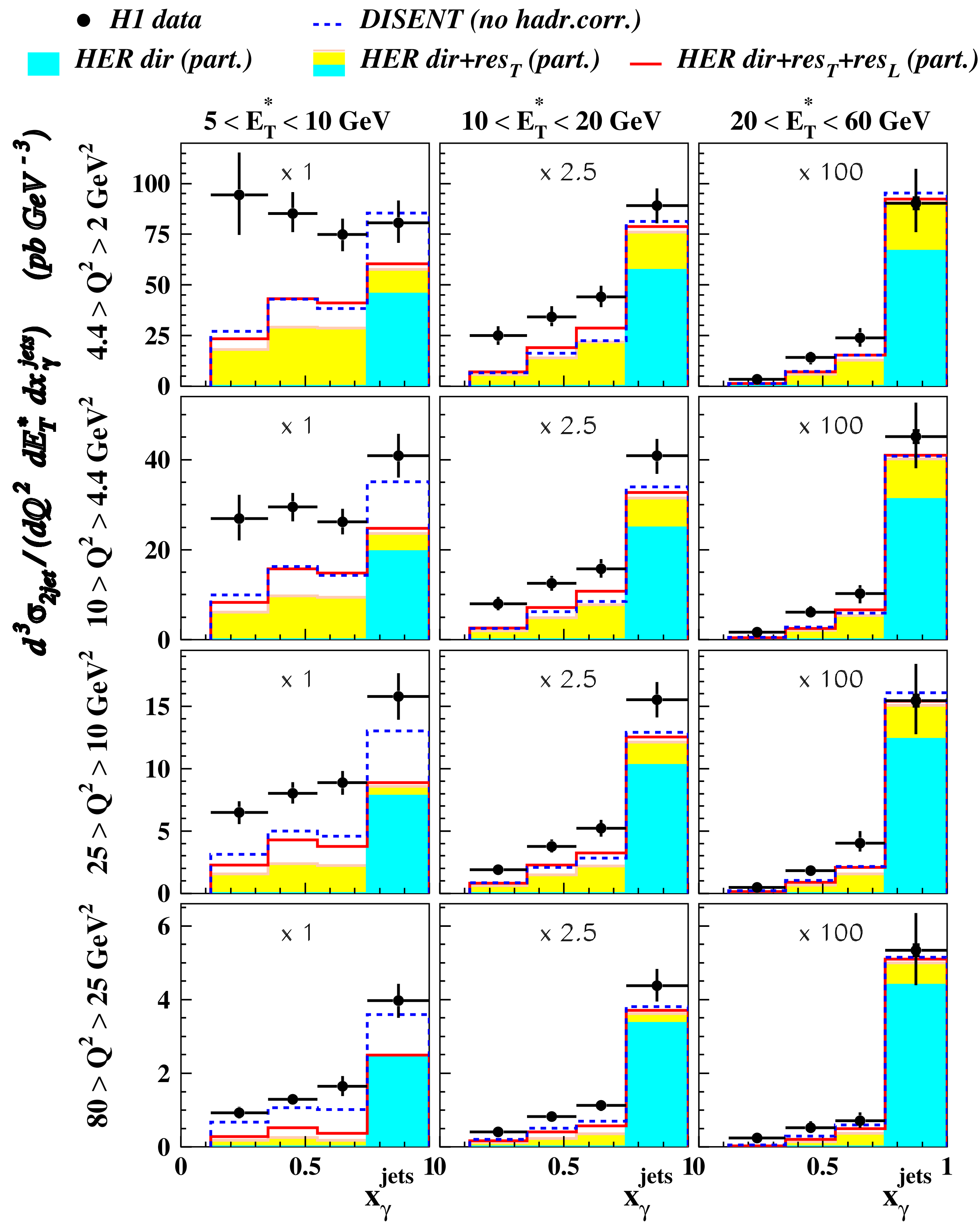

Figure 6.5: The triple differential dijet cross section $\mathrm{d}^3\sigma_{2\mathrm{jet}}/\mathrm{d}Q^2\mathrm{d}E_T^*\,\mathrm{d}x_\gamma^{\mathrm{jets}}$ for the H1 data depicted by points is compared with the predictions of DISENT NLO calculations without the hadronisation corrections (dashed line) and the HERWIG MC program at the parton level, i.e. with no hadronisation, no initial and final state parton showers, using only QED PDF of γ_T^* and γ_L^*, and an NLO PDF of the proton. The dark-filled histograms stand for the direct HERWIG contribution, the light-filled ones for the resolved γ_T^* HERWIG prediction and the full line is the sum of all direct, γ_T^* and γ_L^* resolved HERWIG contributions.

6.1.3 Resolved Virtual Photons in NLO calculations

The pattern of the observed discrepancy between the data and NLO calculations in Figs. 6.1-6.4 suggests an explanation in terms of interactions of the resolved virtual photon understood as an approximation to direct contributions beyond the NLO. Of the NLO parton level calculations only JETVIP includes the resolved virtual photon contribution[5]. Unfortunately, as demonstrated in Section 5.3 (Fig. 5.4), the dependence of the NLO JETVIP calculations of the resolved γ_T^* contribution (i.e. up to order $\alpha\alpha_s^3$) on the slicing parameter y_s is much less constant than those of the direct component. The resulting cross sections are therefore less reliable. Nevertheless, in the absence of other calculations of this kind, the data are compared with the results of the full JETVIP calculations.

First of all, in Fig. 6.6, we compare the data with JETVIP prediction in which the resolved component is taken only in the LO, i.e. diagrams like those in Fig. 1.3 e are ignored in the calculation. Also plotted are the direct part of the JETVIP calculation and the direct part after the subraction of the splitting term (see. Section 1.5). Compared to the NLO direct component of JETVIP, the full JETVIP prediction, employing only the LO resolved photon contribution, decreases the cross section at high x_γ^{jets} while increases it at low x_γ^{jets}. This is in a perfect agreement with the intuitive expectation that can be deduced from Fig. 1.4 – the splitting term, which corresponds to the LO resolved contribution with QED PDF of the photon and is subracted from the direct component of JETVIP, is in the region of $x_\gamma^{\mathrm{jets}} \sim 1$ larger than the LO resolved cross section employing a QCD-improved PDF of photon (SaS1D in our case). In the region of low x_γ^{jets}, it is the other way round.

We can see that adding the LO resolved component to direct part of JETVIP tends to bring the NLO prediction closer to the data, however the improvement is small.

If we include also the NLO contributions (i.e. those exemplified by Fig. 1.3 e) in the resolved photon contribution, the description of the data by JETVIP significantly improves, as can be seen from Figs. 6.7 and 6.8. The inclusion of the NLO resolved γ_T^* contribution brings the NLO calculations closer to the data, in both two cross sections presented, though there is still a remaining discrepancy between the data and calculations at low to moderate x_γ^{jets} and low Q^2, or equivalently, at large η^* and low Q^2. The incorporation of some kind of QCD parton shower mechanism, which is not yet part of the NLO calculations, would presumably further improve the agreement with the data – similarly as it does in the case of LO MC generators (as will be demonstrated in Section 6.2, Figs.. 6.9 and 6.10). Also the NLO resolved γ_L^* contribution, which is not yet implemented within the standard JETVIP code, is expected to improve the description of data [CT00b, CT01].

As a conclusion of Section 6.1, we clearly see a need for contributions beyond the NLO direct calculations.

---

[5] Only the contribution of transversely polarised resolved photons is implemented in JETVIP, while the longitudinal resolved photons are omitted.

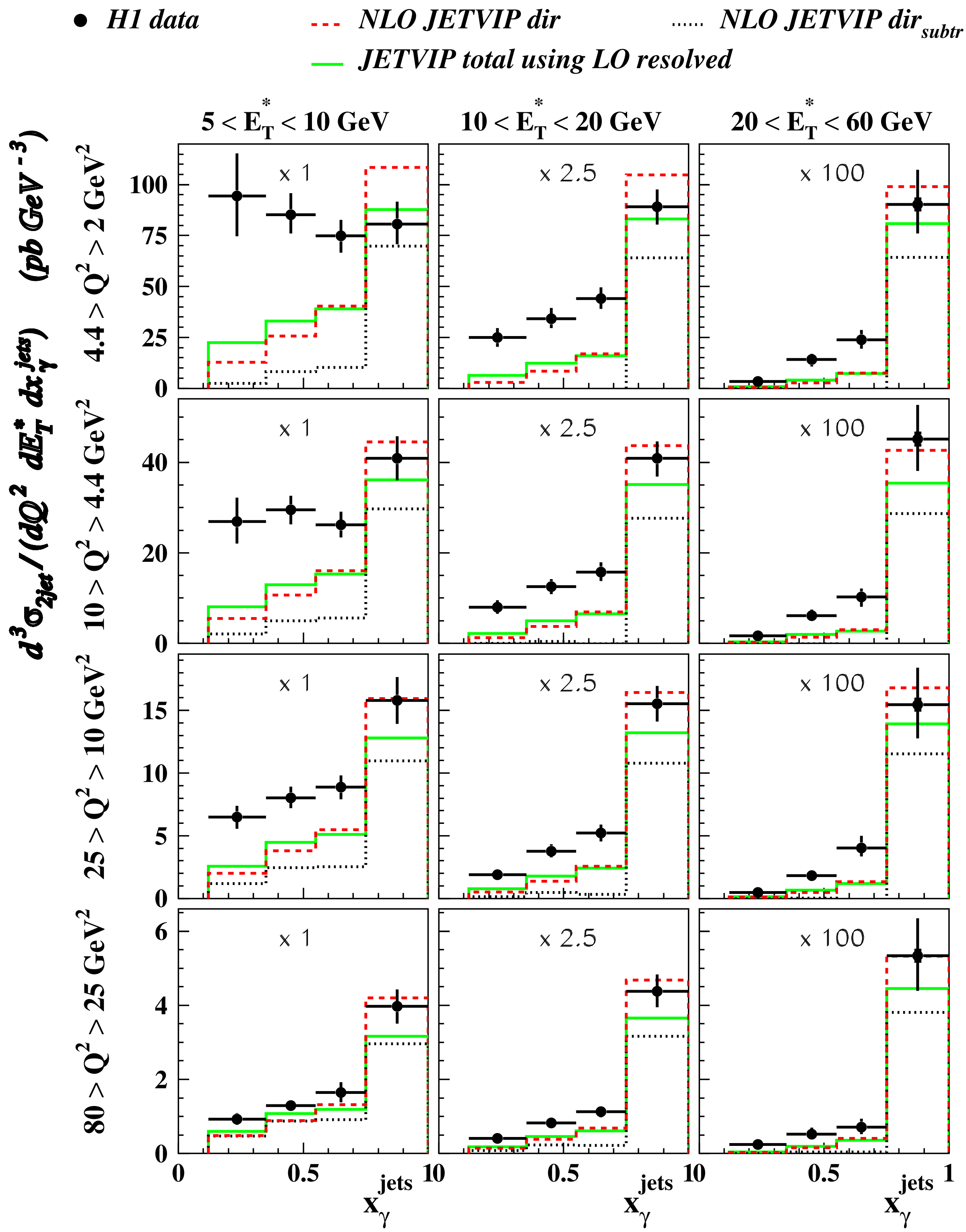

Figure 6.6: Triple differential dijet cross section $\mathrm{d}^3\sigma_{2\mathrm{jet}}/\mathrm{d}Q^2\mathrm{d}E_T^*\,\mathrm{d}x_\gamma^{\mathrm{jets}}$. The data are compared with the NLO JETVIP calculations in which only the LO part of the resolved contribution is taken into account. Also shown are the NLO direct JETVIP calculations before and after the subtraction of the splitting term. The calculations are corrected for the hadronisation effects.

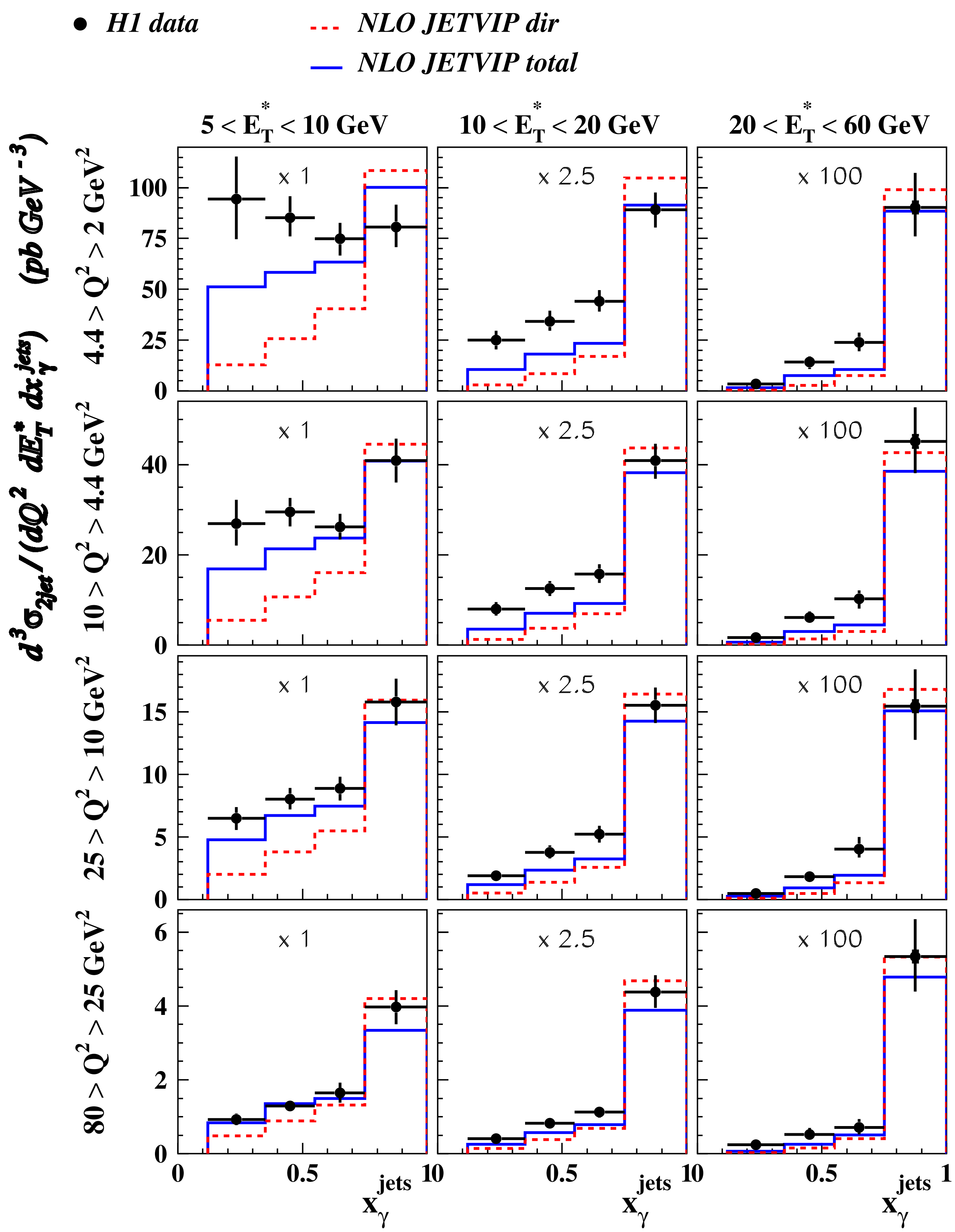

Figure 6.7: Triple differential dijet cross section $\mathrm{d}^3\sigma_{2\mathrm{jet}}/\mathrm{d}Q^2\mathrm{d}E_T^*\,\mathrm{d}x_\gamma^{\mathrm{jets}}$. The data are compared with the NLO JETVIP calculations including the NLO resolved photon contribution (NLO JETVIP total). Also shown is the NLO direct JETVIP calculation before the subtraction of the splitting term (NLO JETVIP dir). The calculations are corrected for the hadronisation effects.

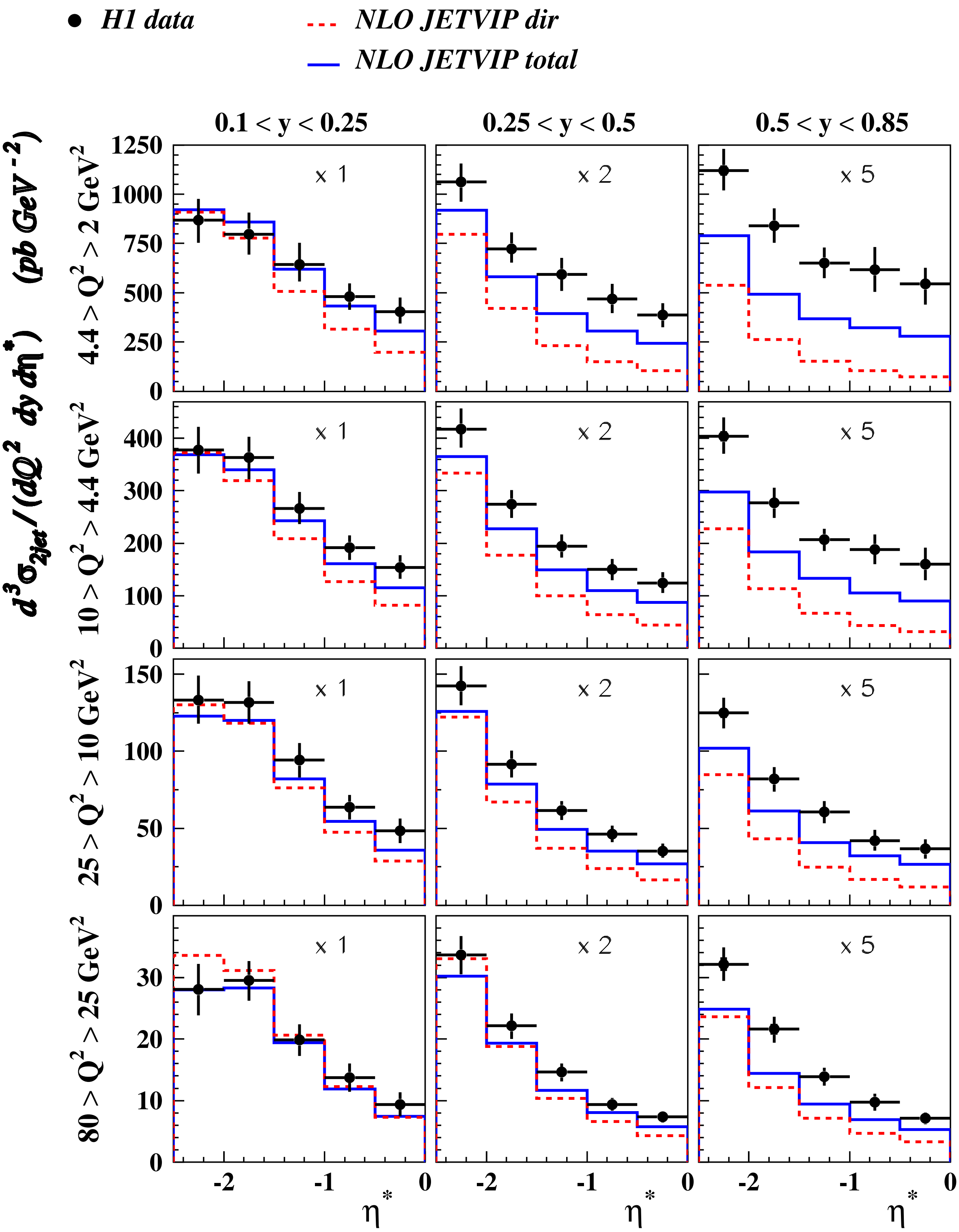

Figure 6.8: Triple differential dijet cross section $\mathrm{d}^3\sigma_{2\mathrm{jet}}/\mathrm{d}Q^2\mathrm{d}\eta^*\,\mathrm{d}E_T^*$. See the caption of Fig. 6.7 for further details.

6.2 Comparison with the DGLAP Monte Carlo Models

The parton level calculations discussed in the context of Figs. 6.1-6.8 ignored initial and final state QCD parton showers and possible effects of the soft underlying event. Realistic MC models take all these effects into account. Their importance together with the QCD improvements of the photon PDF, D_{i/γ^*}, is demonstrated in Fig. 6.9. Once all these effects are included, the cross sections predicted by the sum of all HERWIG components[6] are in a good agreement with the data. The improvement in the low x_γ^{jets} region is especially striking. Our detailed studies made with HERWIG and presented in Fig. 6.10 indicate that the largest change of the cross section originates from the initial and final state QCD parton showers, which take into account correct kinematics, as discussed at the end of Section 1.8. These effects increase the total dijet cross section in our kinematic region by typically 30% and in part of the phase space, namely for low Q^2, low E_T^* and low x_γ^{jets}, by as much as 100%. Another 10% increase of the total dijet cross section arises from the change from QED to QCD-improved D_{i/γ^*}. The influence of different effects on the total dijet cross section is summarised in detail in Table 6.1. Contrary to the studies done in

Parameter	**Direct**	**Resolved** γ_T^*	**Resolved** γ_L^*	**Total**
Standard setting	100%	100%	100%	100%
NLO PDF of the proton	95.4%	98.9%	101.0%	97.4%
QED PDF of γ^*	100%	74.8%	86.7%	89.7%
No I.P.S.	79.2%	74.9%	64.4%	75.3%
No sue	100%	93.2%	90.6%	96.2%
(if sue=30%)	(100%)	(113.1%)	(118.7%)	(107.4%)
No hadronisation, no sue	96.6%	103.1%	103.6%	99.9%
No hadr., no I.P.S., no F.P.S.	67.4%	75.9%	63.6%	69.5%
All changes together	55.6%	54.4%	43.2%	53.1%

Table 6.1: Influence of different parameters on the cross section in HERWIG.

Fig. 6.10, where the parameter setting is changed sequentially, i.e. one parameter at a time is changed in addition to the previously changed ones, in Table 6.1 only the parameters mentioned in the left column of the appropriate raw of the table are varied with respect to the standard HERWIG setting[7]. The table quantitatively illustrates different effects on the total dijet cross section.

[6] The total HERWIG prediction is given as a sum of direct and transverse and longitudinally polarised resolved photon contributions.

[7] In "standard HERWIG prediction" we simulate initial and final state QCD parton showers, hadronisation, soft underlying interactions, QCD-improved PDF of the photon and LO PDF of photon and proton as described in Section 1.8 and Table 1.1.

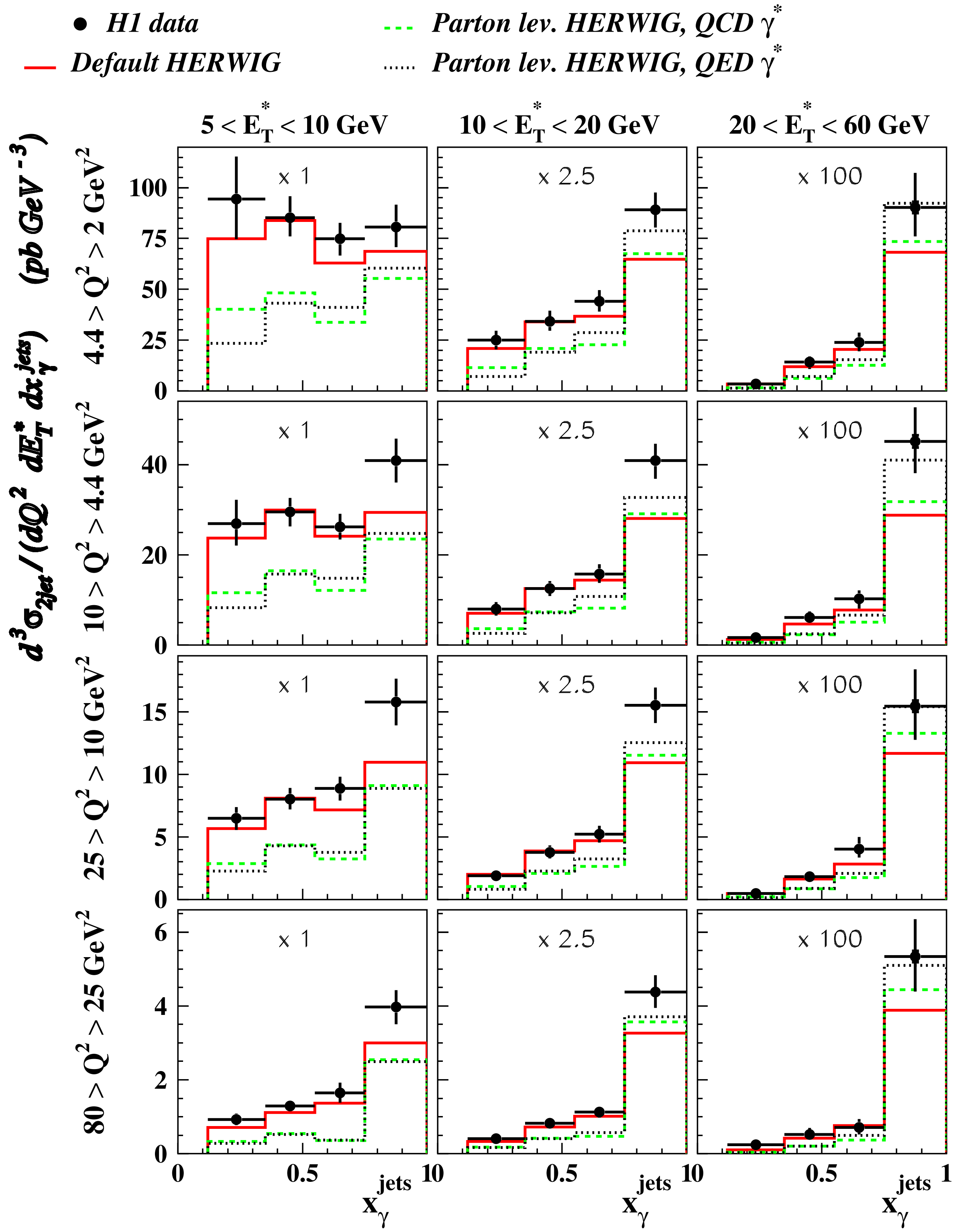

Figure 6.9: Triple differential dijet cross section $d^3\sigma_{2\mathrm{jet}}/dQ^2 dE_T^* dx_\gamma^{\mathrm{jets}}$. The data are compared with the standard HERWIG prediction (full line) and the parton level HERWIG predictions without the parton showers, hadronisation and soft underlying event using the pure QED photon PDF (dotted line) or the QCD-improved one (dashed line). The HERWIG cross sections are obtained as sum of the direct, γ_T^* and γ_L^* resolved photon contributions.

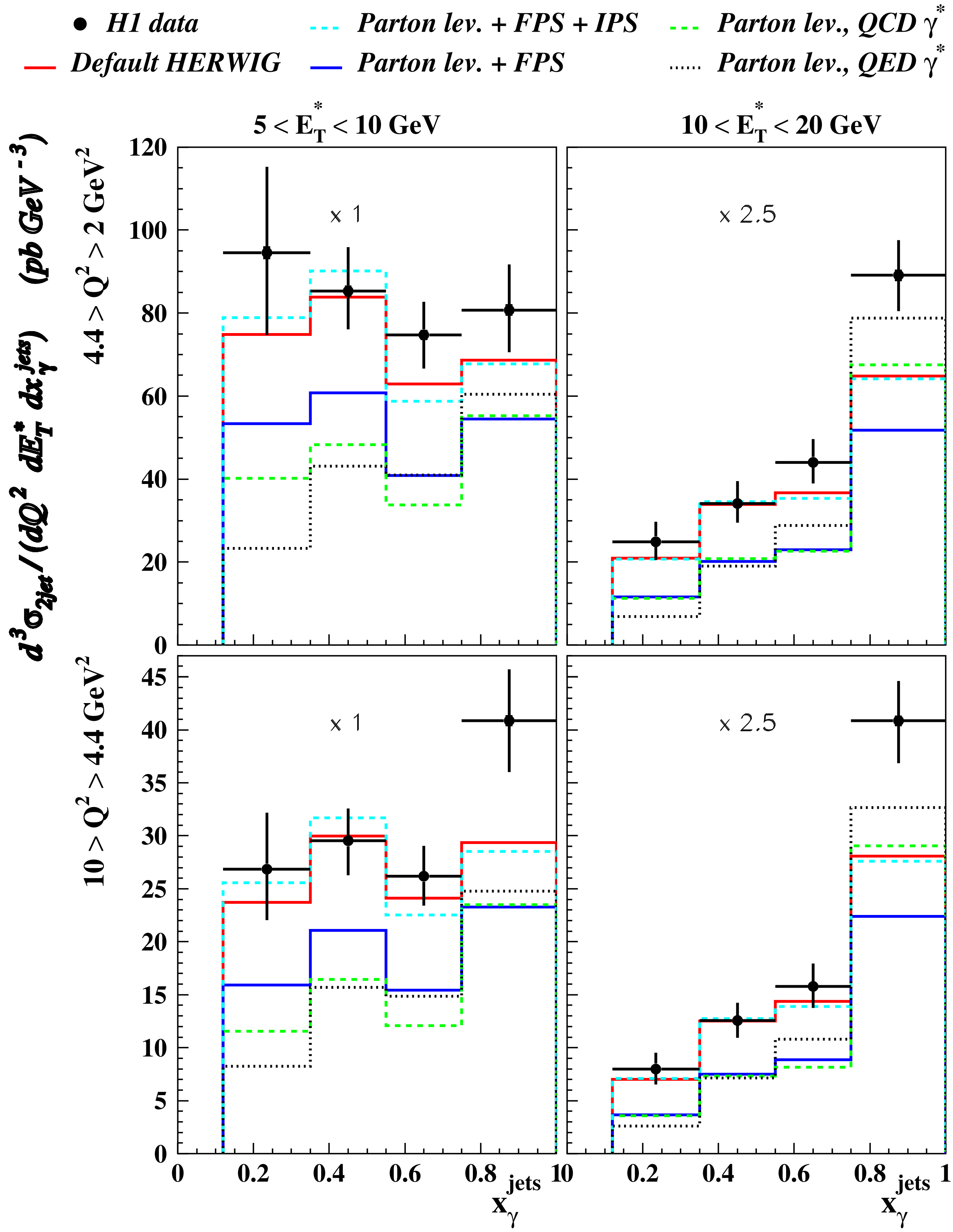

Figure 6.10: Triple differential dijet cross section $\mathrm{d}^3\sigma_{2\mathrm{jet}}/\mathrm{d}Q^2\mathrm{d}E_T^*\,\mathrm{d}x_\gamma^{\mathrm{jets}}$ (a detailed version of Fig. 6.9). The data are compared with the different HERWIG predictions shown already in Fig. 6.9. Also shown are the HERWIG parton level cross sections with final state QCD parton showers (full line) and with both initial and final state QCD parton showers (upper dashed line).

Table 6.1 and Figs. 6.9 and 6.10 indicate that the QCD parton showers and QCD-improved D_{i/γ^*} significantly increase the predicted cross sections and bring them closer to data. One can therefore expect that the same would be true for the NLO calculations, were the NLO programs able to simulate QCD parton showers. Unfortunately, present programs for NLO calculations do not allow us to do that.

Figure 6.11 compares[8] the data separately with direct, γ_T^* and γ_L^* resolved photon contributions of standard HERWIG. The HERWIG direct contribution alone reasonably describes the shape of $x_\gamma^{\rm jets}$ distribution of the data in the highest Q^2 bin, while at low Q^2 the resolved photon contribution is clearly needed. Previous analyses of ep collisions employing the resolved photon contribution have ignored the interactions of longitudinally polarised virtual photons. Figure 6.11 provides evidence that their contribution improves the LO prediction. Not only do they increase the magnitude of the HERWIG predictions to better match the data, but they also correctly reproduce the Q^2 and E_T^* dependence. For a given interval of E_T^*, the ratio of γ_L^* to γ_T^* contributions increases with Q^2, whereas keeping Q^2 fixed it decreases with increasing E_T^*. This behaviour is expected from Eqs. (1.11) and (1.12), and it is crucial for a successful description of the data. Enhancing the PDF of γ_T^* in the resolved photon contribution by a constant factor would not lead to a comparably successful description of the data.

The highest $x_\gamma^{\rm jets}$ region in Fig. 6.11 is not described well by HERWIG. The RAPGAP prediction (not shown) is higher than HERWIG but still significantly below the data. The reason why LO MC programs do not reproduce the data in this region is not fully clear. In HERWIG, the problem can be partially explained by the cut on high $x_\gamma^{\rm gen}$ in the resolved photon interactions described in Section 5.5.

According to the y-dependence of the photon fluxes in Eqs. (1.23) and (1.24), the shape in y of the dijet cross section in the region of $x_\gamma^{\rm jets} < 0.75$ depends significantly on the presence or absence of a contribution from γ_L^*. In Fig. 6.12 we show the event cross section as a function of y in different bins of Q^2 and $x_\gamma^{\rm jets}$. The addition of the resolved longitudinal photon contribution brings the y dependence of the HERWIG predictions much closer to the data, and the ratio of the contributions from γ_L^* and γ_T^* decreases with increasing y as expected from Eqs.(1.23) and (1.24). The small contribution of γ_L^* compared to γ_T^* at large $x_\gamma^{\rm jets}$ is a consequence of the different D_{i/γ_T^*} and D_{i/γ_L^*} dependence on x_γ in Eqs. (1.11) and (1.12). Figure 6.12 provides a cross-check of the need for γ_L^* resolved photon contributions presented in Fig. 6.11, which does not show the dependence of the cross section on y. The low HERWIG prediction in the lowest y bin for $Q^2 > 10\,\mathrm{GeV}^2$ and $x_\gamma^{\rm jets} < 0.75$ is in part due to a cut-off procedure in HERWIG which suppresses the PDF of the virtual photon in the region of high x_γ (see Section 5.5). In the same bins resolved γ_T^* contribution of RAPGAP predicts a rise in the cross section with decreasing y similar to that in the data, which will be demonstrated later on in this section in Fig. 6.14. HERWIG underestimates the data also in the region $0.75 < x_\gamma^{\rm jets}$. This is again partially

[8]Prediction of MC program CASCADE, also shown in Fig. 6.11, will be discussed in Section 6.3.

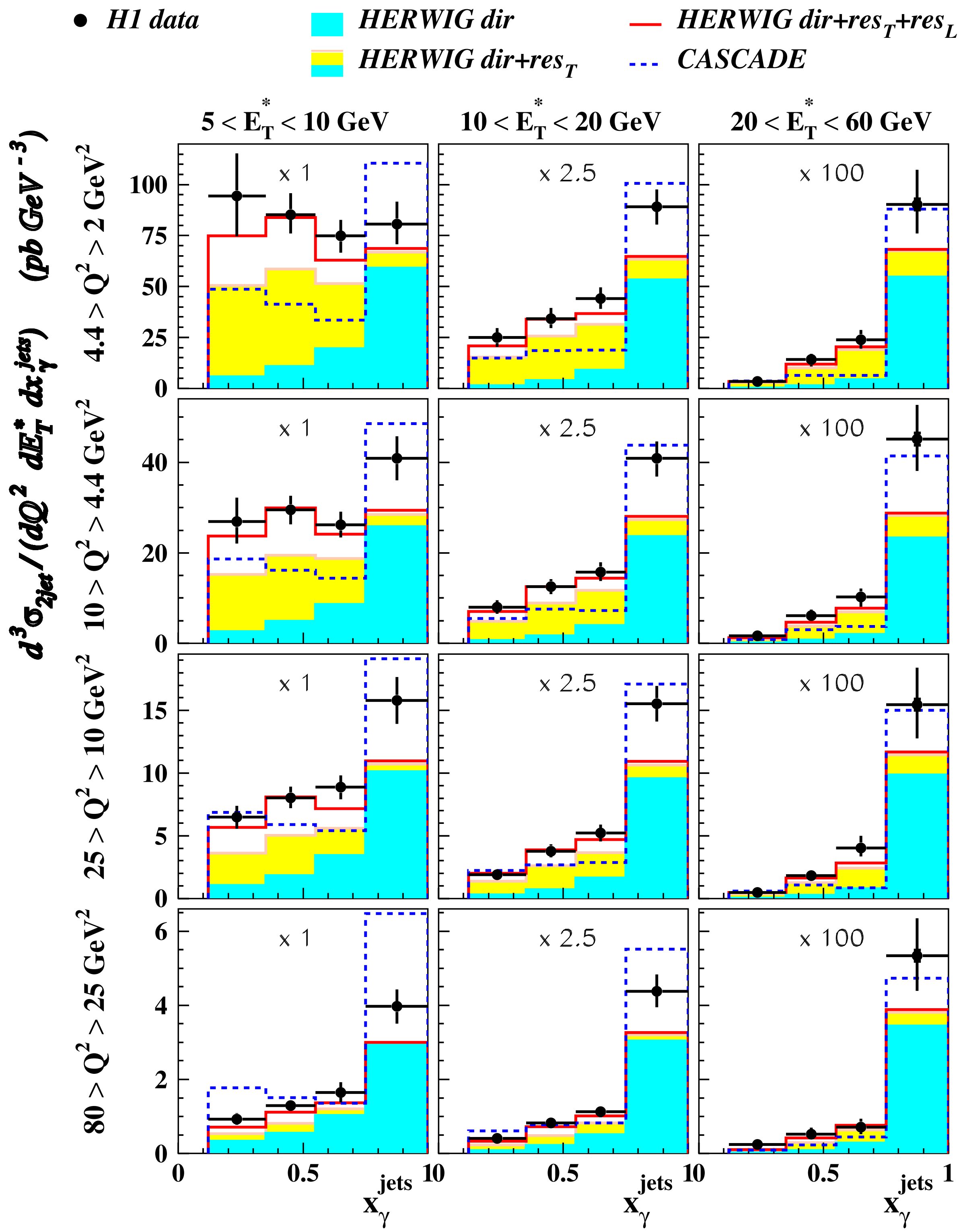

Figure 6.11: The triple differential dijet cross section $d^3\sigma_{2jet}/dQ^2 dE_T^* dx_\gamma^{jets}$ for the H1 data is compared with standard predictions of HERWIG and CASCADE (dashed line). The dark-filled histograms show the direct HERWIG contribution, the light-filled ones the resolved γ_T^* HERWIG prediction and the full line is the sum of all direct, γ_T^* and γ_L^* resolved photon HERWIG contributions.

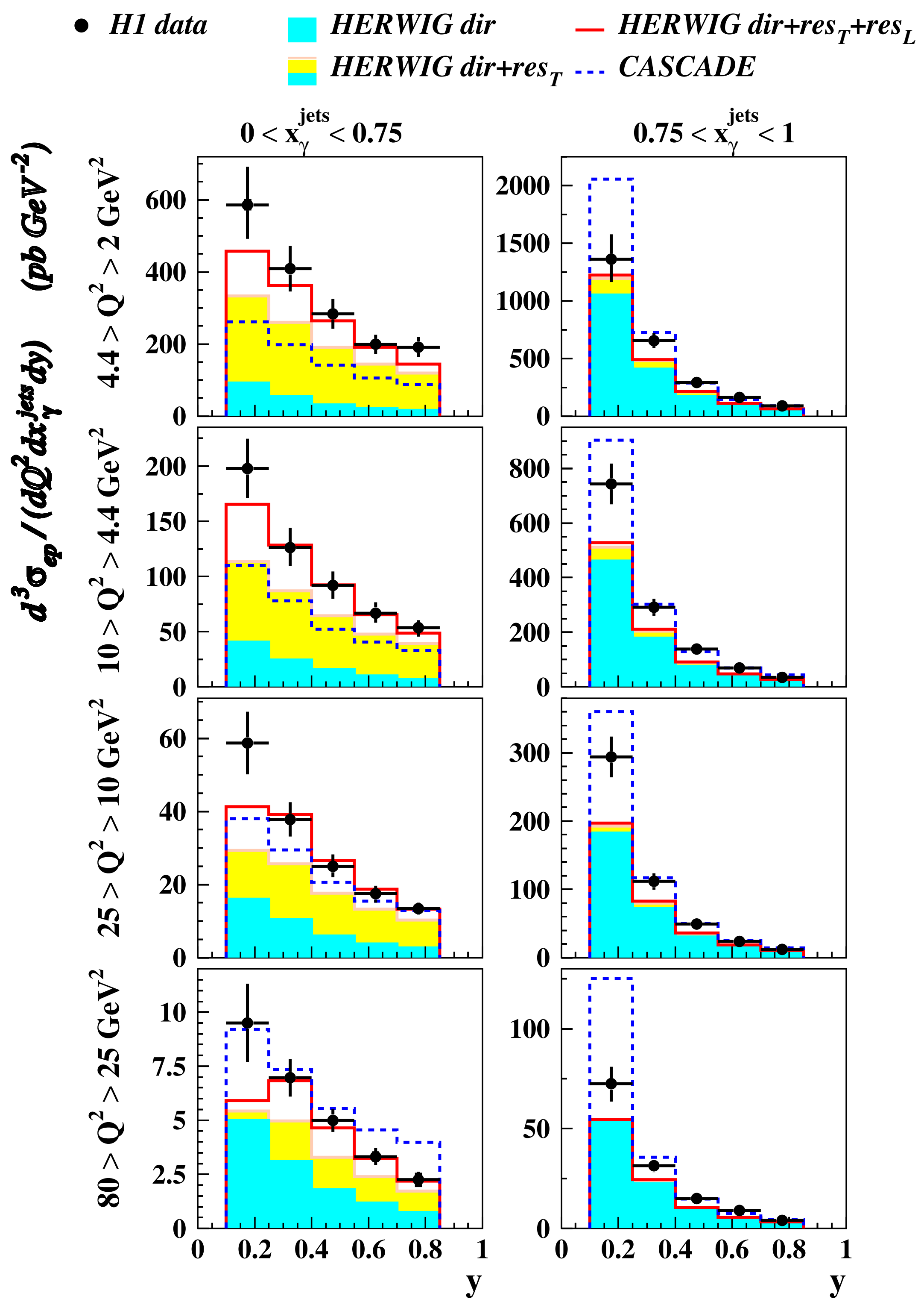

Figure 6.12: Triple differential event cross section $\mathrm{d}^3\sigma_{\mathrm{ep}}/\mathrm{d}Q^2\mathrm{d}x_\gamma^{\mathrm{jets}}\mathrm{d}y$. See the caption of Fig. 6.11 for further details.

due to the cut-off procedure in HERWIG, although even RAPGAP prediction lies below the measurement in that region.

Figure 6.13 compares the measured dijet cross section as a function of η^* in different bins of Q^2 and y with the standard HERWIG prediction. The data are well reproduced by the complete LO MC model in shape, however the absolute normalisation, especially at low y, is not satisfactory. In agreement with the message of Figs. 6.11 and 6.12, the importance of the resolved photon contributions increases in the forward jet region, for low Q^2 and at high y.

To get an estimate of the model dependence of the above conclusions, the data are compared in Fig. 6.14 with both HERWIG and RAPGAP. Since RAPGAP does not include the contribution of resolved γ_L^*, only the direct and resolved γ_T^* components are shown. A decent agreement of both models is found, except for the first bin of y for low x_γ^{jets} and high Q^2. The difference is in part, but not entirely, due to a cut-off procedure in HERWIG which suppresses PDF of the virtual photon in the region close to $x_\gamma = 1$ (see Section 5.5). The higher RAPGAP predictions for the cross section in the lowest y and high Q^2 region suggest that in this region RAPGAP would probably describe data even better than HERWIG, were the contribution of resolved γ_L^* included in RAPGAP.

Figure 6.15 shows the comparison of data and HERWIG with the prediction of PYTHIA. The cross section calculated using PYTHIA is systematically below the measurement as well as below the HERWIG and RAPGAP predictions (note that predictions of the latter two programs for both direct and γ_T^* resolved photon cross sections are in a relatively good agreement, as indicated in Fig. 6.14 for a different distribution). The parameter setting in PYTHIA was as close to that used in HERWIG and RAPGAP as possible. The reason why the cross section predicted by PYTHIA is so low is therefore unknown. The effect of multiple interactions is significant only at low Q^2 and low E_T^*. It increases the cross section in a similar way as the soft underlying activity in HERWIG.

In Fig. 6.15, only the direct and resolved γ_T^* components are shown. It is possible to simulate also the resolved γ_L^* contribution in PYTHIA, however only in the approximation using the PDF of the transverse photon reweighted by a simple multiplicative expression [FS00]. Several such expressions have been suggested by the authors of PYTHIA, each of them containing a free parameter. The prediction of the contribution of longitudinal photons to the dijet cross section strongly depends on the choice of multiplicative expression and on the value of the free parameter, which leads to variation of γ_L^* contribution within orders of magnitude. Since furthermore the prediction of PYTHIA for direct and γ_T^* resolved contribution significantly underestimates the data, it is not possible to make any conclusion about the γ_L^* resolved contribution and we do not even show it in the figure.

We conclude that the effects of QCD improvements of the photon PDF as well as the transverse boost of partons resulting from the simulation of parton showers significantly improves the theoretical description of the data. We clearly see that the contribution from the longitudinally polarised virtual photons further improves agreement with the data.

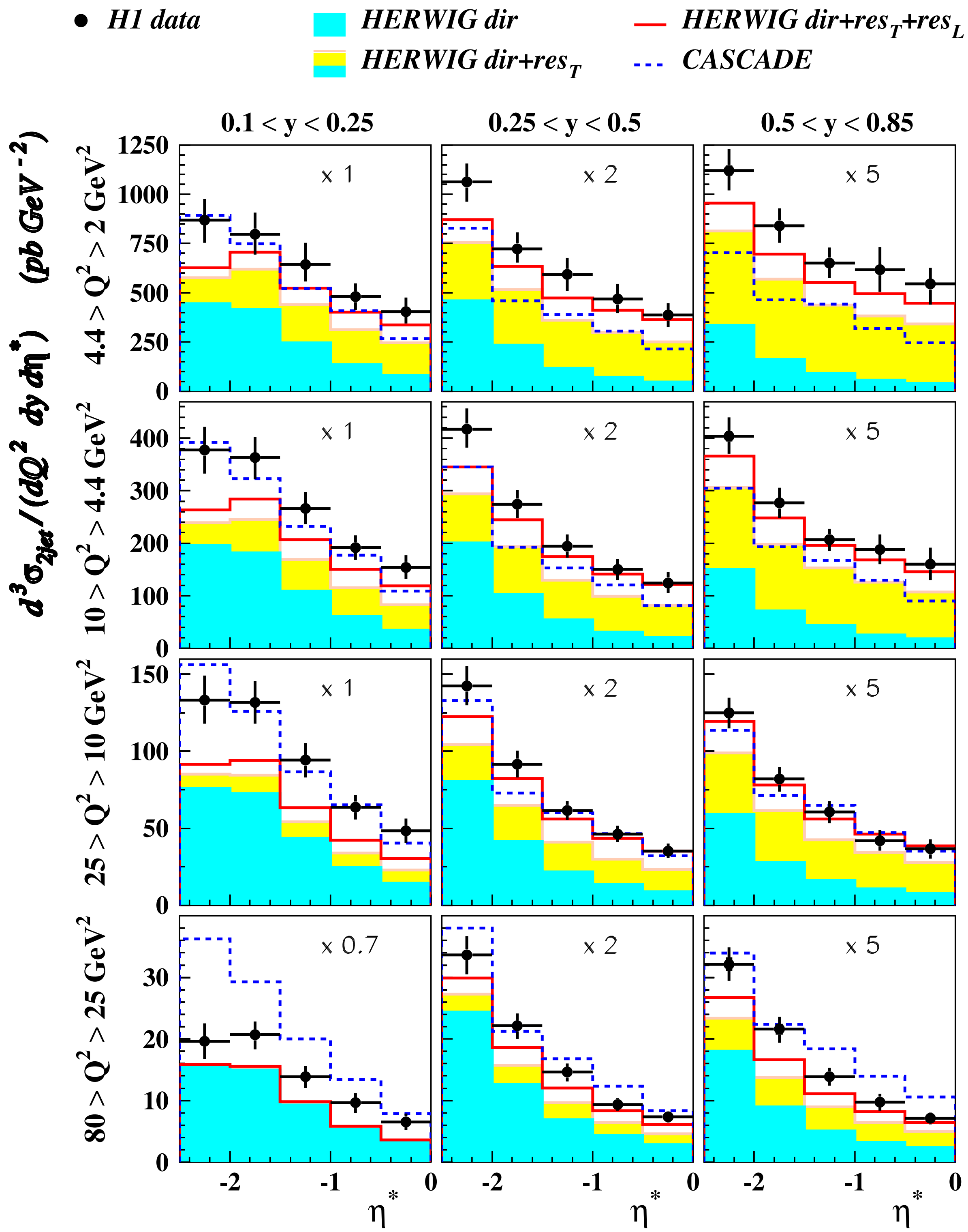

Figure 6.13: Triple differential dijet cross section $\mathrm{d}^3\sigma_{2\mathrm{jet}}/\mathrm{d}Q^2\mathrm{d}y\mathrm{d}\eta^*$. See the caption of Fig. 6.11 for further details.

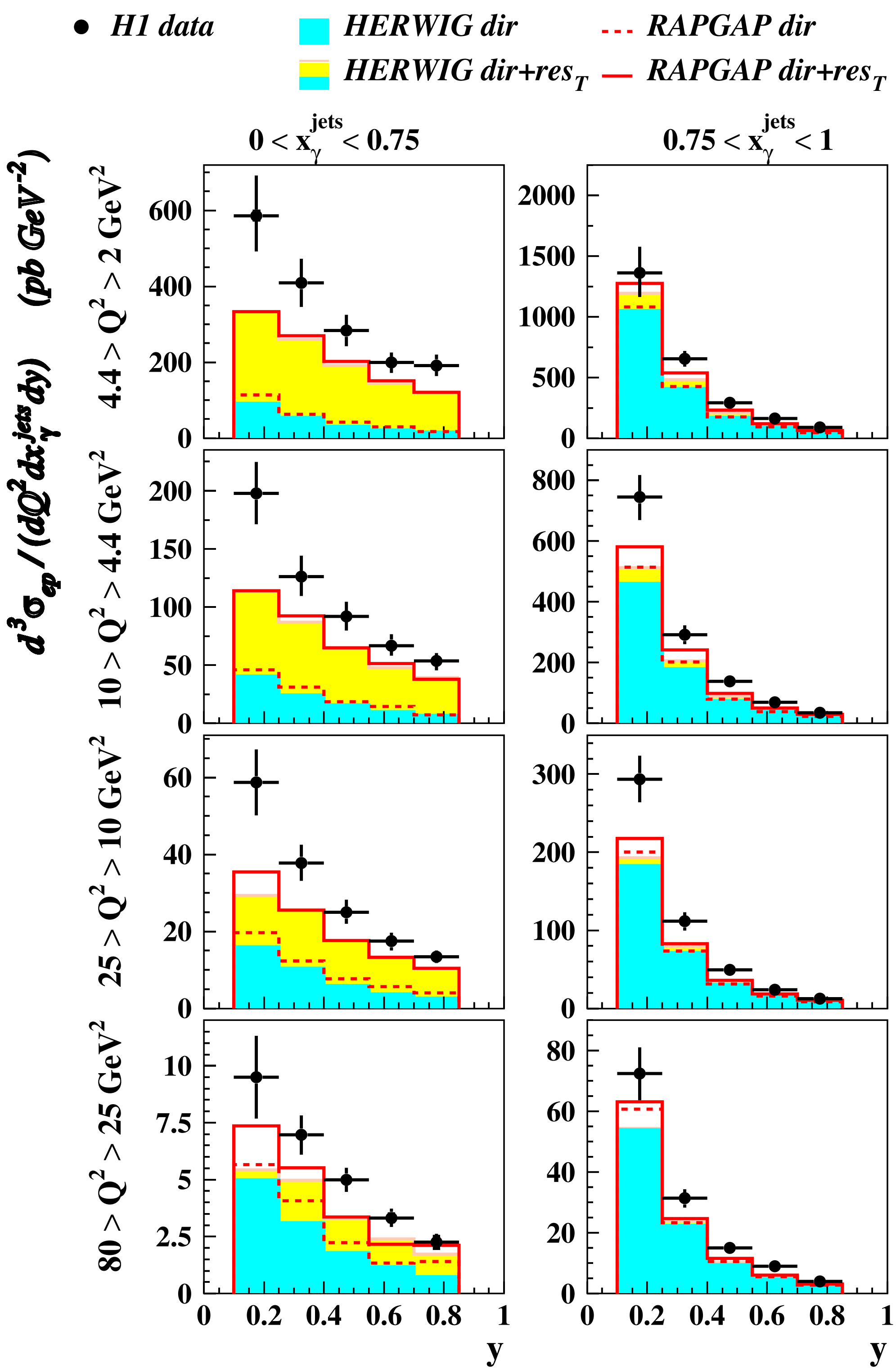

Figure 6.14: Triple differential event cross section $\mathrm{d}^3\sigma_{\mathrm{ep}}/\mathrm{d}Q^2\mathrm{d}x_\gamma^{\mathrm{jets}}\mathrm{d}y$ for the H1 data is compared with predictions of HERWIG and RAPGAP. The dark-filled histograms (full line) show the direct HERWIG (RAPGAP) contribution, the light-filled histograms (dashed line) show the resolved γ_T^* HERWIG (RAPGAP) prediction, respectively.

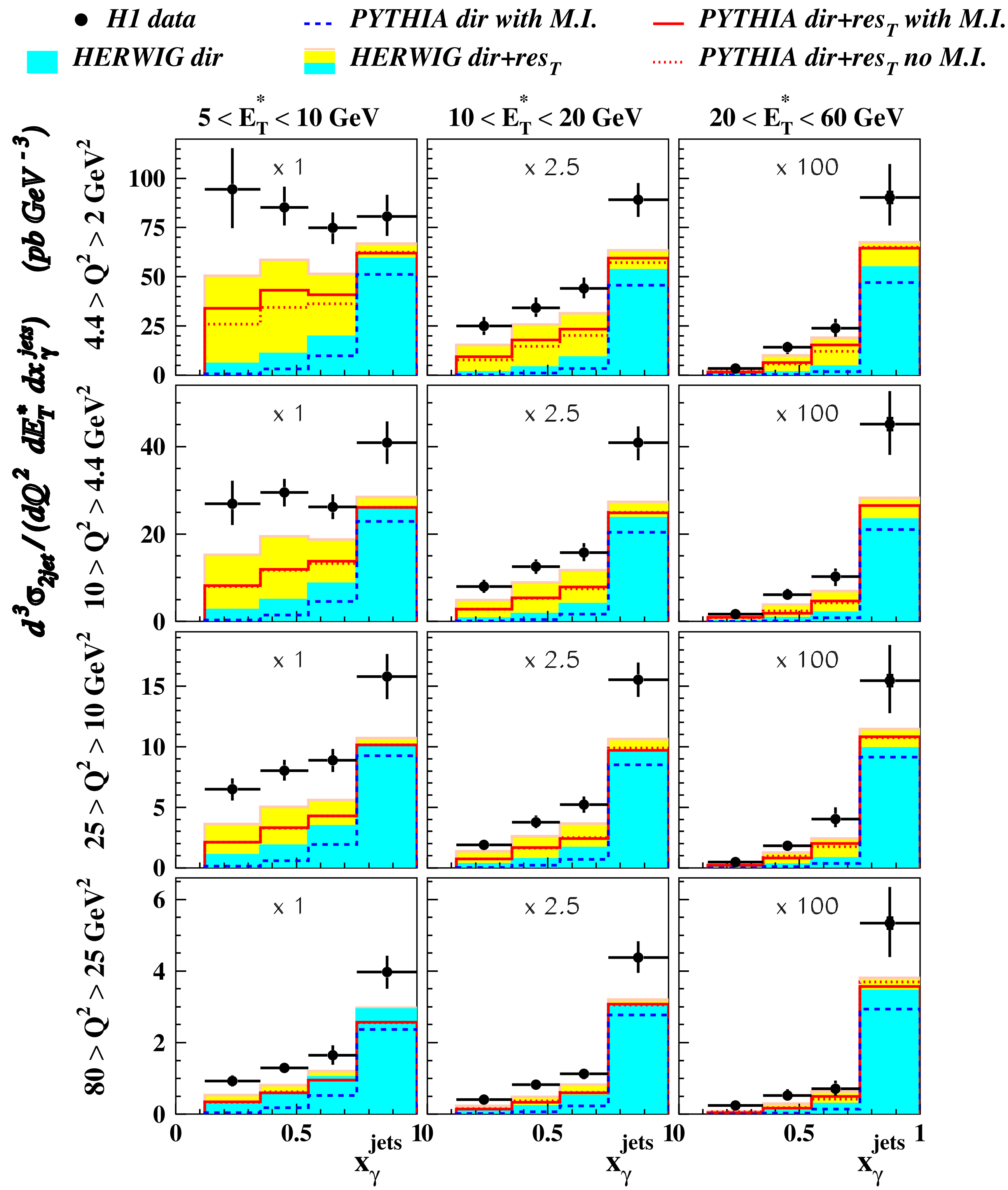

Figure 6.15: Triple differential dijet cross section $\mathrm{d}^3\sigma_{2\mathrm{jet}}/\mathrm{d}Q^2\mathrm{d}E_T^*\,\mathrm{d}x_\gamma^{\mathrm{jets}}$ for the H1 data is compared with predictions of HERWIG and PYTHIA. The dashed line shows direct photon PYTHIA contribution, the full line stands for the sum of direct and transverse resolved photon PYTHIA contributions. These predictions include simulation of the multiple interactions (M.I.), while the dotted line shows the sum of direct and transverse resolved photon PYTHIA contributions without M.I. The data points as well as HERWIG predictions are the same as those shown in Fig. 6.11.

6.3 Comparison with the CCFM Monte Carlo Model

In Figs. 6.11-6.13 the data are also compared with predictions of the CASCADE MC, employing an unintegrated PDF of the proton satisfying the CCFM evolution equations.

The CASCADE predictions describe the main qualitative trends in the data, except the Q^2 dependence in the lowest E_T^* bin (Fig. 6.11) or at low $x_\gamma^{\rm jets}$ (Fig. 6.12). On the other hand, CASCADE predicts a significant dijet cross section at low $x_\gamma^{\rm jets}$ (Fig. 6.11), much higher and closer to data than the LO and NLO DGLAP calculations without the resolved photon contribution. Also, except for the highest Q^2 bin, dijet production in the forward region is reproduced better by CASCADE (Fig. 6.13) than by NLO direct calculations (Fig. 6.3).

The reason why CASCADE does not fully reproduce the Q^2 dependence and the low $x_\gamma^{\rm jets}$ region could be partially explained by the fact that only gluons are considered in the parton cascade from the proton side. This is a good approximation in the very low x_p region, which is however not accessible in this analysis due to the limited centre-of-mass energy of the ep collisions at HERA.

We have also observed high sensitivity of the CASCADE predictions to the input parameterisations of the unintegrated PDF of the proton. This is demonstrated in Fig. 6.16, where three different sets of PDF are used for the proton, which differ in the way the small $k_\perp$ region is treated. Two of them, namely the JS2001 and J2003 set 1, employ the full splitting function including the non-singular term, whereas J2003 set 2 takes into account only the singular terms. The prediction in the high $x_\gamma^{\rm jets}$ region varies only within 10-15% for all three parameterisations, while for low $x_\gamma^{\rm jets}$ we observe high sensitivity to the input PDFs, which reaches 100% in some bins. This fact promises a possible improvement of the CASCADE description of the data once the unintegrated proton PDFs are determined more precisely. On the other hand, high sensitivity of the predictions to the parameterisation of the PDF indicates that the data can be used for their determination.

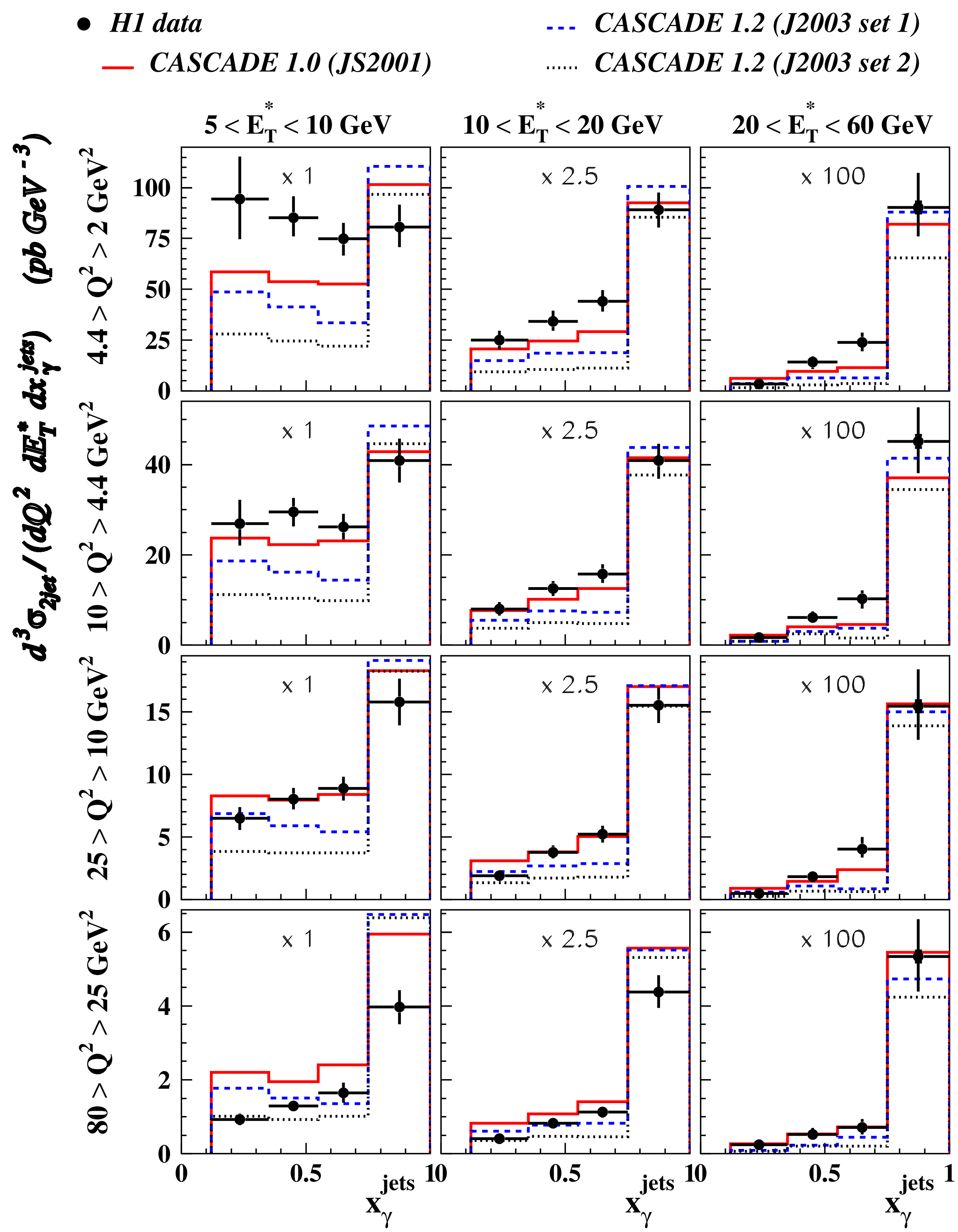

Figure 6.16: Triple differential dijet cross section $\mathrm{d}^3\sigma_{2\mathrm{jet}}/\mathrm{d}Q^2\mathrm{d}E_T^*\,\mathrm{d}x_\gamma^{\mathrm{jets}}$ for the H1 data is compared with predictions of CASCADE with different sets of the unintegrated PDFs of the proton.

Summary

Triple differential dijet cross sections in $e^{\pm}p$ interactions were measured in the region of photon virtualities $2 < Q^2 < 80\,\mathrm{GeV}^2$ and over a wide range of inelasticities $0.1 < y < 0.85$. The data in the kinematic range $E^*_{T\,1} > 7\,\mathrm{GeV}$, $E^*_{T\,2} > 5\,\mathrm{GeV}$ and pseudorapidities $-2.5 < \eta^*_1, \eta^*_2 < 0$ were compared with NLO and LO QCD calculations, with and without resolved photon contributions or parton showers, as well as with a calculation based on k_T factorisation using unintegrated PDFs of the proton within the CCFM evolution scheme.

We have observed a sizable and systematic excess of the data over the NLO calculations of DISENT, which do not include a resolved virtual photon contribution, in the region of $Q^2 < 10\,\mathrm{GeV}^2$, low E^*_T and low x_γ^{jets}, or equivalently, for low Q^2, low E^*_T and large η^*. The excess observed for $x_\gamma^{\mathrm{jets}} < 0.75$ decreases with increasing Q^2.

The NLO calculations incorporating a resolved virtual photon, as implemented in JETVIP, describe the data significantly better than the pure NLO direct photon predictions, though there is still a deficit of the predicted cross section at low x_γ^{jets}, especially for low Q^2. Unfortunately, the JETVIP prediction for the resolved part of the dijet cross section are sensitive to the choice of the slicing parameter y_s and must therefore be taken with caution.

It is also demonstrated that the initial and final state QCD parton showers, which are not taken into account in the NLO QCD calculations, notably increase the predicted cross section in the LO Monte Carlo model HERWIG. They lead to a considerable improvement in the description of the measurement, even though there is still a remaining discrepancy in the region of high x_γ^{jets}.

The best agreement with the data is obtained when both transversely and longitudinally polarised resolved virtual photons are included. Employing the different y dependence of the γ^*_T and γ^*_L fluxes as well as different dependence of D_{i/γ^*_T} and D_{i/γ^*_L} on Q^2 and E^*_T, the first time indication of the resolved photon contribution with the longitudinal polarisation is observed.

Based on the CCFM evolution scheme, CASCADE provides theoretical prediction alternative to the DGLAP-based MC models. Although presently without the concept of virtual photon structure, it predicts significant cross section in the region of low x_γ^{jets} (and correspondingly in the forward jet region), much larger than the direct photon calculations in the LO and NLO programs based on the DGLAP evolution. However, it is still not sufficient for the description of the data in the low x_γ^{jets} region. The CASCADE prediction describes the data best in the region of moderate Q^2 between 10 and 25 GeV^2. The Q^2 dependence of the cross section is less steep than in the data.

In summary, the data show clear evidence for effects that go beyond the fixed-order NLO QCD calculations. The importance of QCD parton showers and of the resolved γ_L^* contribution is demonstrated.

Appendix A

Trigger Definition

The exact definitions of the triggers *s9*, *s61* and *s64* (see page 36) were changing during our data taking period as the experts modified and improved the performance of the whole trigger system. However, the changes were mostly of a minor importance. As an example, we present the complete definitions of our analysis triggers in the run 270049 (taken on April 18, 2000) in the form of logical expressions constructed of trigger elements:

```
s009 SPCLe_IET>1&&
       !SPCLh_AToF_E_1&&!SPCLh_ToF_E_2&&!VETO_inner_BG&&!VETO_Outer_BG&&
       !VLQToF_BG&&
       zVtx_mul<7&&
       (zVtx_T0||FwdRay_T0)&&
       !(DCRPh_NL_many&&DCRPh_NH_many&&DCRPh_PL_many&&DCRPh_PH_many)&&
       ((FToF_IA||FIT_IA)||(!FToF_BG&&!FIT_BG))&&(PToF_IA||!PToF_IA)
     L2[22] SPCL_R30

s061 DCRPh_THig&&zVtx_sig&&(SPCLe_IET>2||SPCLe_IET_Cen_3)&&
       !SPCLh_AToF_E_1&&!SPCLh_ToF_E_2&&!VETO_inner_BG&&
       !VETO_Outer_BG&&!VLQToF_BG&&
       !(DCRPh_NL_many&&DCRPh_NH_many&&DCRPh_PL_many&&DCRPh_PH_many)&&
       (FToF_IA||FIT_IA)||(!FToF_BG&&!FIT_BG)

s064 LAr_IF>1&&LAr_Etrans>2&&
       !SPCLh_AToF_E_1&&!VETO_inner_BG&&!VETO_Outer_BG&&!VLQToF_BG&&
       (zVtx_T0||FwdRay_T0)||(LAr_T0&&!zVtx_T0_nextbc)&&
       ((FToF_IA||FIT_IA)||(!FToF_BG&&!FIT_BG))&&(PToF_IA||!PToF_IA)&&
       RZ_non_vtx||!RZ_non_vtx.
```

Meaning of the logical symbols and definitions of the trigger elements are the following:

&& and,

|| or,

! not.

SPCLe_IET>1: Energy deposited in the SPACAL trigger towers (in the so-called *sliding window*) larger than 2 GeV.

SPCLe_IET>2: Energy deposited in the SPACAL trigger towers larger than 5.7 GeV.

SPCLe_IET_Cen_3: Energy deposited in the central part of the SPACAL above the highest threshold.

DCRPh_THig: At least one track candidate in central jet chamber (CJC) with the transverse momentum above 800 MeV.

zVtx_sig: A signature for the z-vertex found.

LAr_IF>1: Energy in the forward (IF) part of the LAr above 7.5 GeV.

LAr_Etrans>2: Transverse energy in a trigger tower of the LAr above 7.2 GeV.

LAr_T0: Validation of the digital time zero.

SPCLh_AToF_E_1: Energy in the ATOF time-of-flight detector above the first threshold.

SPCLh_ToF_E_2: Energy in the TOF time-of-flight detector above the second threshold.

VETO_inner_BG: Inner veto wall hit in the proton satellite background time window.

VETO_Outer_BG: Outer veto wall hit in the proton satellite background time window.

VLQToF_BG: Hit in the VLQ time-of-flight detector in the proton background time window.

zVtx_mul<7: Less than 200 entries in the z-vertex histogram.

zVtx_T0: At least one ray (a vertex candidate).

zVtx_T0_nextbc: At least one ray in the next BC.

FwdRay_T0: Any multiplicity of rays.

FToF_IA: The hit in forward time-of-flight detector in the main proton satellite time window.

FIT_IA: The forward interaction timing hit in the proton satellite time window.

FToF_BG: The hit in forward time-of-flight detector in late proton satellite time window.

FIT_BG: The forward interaction timing hit in the background or late proton satellite time window.

PToF_IA: PLUG time-of-flight hit in the interaction time window.

DCRPh_NL_many: At least 20 negative low momentum track candidates.

DCRPh_NH_many: At least 20 negative high momentum track candidates.

DCRPh_PL_many: At least 20 positive low momentum track candidates.

DCRPh_PH_many: At least 20 positive high momentum track candidates.

RZ_non_vtx: Upstream background (i.e. many non-vertex tracks).

Appendix B

Reweighting Procedure

To correct the measurement for the QED radiative effects (Section 4.5.1) and detector acceptance and smearing effects (Section 4.5.3), some correction functions have to be determined and applied either to data or to a MC simulation. For this purpose, we used an iterative reweighting procedure described in this section. We shall demonstrate the technique on an example of the reweighting of a MC event sample to fit the measured distributions in the data (see Fig. 4.11 and 4.12), which has been applied before performing the Bayesian unfolding of the detector effects described in Section 4.5.3.

In the example, our aim is to assign additional weights to events simulated by HERWIG such that the MC distributions describe the measured ones. The upper left plot in Fig. B.1 compares x_γ^{jets} distribution for the data with HERWIG before the reweighting procedure. The lower left plot in Fig. B.1 depicts the ratio of these two distributions together with a function $\mathcal{W}(x_\gamma^{\mathrm{jets}})$ fitted to it. The function $\mathcal{W}(x_\gamma^{\mathrm{jets}})$ is then assigned as a weight to each simulated event according to its value of x_γ^{jets}.

Reweighting in just one variable (x_γ^{jets} in our case) would bring the HERWIG prediction closer do data but is not sufficient for a perfect description. Therefore we reweight more than one variable – in our example we have chosen x_γ^{jets}, z_{vtx}, y, Q^2 and $E^*_{T\,1}$ (only two of them are shown as examples in Figs. B.1 and B.2). The final weight of an MC event is given by the product

$$\text{Event weight} = \mathcal{W}(x_\gamma^{\mathrm{jets}}) \cdot \mathcal{W}'(z_{\mathrm{vtx}}) \cdot \mathcal{W}''(y) \cdot \mathcal{W}'''(Q^2) \cdot \mathcal{W}''''(E^*_{T\,1}) \tag{B.1}$$

Unfortunately, the measured quantities are always to some extend correlated, and reweighting in one variable may spoil a nice description in the others. To overcome this problem, the reweighting procedure is done iteratively. In each step, new parameterisations of the $\mathcal{W}$-functions are determined and consequently applied as event weights on the MC events. Usually two or three iterations lead to a satisfactory and stable result. At the end, reweighted MC sample nicely describes the data as exemplified in upper right plots of Figs. B.1 and B.2 or in Figs. 4.11 and 4.12. Figures 4.11 and 4.12 moreover demonstrate that also the variables ignored in the reweighting procedure (e.g. W, $E^*_{T\,2}$,

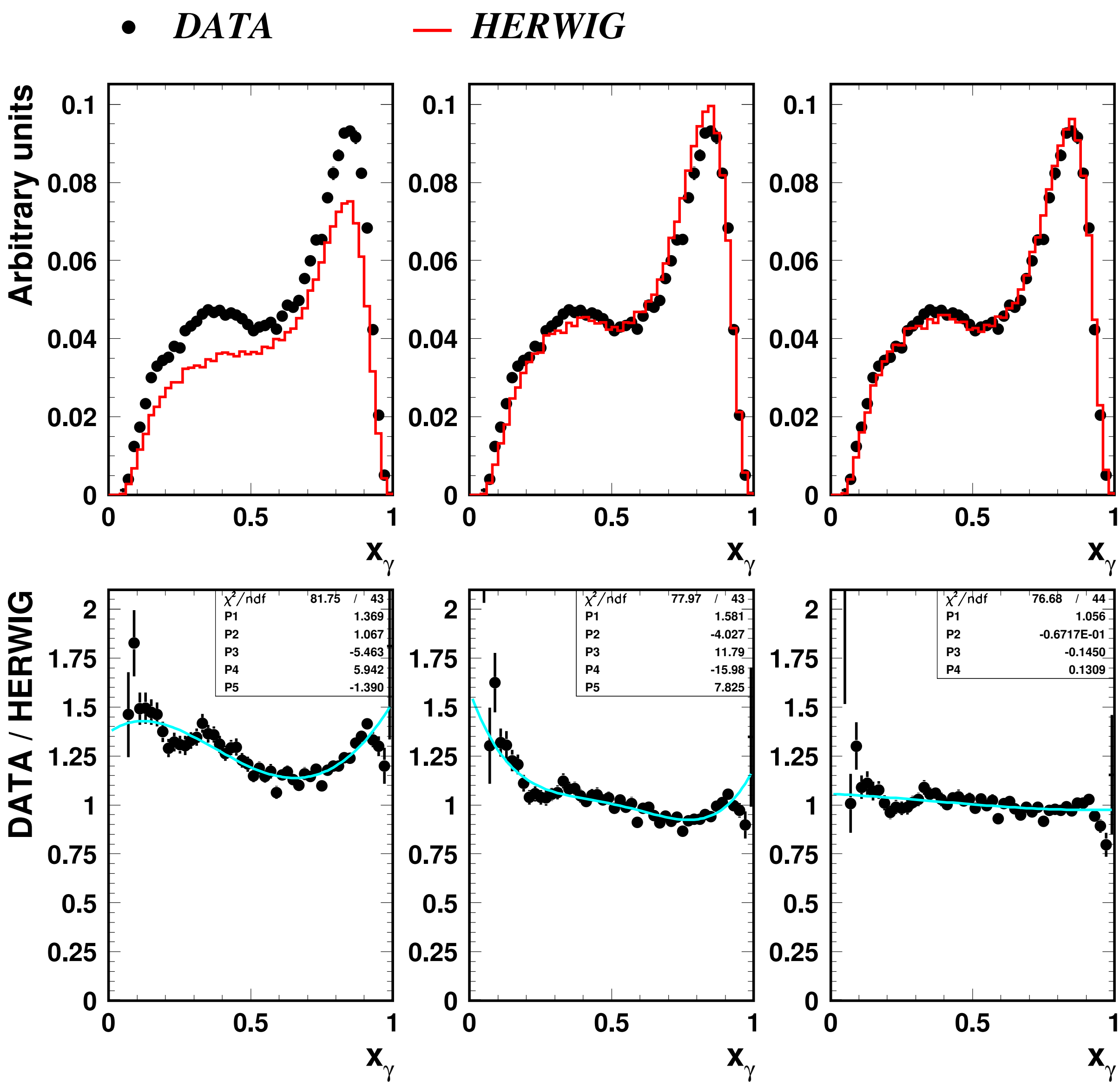

Figure B.1: Reweighting of $x_\gamma^{\rm jets}$ distribution. The upper row of plots presents comparisons of the DATA with HERWIG before the reweighting procedure (*left*), after the reweighting procedure performed in all variables but $x_\gamma^{\rm jets}$ (*middle*) and at the end of the procedure (*right*). The ratia of data over the HERWIG predictions together with their fits, i.e. functions $\mathcal{W}(x_\gamma^{\rm jets})$ (see the text), are shown in the lower row of the figure.

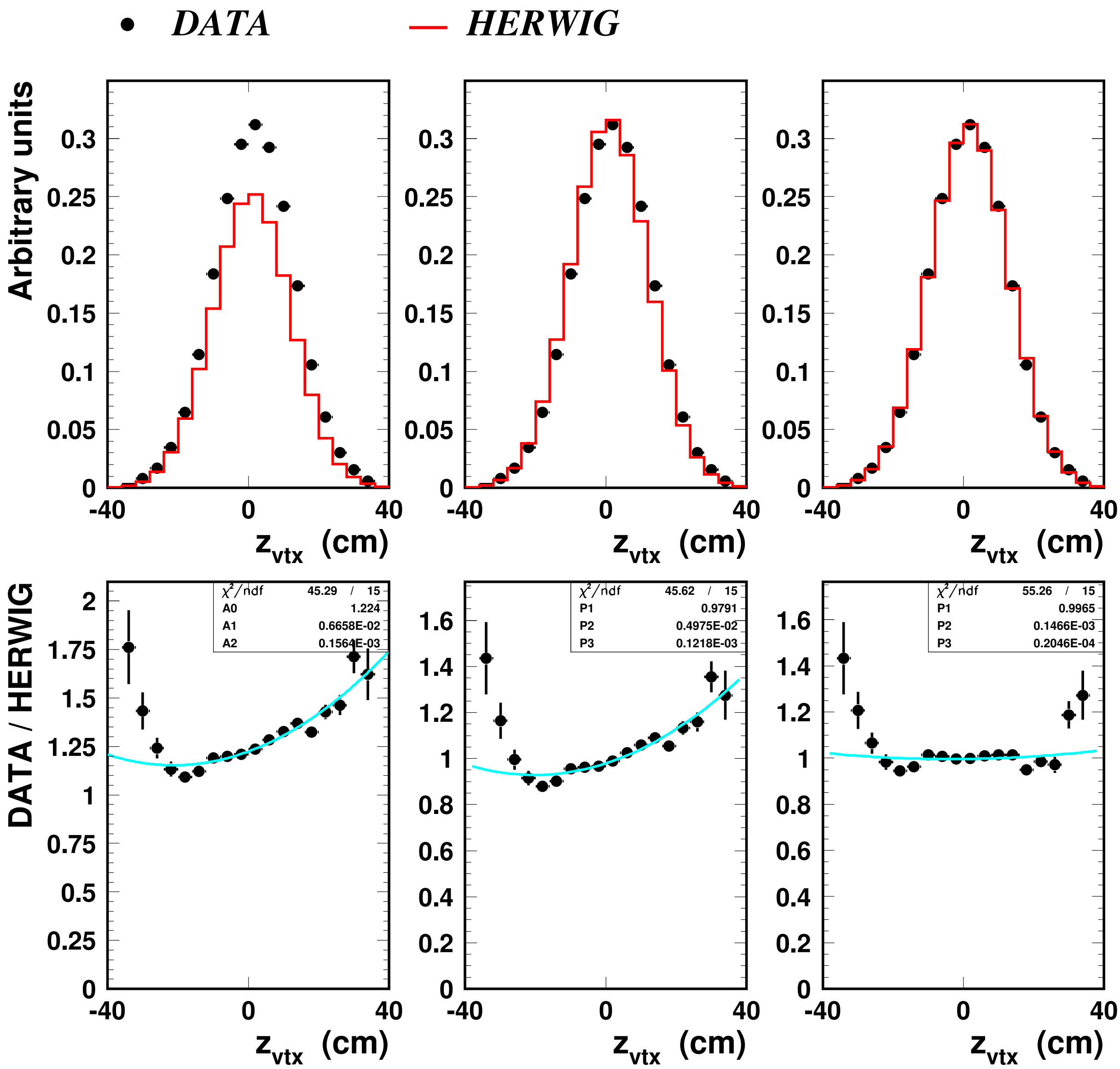

Figure B.2: Reweighting of z_{vtx} distribution. The upper row of plots presents comparisons of the DATA with HERWIG before the reweighting procedure (*left*), after the reweighting procedure performed in all variables but z_{vtx}(*middle*) and at the end of the procedure (*right*). The ratia of data over the HERWIG predictions together with their fits, i.e. functions $\mathcal{W}(z_{\mathrm{vtx}})$ (see the text), are shown in the lower row of the figure.

η_1^*, η_2^*) are well reproduced by the reweighted MC.

The middle plot in Fig. B.1 (Fig. B.2) shows how $x_\gamma^{\rm jets}$ ($z_{\rm vtx}$) distribution would be described, had we not performed the reweighting in $x_\gamma^{\rm jets}$ ($z_{\rm vtx}$), respectively, but only in the other four quantities from Eq. (B.1).

Appendix C

Tables of the Results

Q^2 (GeV^2)	E_T^* (GeV)	x_γ	$\mathrm{d}^3\sigma_{2\mathrm{jet}}/\mathrm{d}Q^2\mathrm{d}E_T^*\,\mathrm{d}x_\gamma^{\mathrm{jets}}$ ($\mathrm{pb/GeV}^3$)	δ_{stat} ($\mathrm{pb/GeV}^3$)	δ_{syst} ($\mathrm{pb/GeV}^3$)	hadr. corr.
2.0 – 4.4	5 – 10	0.12 – 0.35	94	1	20	0.78
		0.35 – 0.55	85.3	1.0	9.9	0.81
		0.55 – 0.75	74.8	0.9	7.9	1.17
		0.75 – 1.00	81	1	10	1.04
	10 – 20	0.12 – 0.35	10.0	0.2	1.8	0.87
		0.35 – 0.55	13.6	0.2	2.0	0.88
		0.55 – 0.75	17.6	0.2	2.1	1.03
		0.75 – 1.00	35.6	0.4	3.4	1.01
	20 – 60	0.12 – 0.35	0.033	0.004	0.010	0.81
		0.35 – 0.55	0.141	0.010	0.029	0.93
		0.55 – 0.75	0.239	0.012	0.045	0.94
		0.75 – 1.00	0.90	0.03	0.15	0.98
4.4 – 10	5 – 10	0.12 – 0.35	26.9	0.3	5.1	0.80
		0.35 – 0.55	29.5	0.3	3.2	0.82
		0.55 – 0.75	26.2	0.2	2.8	1.19
		0.75 – 1.00	40.9	0.4	4.8	1.05
	10 – 20	0.12 – 0.35	3.20	0.06	0.60	0.86
		0.35 – 0.55	5.03	0.07	0.66	0.90
		0.55 – 0.75	6.31	0.07	0.84	1.02
		0.75 – 1.00	16.3	0.2	1.5	1.02
	20 – 60	0.12 – 0.35	0.0169	0.0022	0.0050	0.88
		0.35 – 0.55	0.061	0.004	0.012	0.97
		0.55 – 0.75	0.103	0.006	0.019	0.89
		0.75 – 1.00	0.451	0.014	0.072	0.98
10 – 25	5 – 10	0.12 – 0.35	6.50	0.09	0.91	0.83
		0.35 – 0.55	8.03	0.08	0.86	0.85
		0.55 – 0.75	8.87	0.08	0.94	1.21
		0.75 – 1.00	15.8	0.1	1.9	1.05
	10 – 20	0.12 – 0.35	0.76	0.02	0.14	0.92
		0.35 – 0.55	1.51	0.02	0.21	0.88
		0.55 – 0.75	2.09	0.03	0.27	1.03
		0.75 – 1.00	6.22	0.06	0.57	1.02
	20 – 60	0.12 – 0.35	0.0048	0.0007	0.0016	1.05
		0.35 – 0.55	0.0182	0.0013	0.0031	0.84
		0.55 – 0.75	0.0403	0.0019	0.0079	0.96
		0.75 – 1.00	0.155	0.005	0.028	0.98
25 – 80	5 – 10	0.12 – 0.35	0.93	0.02	0.16	0.86
		0.35 – 0.55	1.30	0.02	0.13	0.89
		0.55 – 0.75	1.65	0.02	0.27	1.26
		0.75 – 1.00	3.97	0.03	0.46	1.06
	10 – 20	0.12 – 0.35	0.165	0.006	0.027	0.89
		0.35 – 0.55	0.330	0.007	0.045	0.91
		0.55 – 0.75	0.451	0.006	0.057	1.06
		0.75 – 1.00	1.75	0.02	0.17	1.02
	20 – 60	0.12 – 0.35	0.00246	0.00081	0.00060	1.06
		0.35 – 0.55	0.0052	0.0005	0.0015	0.88
		0.55 – 0.75	0.0071	0.0004	0.0020	0.95
		0.75 – 1.00	0.0534	0.0015	0.0097	0.98

Table C.1: Triple differential dijet cross section $\mathrm{d}^3\sigma_{2\mathrm{jet}}/\mathrm{d}Q^2\mathrm{d}E_T^*\,\mathrm{d}x_\gamma^{\mathrm{jets}}$. The cross section is given together with the statistical and systematic errors. The correction factors for the hadronisation effects applied to the NLO QCD predictions are also shown.

Q^2 (GeV^2)	y	η^*	$\mathrm{d}^3\sigma_{2\mathrm{jet}}/\mathrm{d}Q^2\mathrm{d}y\mathrm{d}\eta^*$ (pb/GeV^2)	δ_{stat} (pb/GeV^2)	δ_{syst} (pb/GeV^2)	hadr. corr.
2.0 – 4.4	0.10 – 0.25	-2.5 – (-2.0)	870	10	110	0.89
		-2.0 – (-1.5)	800	10	110	1.01
		-1.5 – (-1.0)	643	11	98	1.03
		-1.0 – (-0.5)	480	8	66	0.99
		-0.5 – 0.0	404	8	64	0.94
	0.25 – 0.50	-2.5 – (-2.0)	531	7	48	1.07
		-2.0 – (-1.5)	362	5	38	1.04
		-1.5 – (-1.0)	297	5	42	0.97
		-1.0 – (-0.5)	234	4	37	0.94
		-0.5 – 0.0	193	4	30	0.92
	0.50 – 0.85	-2.5 – (-2.0)	224	4	21	1.03
		-2.0 – (-1.5)	168	3	17	0.95
		-1.5 – (-1.0)	130	2	15	0.91
		-1.0 – (-0.5)	123	3	23	0.91
		-0.5 – 0.0	109	3	18	0.88
4.4 – 10	0.10 – 0.25	-2.5 – (-2.0)	377	4	44	0.90
		-2.0 – (-1.5)	363	4	41	1.02
		-1.5 – (-1.0)	266	3	30	1.04
		-1.0 – (-0.5)	192	2	24	0.99
		-0.5 – 0.0	154	2	23	0.96
	0.25 – 0.50	-2.5 – (-2.0)	209	2	18	1.10
		-2.0 – (-1.5)	137	2	13	1.06
		-1.5 – (-1.0)	97	1	11	1.00
		-1.0 – (-0.5)	75	1	10	0.96
		-0.5 – 0.0	62.2	1.0	9.7	0.93
	0.50 – 0.85	-2.5 – (-2.0)	80.7	1.5	6.8	1.05
		-2.0 – (-1.5)	55.3	1.1	5.6	0.98
		-1.5 – (-1.0)	41.4	0.9	4.2	0.94
		-1.0 – (-0.5)	37.6	0.8	5.6	0.90
		-0.5 – 0.0	31.9	0.8	6.1	0.89
10 – 25	0.10 – 0.25	-2.5 – (-2.0)	133	1	16	0.89
		-2.0 – (-1.5)	132	1	14	1.04
		-1.5 – (-1.0)	94	1	11	1.05
		-1.0 – (-0.5)	63.7	0.8	8.0	1.04
		-0.5 – 0.0	48.3	0.7	7.9	0.97
	0.25 – 0.50	-2.5 – (-2.0)	71.2	0.8	6.3	1.11
		-2.0 – (-1.5)	45.8	0.6	4.3	1.09
		-1.5 – (-1.0)	30.8	0.4	3.0	1.01
		-1.0 – (-0.5)	23.1	0.3	2.7	0.97
		-0.5 – 0.0	17.6	0.3	2.3	0.95
	0.50 – 0.85	-2.5 – (-2.0)	25.0	0.5	2.0	1.06
		-2.0 – (-1.5)	16.4	0.3	1.5	0.99
		-1.5 – (-1.0)	12.1	0.3	1.4	0.94
		-1.0 – (-0.5)	8.4	0.2	1.3	0.93
		-0.5 – 0.0	7.3	0.2	1.2	0.91
25 – 80	0.10 – 0.25	-2.5 – (-2.0)	28.0	0.3	4.1	0.90
		-2.0 – (-1.5)	29.5	0.3	3.2	1.04
		-1.5 – (-1.0)	19.8	0.2	2.6	1.08
		-1.0 – (-0.5)	13.8	0.2	2.3	1.05
		-0.5 – 0.0	9.4	0.2	1.9	0.99
	0.25 – 0.50	-2.5 – (-2.0)	16.8	0.2	1.5	1.13
		-2.0 – (-1.5)	11.1	0.2	1.0	1.11
		-1.5 – (-1.0)	7.31	0.11	0.70	1.03
		-1.0 – (-0.5)	4.69	0.08	0.51	1.02
		-0.5 – 0.0	3.68	0.08	0.43	0.98
	0.50 – 0.85	-2.5 – (-2.0)	6.43	0.17	0.52	1.09
		-2.0 – (-1.5)	4.32	0.14	0.39	1.00
		-1.5 – (-1.0)	2.78	0.10	0.28	0.98
		-1.0 – (-0.5)	1.95	0.08	0.26	0.96
		-0.5 – 0.0	1.42	0.06	0.18	0.94

Table C.2: Triple differential dijet cross section $\mathrm{d}^3\sigma_{2\mathrm{jet}}/\mathrm{d}Q^2\mathrm{d}y\mathrm{d}\eta^*$. See the caption of Table C.1 for further details.

Q^2 (GeV^2)	η^*	E_T^* (GeV)	$\mathrm{d}^3\sigma_{2\mathrm{jet}}/\mathrm{d}Q^2\mathrm{d}\eta^*\,\mathrm{d}E_T^*$ ($\mathrm{pb/GeV}^3$)	δ_{stat} ($\mathrm{pb/GeV}^3$)	δ_{syst} ($\mathrm{pb/GeV}^3$)	hadr. corr.
2.0 – 4.4	-2.5 – (-1.7)	5 – 7	28.6	0.4	2.5	1.04
		7 – 10	54.9	0.5	5.5	0.99
		10 – 15	16.6	0.2	1.8	0.97
		15 – 20	2.78	0.05	0.42	0.94
		20 – 30	0.276	0.010	0.076	0.92
	-1.7 – (-1.3)	5 – 7	22.5	0.4	2.8	0.99
		7 – 10	35.5	0.4	4.4	1.00
		10 – 15	12.9	0.2	1.5	1.03
		15 – 20	3.50	0.08	0.47	1.00
		20 – 30	0.63	0.02	0.10	0.98
	-1.3 – 0	5 – 7	19.4	0.3	2.7	0.89
		7 – 10	24.6	0.3	3.8	0.95
		10 – 15	8.1	0.1	1.0	1.00
		15 – 20	2.07	0.04	0.29	1.00
		20 – 30	0.450	0.014	0.072	0.99
4.4 – 10	-2.5 – (-1.7)	5 – 7	11.2	0.1	1.1	1.06
		7 – 10	22.0	0.2	1.9	1.01
		10 – 15	6.85	0.06	0.84	0.99
		15 – 20	1.20	0.02	0.21	0.96
		20 – 30	0.136	0.005	0.033	0.91
	-1.7 – (-1.3)	5 – 7	7.60	0.10	0.79	1.00
		7 – 10	13.0	0.1	1.5	1.04
		10 – 15	5.22	0.06	0.50	1.03
		15 – 20	1.59	0.03	0.21	1.01
		20 – 30	0.298	0.011	0.052	0.97
	-1.3 – 0	5 – 7	6.16	0.06	0.68	0.91
		7 – 10	8.3	0.1	1.1	0.97
		10 – 15	3.02	0.03	0.35	1.00
		15 – 20	0.88	0.01	0.12	1.01
		20 – 30	0.199	0.005	0.031	1.00
10 – 25	-2.5 – (-1.7)	5 – 7	3.64	0.04	0.32	1.06
		7 – 10	7.41	0.05	0.64	1.02
		10 – 15	2.41	0.02	0.29	0.99
		15 – 20	0.445	0.007	0.071	0.94
		20 – 30	0.045	0.002	0.011	0.93
	-1.7 – (-1.3)	5 – 7	2.39	0.03	0.25	1.03
		7 – 10	4.27	0.04	0.46	1.06
		10 – 15	1.86	0.02	0.17	1.05
		15 – 20	0.529	0.010	0.075	1.01
		20 – 30	0.098	0.003	0.017	0.96
	-1.3 – 0	5 – 7	1.80	0.02	0.20	0.94
		7 – 10	2.41	0.02	0.30	0.98
		10 – 15	0.98	0.01	0.11	1.03
		15 – 20	0.313	0.005	0.040	1.02
		20 – 30	0.078	0.002	0.011	1.00
25 – 80	-2.5 – (-1.7)	5 – 7	0.741	0.009	0.087	1.12
		7 – 10	1.58	0.01	0.17	1.04
		10 – 15	0.589	0.006	0.072	0.99
		15 – 20	0.134	0.002	0.024	0.94
		20 – 30	0.0143	0.0006	0.0046	0.92
	-1.7 – (-1.3)	5 – 7	0.451	0.007	0.057	1.00
		7 – 10	0.91	0.01	0.10	1.09
		10 – 15	0.471	0.006	0.050	1.05
		15 – 20	0.163	0.003	0.023	1.00
		20 – 30	0.0324	0.0012	0.0068	0.99
	-1.3 – 0	5 – 7	0.301	0.004	0.041	0.98
		7 – 10	0.477	0.005	0.064	1.03
		10 – 15	0.238	0.003	0.030	1.05
		15 – 20	0.090	0.002	0.010	1.02
		20 – 30	0.0229	0.0007	0.0042	1.00

Table C.3: Triple differential dijet cross section $\mathrm{d}^3\sigma_{2\mathrm{jet}}/\mathrm{d}Q^2\mathrm{d}\eta^*\,\mathrm{d}E_T^*$. See the caption of Table C.1 for further details.

Q^2 (GeV^2)	x_γ	y	$\mathrm{d}^3\sigma_{\mathrm{ep}}/\mathrm{d}Q^2\mathrm{d}x_\gamma^{\mathrm{jets}}\mathrm{d}y$ (pb/GeV^2)	δ_{stat} (pb/GeV^2)	δ_{syst} (pb/GeV^2)	hadr. corr.
2.0 − 4.4	0 − 0.75	0.10 − 0.25	586	12	100	0.98
		0.25 − 0.40	409	9	63	0.93
		0.40 − 0.55	283	7	41	0.88
		0.55 − 0.70	199	5	27	0.86
		0.70 − 0.85	192	8	27	0.87
	0.75 − 1	0.10 − 0.25	1360	31	200	0.96
		0.25 − 0.40	653	15	63	1.11
		0.40 − 0.55	289	9	25	1.15
		0.55 − 0.70	164	7	14	1.13
		0.70 − 0.85	89.6	6.2	7.3	1.12
4.4 − 10	0 − 0.75	0.10 − 0.25	198	3	27	0.99
		0.25 − 0.40	126	2	17	0.95
		0.40 − 0.55	92	2	12	0.90
		0.55 − 0.70	66.9	2.1	9.1	0.88
		0.70 − 0.85	53.6	2.2	7.1	0.88
	0.75 − 1	0.10 − 0.25	744	11	74	0.97
		0.25 − 0.40	291	6	30	1.12
		0.40 − 0.55	138	4	12	1.17
		0.55 − 0.70	69.0	2.8	5.5	1.15
		0.70 − 0.85	34.3	2.4	2.7	1.15
10 − 25	0 − 0.75	0.10 − 0.25	58.8	0.9	8.6	1.04
		0.25 − 0.40	37.8	0.7	4.6	0.97
		0.40 − 0.55	25.0	0.6	3.1	0.91
		0.55 − 0.70	17.5	0.5	2.2	0.91
		0.70 − 0.85	13.4	0.7	1.5	0.88
	0.75 − 1	0.10 − 0.25	294	4	30	0.97
		0.25 − 0.40	112	2	12	1.13
		0.40 − 0.55	49.6	1.4	4.0	1.17
		0.55 − 0.70	24.0	1.0	1.8	1.14
		0.70 − 0.85	12.35	0.84	0.91	1.14
25 − 80	0 − 0.75	0.10 − 0.25	9.5	0.2	1.8	1.07
		0.25 − 0.40	6.98	0.15	0.85	1.04
		0.40 − 0.55	5.00	0.15	0.51	0.97
		0.55 − 0.70	3.32	0.17	0.36	0.93
		0.70 − 0.85	2.25	0.27	0.22	0.92
	0.75 − 1	0.10 − 0.25	72.5	0.9	8.6	0.98
		0.25 − 0.40	31.4	0.6	2.9	1.12
		0.40 − 0.55	15.0	0.5	1.3	1.14
		0.55 − 0.70	8.99	0.47	0.88	1.16
		0.70 − 0.85	4.01	0.57	0.85	1.13

Table C.4: Triple differential event cross section $\mathrm{d}^3\sigma_{\mathrm{ep}}/\mathrm{d}Q^2\mathrm{d}x_\gamma^{\mathrm{jets}}\mathrm{d}y$. See the caption of Table C.1 for further details.

Bibliography

[Alt82] G. Altarelli, *Partons in Quantum Chromodynamics*, Phys. Rept. **81**, 1 (1982).

[AP77] G. Altarelli and G. Parisi, *Asymptotic Freedom in Parton Language.*, Nucl. Phys. **B 126**, 298 (1977).

[BEK91] S. Bentvelsen, J. Engelen and P. Kooijman, Reconstruction of (x, Q^2) and Extraction of Structure Functions in Neutral Current Scattering at HERA, in *Proc. of the Workshop on Physics at HERA, Vol. 1*, edited by W. Buchmüller and G. Ingelman, page 23, Hamburg, 1991, DESY, NIKHEF-H-92-02.

[BL78] Y. Balitskii and L. Lipatov, *The Pomeranchuk Singularity in Quantum Chromodynamics.*, Sov. J. Nucl. Phys. **28**, 822 (1978).

[C$^+$99] G. Corcella et al., *HERWIG 6.1 Release Note*, (1999), hep-ph/9912396.

[CCH91] S. Catani, M. Ciafaloni and F. Hautmann, *High Energy Factorisation and Small x Heavy Flavor Production*, Nucl. Phys. **B 366**, 135 (1991).

[CDSW93] S. Catani, Y. L. Dokshitzer, M. H. Seymour and B. R. Webber, *Longitudinally Invariant K(t) Clustering Algorithms for Hadron Hadron Collisions*, Nucl. Phys. **B406**, 187–224 (1993).

[CE91] J. Collins and R. Ellis, *Heavy Quark Production in Very High-Energy Hadron Collisions*, Nucl. Phys. **B 360**, 3 (1991).

[CFM90a] S. Catani, F. Fiorani and G. Marchesini, *QCD Coherence in Initial State Radiation*, Phys. Lett. **B 234**, 339 (1990).

[CFM90b] S. Catani, F. Fiorani and G. Marchesini, *Small x Behaviour of Initial State Radiation in Perturbative QCD*, Nucl. Phys. **B 336**, 18 (1990).

[Chy00a] J. Chyla, *Partonic Structure of $\gamma^*(L)$ in Hard Collisions*, (2000), hep-ph/0010055.

[Chy00b] J. Chyla, *QCD Improved Parton Distribution Functions of $\gamma^*(L)$*, Phys. Lett. **B488**, 289–298 (2000), hep-ph/0006232.

[Chy01] J. Chyla, *Hard Collisions of Photons: Plea for a Common Language*, (2001), hep-ph/0102100.

[Chyed] J. Chyla, *Quarks, Partons and Quantum Chromodynamics*, (Available from http://www-hep.fzu.cz/Theory/notes/text.pdf), unpublished.

[Cia88] M. Ciafaloni, *Coherence Effects in Initial Jets at Small Q^2/s*, Nucl. Phys. **B 296**, 49 (1988).

[CS97] S. Catani and M. H. Seymour, *A General Algorithm for Calculating Jet Cross Sections in NLO QCD*, Nucl. Phys. **B485**, 291–419 (1997), hep-ph/9605323.

[CS03] J. Chyla and K. Sedlak, *Dijet Cross Sections in e p Collisions: Who is Afraid of Symmetric Cuts?*, (2003), hep-ph/0308116.

[CSS88] J. C. Collins, D. E. Soper and G. Sterman, *Factorization of Hard Processes in QCD*, Adv. Ser. Direct. High Energy Phys. **5**, 1–91 (1988).

[CT00a] J. Chyla and M. Tasevsky, *Interpreting Virtual Photon Interactions in Terms of Parton Distribution Functions*, Phys. Rev. **D62**, 114025 (2000), hep-ph/9912514.

[CT00b] J. Chyla and M. Tasevsky, *The Relevance of $\gamma^*(L)$ in Hard Collisions of Virtual Photons*, Eur. Phys. J. **C16**, 471–479 (2000), hep-ph/0003300.

[CT01] J. Chyla and M. Tasevsky, *Resolved $\gamma^*(L)$ in Hard Collisions of Virtual Photons: QCD Effects*, Eur. Phys. J. **C18**, 723–729 (2001), hep-ph/0010254.

[D'A95a] G. D'Agostini, *Comments on the Bayesian Unfolding*, unpublished (1995), ZEUS-Note 95-166; also available from http://www-zeus.roma1.infn.it/~agostini/bayes_comments.ps.

[D'A95b] G. D'Agostini, *A Multidimensional Unfolding Method Based on Bayes' theorem*, Nucl. Instrum. Meth. **A362**, 487–498 (1995).

[DHKW99] C. Duprel, T. Hadig, N. Kauer and M. Wobisch, *Comparison of Next-to-Leading Order Calculations for Jet Cross Sections in Deep-Inelastic Scattering*, (1999), hep-ph/9910448.

[Dir96] M. Dirkmann, *Calibration of the SpaCal with Cosmics*, (1996), Internal H1 note h1-0596-477.

[Dok77] Y. Dokshitser, *Calculation of the Structure Functions for Deep Inelastic Scattering and e+ e- Annihilation by Perturbation Theory in Quantum Chromodynamics.*, Sov. Phys. JETP **46**, 641 (1977).

[ea87] R. B. et al., GEANT3, Technical Report CERN-DD/EE/84-1, CERN, 1987.

[Eng95] R. Engel, *Photoproduction within the Two Component Dual Parton Model. 1. Amplitudes and Cross-sections*, Z. Phys. **C66**, 203–214 (1995).

[ER96] R. Engel and J. Ranft, *Hadronic Photon-Photon Interactions at High Energies*, Phys. Rev. **D54**, 4244–4262 (1996), hep-ph/9509373.

[ERT81] R. K. Ellis, D. A. Ross and A. E. Terrano, *The Perturbative Calculation of Jet Structure in e+ e- Annihilation*, Nucl. Phys. **B178**, 421 (1981).

[ES93] S. D. Ellis and D. E. Soper, *Successive Combination Jet Algorithm for Hadron Collisions*, Phys. Rev. **D48**, 3160–3166 (1993), hep-ph/9305266.

[FR97] S. Frixione and G. Ridolfi, *Jet Photoproduction at HERA*, Nucl. Phys. **B507**, 315–333 (1997), hep-ph/9707345.

[FS98] J. R. Forshaw and A. Sabio Vera, *QCD Coherence and Jet Rates in Small x Deep Inelastic Scattering*, Phys. Lett. **B440**, 141–150 (1998), hep-ph/9806394.

[FS00] C. Friberg and T. Sjöstrand, *Effects of Longitudinal Photons*, Phys. Lett. **B492**, 123–134 (2000), hep-ph/0009003.

[GL72] V. Gribov and L. Lipatov, *Deep Inelastic e p Scattering in Perturbation Theory; e+ e- Pair Annihilation and Deep Inelastic e p Scattering in Perturbation Theory.*, Sov. J. Nucl. Phys. **15**, 438 and 675 (1972).

[Gla98] A. A. Glazov, *Measurement of the Proton Structure Functions $F2(x, Q^2)$ and $F(L)(x, Q^2)$ with the H1 Detector at HERA*, Dissertation, Humboldt Universitat, Berlin (1998), DESY-THESIS-1998-005.

[GLR83] L. Gribov, E. Levin and M. Ryskin, *Semihard Processes in QCD*, Phys. Rep. **100**, 1 (1983).

[Group93] B. Andrieu et al. (H1 Calorimeter Group Collaboration), *Results from Pion Calibration Runs for the H1 Liquid Argon Calorimeter and Comparisons with Simulations*, Nucl. Instrum. Meth. **A336**, 499–509 (1993).

[Group94] B. Andrieu et al. (H1 Calorimeter Group Collaboration), *Beam Tests and Calibration of the H1 Liquid Argon Calorimeter with Electrons*, Nucl. Instrum. Meth. **A350**, 57–72 (1994).

[GRS96] M. Glück, E. Reya and M. Stratmann, *Probing the Parton Densities of Virtual Photons at ep Colliders*, Phys. Rev. **D54**, 5515–5522 (1996), hep-ph/9605297.

[GRS99] M. Glück, E. Reya and I. Schienbein, *Radiatively Generated Parton Distributions of Real and Virtual Photons*, Phys. Rev. **D60**, 054019 (1999), hep-ph/9903337 (Erratum-ibid.D62:019902,2000).

[H1 96] H1 Collaboration, SPACAL group, R.-D. Appuhn et al., *Performance of an Electromagnetic Lead / Scintillating Fiber Calorimeter for the H1 Detector*, Nucl. Instrum. Meth. **A374**, 149–156 (1996).

[H1 97] H1 Collaboration, SPACAL group, R.-D. Appuhn et al., *The H1 Lead/Scintillating-Fiber Calorimeter*, Nucl. Instr. Meth. **A 386**, 397 (1997).

[H197a] C. Adloff et al. (H1 Collaboration), *Determination of the Longitudinal Proton Structure Function $F(L)(x, Q^2)$ at Low x*, Phys. Lett. **B393**, 452–464 (1997), hep-ex/9611017.

[H197b] C. Adloff et al. (H1 Collaboration), *Diffraction Dissociation in Photoproduction at HERA*, Z. Phys. **C74**, 221–236 (1997), hep-ex/9702003.

[H197c] H1 Collaboration, I. Abt et al. (H1 Collaboration), *The H1 Detector at HERA*, Nucl. Instr. Meth. **A386**, 310–347 (1997).

[H197d] H1 Collaboration, I. Abt et al. (H1 Collaboration), *The Tracking, Calorimeter and Muon Detectors of the H1 Experiment at HERA*, Nucl. Instr. Meth. **A386**, 348–396 (1997).

[H100] C. Adloff et al. (H1 Collaboration), *Measurement of Dijet Cross-Sections at Low Q^2 and the Extraction of an Effective Parton Density for the Virtual Photon*, Eur. Phys. J. **C13**, 397–414 (2000), hep-ex/9812024.

[H101a] C. Adloff et al. (H1 Collaboration), *Dijet Production in Charged and Neutral Current e+ p Interactions at High Q^2*, Eur. Phys. J. **C19**, 429–440 (2001), hep-ex/0010016.

[H101b] C. Adloff et al. (H1 Collaboration), *Measurement and QCD Analysis of Jet Cross Sections in Deep- Inelastic Positron Proton Collisions at $\sqrt{s}$ of 300 GeV*, Eur. Phys. J. **C19**, 289–311 (2001), hep-ex/0010054.

[H101c] C. Adloff et al. (H1 Collaboration), *Three-Jet Production in Deep-Inelastic Scattering at HERA*, Phys. Lett. **B515**, 17–29 (2001), hep-ex/0106078.

[H102a] C. Adloff et al. (H1 Collaboration), *Measurement of Dijet Cross Sections in Photoproduction at HERA*, Eur. Phys. J. **C25**, 13–23 (2002), hep-ex/0201006.

[H102b] C. Adloff et al. (H1 Collaboration), *Measurement of Inclusive Jet Cross-Sections in Deep- Inelastic e p Scattering at HERA*, Phys. Lett. **B542**, 193–206 (2002), hep-ex/0206029.

[H103a] C. Adloff et al. (H1 Collaboration), *Measurement of Inclusive Jet Cross Sections in Photoproduction at HERA*, (2003), hep-ex/0302034.

[H103b] A. Aktas et al. (H1 Collaboration), *Inclusive Dijet Production at Low Bjorken-x in Deep Inelastic Scattering*, (2003), hep-ex/0310019.

[H103c] A. Aktas et al. (H1 Collaboration), *Inclusive Dijet Production at Low Bjorken-x in Deep Inelastic Scattering*, (2003), hep-ex/0310019.

[H104] A. Aktas et al. (H1 Collaboration), *Measurement of Dijet Production at Low Q^2 at HERA*, *submitted to Eur. Phys. J. C* (2004), hep-ex/0401010.

[HER00a] K. Ackerstaff et al. (HER Collaboration), *Measurement of Angular Distributions and $R = \sigma(L)/\sigma(T)$ in Diffractive Electroproduction of ρ^0 Mesons*, Eur. Phys. J. **C18**, 303–316 (2000), hep-ex/0002016.

[HER00b] K. Ackerstaff et al. (HER Collaboration), *Nuclear Effects on $R = \sigma(L)/\sigma(T)$ in Deep Inelastic Scattering*, Phys. Lett. **B475**, 386–394 (2000), hep-ex/9910071.

[IER97] G. Ingelman, A. Edin and J. Rathsman, *LEPTO 6.5: A Monte Carlo Generator for Deep Inelastic Lepton-Nucleon Scattering*, Comp. Phys. Comm. **101**, 108 (1997), hep-ph/9605286.

[Jan96] J. Janoth, *The Calibration System CAM for the New Calorimeter SpaCal of the H1 Detector at HERA and Analysis of First Data. (In German)*, Dissertation, Universitat Heidelberg (1996), HD-IHEP-96-17.

[JS01] H. Jung and G. P. Salam, *Hadronic Final State Predictions from CCFM: The Hadron- Level Monte Carlo Generator CASCADE*, Eur. Phys. J. **C19**, 351–360 (2001), hep-ph/0012143.

[Jun95] H. Jung, *Hard Diffractive Scattering in High Energy e-p Collisions and the Monte Carlo Generator RAPGAP*, Comp. Phys. Comm. **86**, 147 (1995).

[Jun02a] H. Jung, *The CCFM Monte Carlo Generator CASCADE*, Comput. Phys. Commun. **143**, 100–111 (2002), hep-ph/0109102.

[Jun02b] H. Jung, *Heavy Quark Production at the TEVATRON and HERA Using k(t) Factorization with CCFM Evolution*, Phys. Rev. **D65**, 034015 (2002), hep-ph/0110034.

[KK96] M. Klasen and G. Kramer, *Dijet Cross-Sections at $O(\alpha\alpha_s^2)$ in Photon–Proton Collisions*, Phys. Lett. **B366**, 385–393 (1996), hep-ph/9508337.

[KK97] M. Klasen and G. Kramer, *Inclusive Two-Jet Production at HERA: Direct and Resolved Cross Sections in Next-to-Leading Order QCD*, Z. Phys. **C76**, 67–74 (1997), hep-ph/9611450.

[KLF76] E. Kuraev, L. Lipatov and V. Fadin, *Multi-Reggeon Processes in the Yang-Mills Theory*, Sov. Phys. JETP **44**, 443 (1976).

[KLF77] E. Kuraev, L. Lipatov and V. Fadin, *The Pomeranchuk Singularity in Non-abelian Gauge Theories.*, Sov. Phys. JETP **45**, 199 (1977).

[KP98] G. Kramer and B. Potter, *Low Q^2 Jet Production at HERA in Next-to-Leading Order QCD*, Eur. Phys. J. **C5**, 665–679 (1998), hep-ph/9804352.

[KZS01] M. Krawczyk, A. Zembrzuski and M. Staszel, *Survey of Present Data on Photon Structure Functions and Resolved Photon Processes*, Phys. Rept. **345**, 265–450 (2001), hep-ph/0011083.

[L+97] H. L. Lai et al., *Improved Parton Distributions from Global Analysis of Recent Deep Inelastic Scattering and Inclusive Jet Data*, Phys. Rev. **D55**, 1280–1296 (1997), hep-ph/9606399.

[Lip75] L. Lipatov, *The Parton Model and Perturbation Theory.*, Sov. J. Nucl. Phys. **20**, 94 (1975).

[LRSS91] E. Levin, M. Ryskin, Y. Shabelskii and A. Shuvaev, *Deep Inelastic Structure Function at low x*, Sov. J. Nucl. Phys. **53**, 657 (1991).

[M+92] G. Marchesini et al., *HERWIG: A Monte Carlo Event Generator For Simulating Hadron Emission Reactions with Interfering Gluons. Version 5.1 – April 1991*, Comput. Phys. Commun. **67**, 465–508 (1992).

[Mar95] G. Marchesini, *QCD Coherence in the Structure Function and Associated Distributions at Small x*, Nucl. Phys. **B 445**, 49 (1995).

[Mey97] A. Meyer, *Measurement of the Structure Function $F2(x, Q^2)$ of the Proton at Low Q^2 with the H1 Detector at HERA Using the New Detector Components Spacal and BDC*, Dissertation, Universitat Hamburg (1997), DESY-FH1-97-01.

[Nis00] R. Nisius, *The Photon Structure from Deep Inelastic Electron Photon Scattering*, Phys. Rept. **332**, 165–317 (2000), hep-ex/9912049.

[Poe00] R. Poeschl, *Measurement of the Double Differential Dijet Rate in Deep Inelastic Scattering at HERA and Comparison to NLO QCD Calculations*, Dissertation, Dortmund (2000), DESY-THESIS-2000-057.

[Pot99] B. Potter, *JetViP 1.1: Calculating One- and Two-Jet Cross Sections with Virtual Photons in NLO QCD*, Comput. Phys. Commun. **119**, 45–66 (1999), hep-ph/9806437.

[Pot00] B. Potter, *JetViP 2.1: The Hbook Version*, Comput. Phys. Commun. **133**, 105–118 (2000), hep-ph/9911221.

[Sal99] G. P. Salam, *Soft Emissions and the Equivalence of BFKL and CCFM Final States*, JHEP **03**, 009 (1999), hep-ph/9902324.

[SB87] T. Sjöstrand and M. Bengtsson, *The Lund Monte Carlo for Jet Fragmentation and e+ e- Physics: JETSET Version 6.3: an Update*, Comp. Phys. Comm. **43**, 367 (1987).

[Sjo86] T. Sjostrand, *The Lund Monte Carlo for Jet Fragmentation and e+ e- Physics: JETSET Version 6.2*, Comp. Phys. Comm. **39**, 347 (1986).

[Sjo94] T. Sjostrand, *High-Energy Physics Event Generation with PYTHIA 5.7 and JETSET 7.4.*, Comp. Phys. Comm. **82**, 74 (1994).

[SS96] G. A. Schuler and T. Sjöstrand, *Parton Distributions of the Virtual Photon*, Phys. Lett. **B376**, 193–200 (1996), hep-ph/9601282.

[Tas99] M. Tasevsky, *Virtual Photon Structure from Low Q^2 Dijet Production at HERA*, Dissertation, Faculty of Mathematics and Physics, Charles University, Praha (1999), (available from http://www-h1.desy.de/psfiles/theses/h1th-181.ps).

[Tza] E. Tzamariudaki, *Performance of the H1 Lead/Scintillating-Fibre Calorimeter*, One of three related talks included in DESY-98-005 and given at the 7th International Conference on Calorimetry in High- Energy Physics (ICCHEP 97), Tucson, AZ, 9-14 Nov 1997.

[W.A78] W.A. Bardeen et al., *Deep Inelastic Scattering Beyond the Leading Order in Asymptotically Free Gauge Theories*, Phys. Rev. **D 18**, 3998 (1978).

[Web84] B. R. Webber, *A QCD Model for Jet Fragmentation Including Soft Gluon Interference*, Nucl. Phys. **B238**, 492 (1984).

[Web98] B. R. Webber, *Jet Rates in Deep Inelastic Scattering at Small x*, Phys. Lett. **B444**, 81 (1998), hep-ph/9810286.

[x02] B. Andersson et al. (Small x Collaboration), *Small x Phenomenology: Summary and Status*, Eur. Phys. J. **C25**, 77–101 (2002), hep-ph/0204115.

[ZEUS99] J. Breitweg et al. (ZEUS Collaboration), *Measurement of Dijet Photoproduction at High Transverse Energies at HERA*, Eur. Phys. J. **C11**, 35–50 (1999), hep-ex/9905046.

[ZEUS00] J. Breitweg et al. (ZEUS Collaboration), *The Q^2 Dependence of Dijet Cross Sections in γp Interactions at HERA*, Phys. Lett. **B479**, 37–52 (2000), hep-ex/0002010.

[ZEUS02a] S. Chekanov et al. (ZEUS Collaboration), *Dijet Photoproduction at HERA and the Structure of the Photon*, Eur. Phys. J. **C23**, 615–631 (2002), hep-ex/0112029.

[ZEUS02b] S. Chekanov et al. (ZEUS Collaboration), *Dijet Production in Neutral Current Deep Inelastic Scattering at HERA*, Eur. Phys. J. **C23**, 13–27 (2002), hep-ex/0109029.

[ZEUS02c] S. Chekanov et al. (ZEUS Collaboration), *Inclusive Jet Cross Sections in the Breit Frame in Neutral Current Deep Inelastic Scattering at HERA and Determination of α_s*, Phys. Lett. **B547**, 164–180 (2002), hep-ex/0208037.

[ZEUS03a] S. Chekanov et al. (ZEUS Collaboration), *Scaling Violations and Determination of α_s from Jet Production in γp Interactions at HERA*, Phys. Lett. **B560**, 7–23 (2003), hep-ex/0212064.

[ZEUS03b] S. Chekanov et al. (ZEUS Collaboration), *Study of the Azimuthal Asymmetry of Jets in Neutral Current Deep Inelastic Scattering at HERA*, Phys. Lett. **B551**, 226–240 (2003), hep-ex/0210064.